



Cancer Detection Using Advanced UWB Microwave
Technology

by

Bilal Khalid

<https://orcid.org/0000-0003-0029-4072>

A thesis submitted in partial fulfilment of the requirements of London
South Bank University for the degree of Doctor of Philosophy

School of Engineering
Division of Electrical Electronic Engineering
London South Bank University
London, United Kingdom

Supervisor: Prof. Mohammad Ghavami

September 2023

Abstract

Medical diagnosis and subsequent treatment efficacy hinge on innovative imaging modalities. Among these, Microwave Imaging (MWI) has emerged as a compelling approach, offering safe and cost-efficient visualization of the human body. This comprehensive research explores the potential of the Huygens principle-based microwave imaging algorithm, specifically focusing on its prowess in cancer, lesion, and infection detection. Extensive experimentation employing meticulously crafted phantoms validates the algorithm's robustness.

In the context of lung infections, this study harnesses the power of Huygens-based microwave imaging to detect lung-COVID-19 infections. Employing Microstrip and horn antennas within a frequency range of 1 to 5 GHz and a multi-bistatic setup in an anechoic chamber, the research utilizes phantoms mimicking human torso dimensions and dielectric properties. Notably, the study achieves a remarkable detection capability, attaining a signal-to-clutter ratio of 7 dB during image reconstruction using S21 signals. A higher SCR ratio indicates better contrast and clarity of the detected inclusion, which is essential for reliable medical imaging. It is noteworthy that this achievement is realized in free space without necessitating coupling liquid, underscoring the algorithm's practicality.

Furthermore, the research delves into the validation of Huygens Principle (HP)-based microwave imaging in detecting intricate lung lesions. Utilizing a meticulously designed multi-layered phantom with characteristics closely mirroring human anatomy, the study spans frequency bands from 0.5 GHz to 3 GHz within an anechoic chamber. The outcomes are compelling, demonstrating consistent lesion detection within reconstructed images. Impressively, the signal-to-clutter ratio post-artifact removal surges to 13.4 dB, affirming the algorithm's potential in elevating medical imaging precision.

To propel the capabilities of MWI further, this research unveils a novel device: 3D microwave imaging rooted in Huygens principle. Leveraging MammoWave device's capabilities, the study ventures into 3D image reconstruction. Dedicated phantoms housing 3D structured inclusions, each embodying distinct dielectric properties, serve as the experimental bedrock. Through an intricate interplay of data acquisition and processing, the study attains a laudable feat: seamless 3D visualization of inclusions across various z-axis planes, accompanied by minimal dimensional error not exceeding 7.5%.

In a parallel exploration, spiral-like measurement configurations enter the spotlight.

These configurations, meticulously tailored along the z-axis, yield promising results. The research unveils an innovative approach to reducing measurement time while safeguarding imaging fidelity. Notably, spiral-like measurements achieve a notable 50% reduction in measurement time, albeit with slight trade-offs. Signal-to-clutter ratios experience a modest reduction, and there is a minor increase in dimensional analysis error, which remains within the confines of 3.5%. The research findings serve as a testament to MWI's efficacy across diverse medical domains. The success in lung infection and lesion detection underscores its potential impact on medical diagnostics. Moreover, the foray into 3D imaging and the strategic exploration of measurement configurations lay the foundation for future advancements in microwave imaging technologies. As a result, the outcomes of this research promise to reshape the landscape of accurate and efficient medical imaging modalities.

Acknowledgements

The pursuit of this doctoral degree has been an extraordinary and transformative journey, one that I am acutely aware would not have been feasible without the unwavering support and guidance of numerous individuals. In light of this, I wish to express my profound gratitude for the invaluable contributions of those who have played an instrumental role in the successful culmination of this dissertation.

Foremost, I extend my sincere appreciation to my principal supervisor, Prof. Mohammad Ghavami. His steadfast guidance, insightful feedback, and unyielding encouragement have been the pillars on which my research journey has been built. His unceasing support has been a pivotal force that propelled me forward throughout the course of my PhD.

In equal measure, I am indebted to my esteemed technical supervisors, Dr. Gianluigi Tiberi and Dr. Navid Ghavami. Their unwavering encouragement, motivational guidance, and extensive expertise have been indispensable to the development of this project. Their mentorship and invaluable insights, spanning both research and thesis, have fostered my growth as a proficient research scientist. The realization of my research endeavors and the eventual completion of my dissertation would have been inconceivable without the steadfast tutelage of Dr. Gianluigi Tiberi and Dr. Navid Ghavami.

A debt of gratitude is also owed to Dr. Banafsheh Khalesi, whose consistent guidance, astute feedback, and unwavering support have been instrumental to this project and thesis. Her mentorship, spanning the continuum of my academic journey from my master's to this very juncture, has been a constant beacon.

The contributions of Prof. Sandra Dudley are equally deserving of recognition, her sagacious advice and financial support through the waiver of school fees are greatly appreciated. This generosity has profoundly impacted my journey, and I am deeply thankful.

I am also appreciative of the camaraderie and assistance provided by my friends, co-workers, and roommates at T-413. Special acknowledgment goes to Dr. Banafsheh Khalesi, whose presence has made my academic sojourn truly enriching.

Lastly, I extend heartfelt gratitude to my granddad, parents, siblings, and Muhammad Azeem for their unwavering belief in me and their unending encouragement to pursue my aspirations. A particularly profound thank you is extended to my beloved wife, whose steadfast support and assistance have been a cornerstone during the trials of this challenging period.

In conclusion, the collective contributions of these individuals have significantly enriched my academic voyage, and I am deeply humbled by their enduring support.

Publications

- **Bilal Khalid**, Banafsheh Khalesi, Navid Ghavami, Lorenzo Sani, Alesandro Vispa, Mario Badia, Sandra Dudley-Mcevoy, Mohammad Ghavami and Gianluigi Tiberi 2022. "3D Huygens Principle Based Microwave Imaging Through MammoWave Device: Validation Through Phantoms." IEEE Access, 10, pp.106770-106780.
- **Bilal Khalid**, Banafsheh Khalesi, Navid Ghavami, Sandra Dudley-Mcevoy, Mohammad Ghavami and Gianluigi Tiberi 2023. "Huygens Principle based Microwave Imaging for Lung Lesion Detection using Realistic Phantom" MDPI, Sensors, (Under Revision).
- **Bilal Khalid**, Banafsheh Khalesi, Navid Ghavami, Sandra Dudley-Mcevoy, Mohammad Ghavami and Gianluigi Tiberi, "3D Microwave Imaging Using Huygens Principle: A Phantom-based Validation," 2021 Photonics & Electromagnetics Research Symposium (PIERS), Hangzhou, China, 2021, pp. 2892-2896,IEEE Xplore.
- **Bilal Khalid**, Banafsheh Khalesi, Navid Ghavami, Giovanni Raspa, Mario Badia, Sandra Dudley-Mcevoy, Mohammad Ghavami and Gianluigi Tiberi, 2023, July." A Spiral-like Acquisition Strategy for 3D Huygens' Principle Based Microwave Imaging". In Photonics & Electromagnetics Research Symposium (Piers) 2023,IEEE Xplore.
- Banafsheh Khalesi, **Bilal Khalid**, Navid Ghavami, Mohammad Ghavami, Sandra Dudley-Mcevoy and Gianluigi Tiberi 2021, November." Microwave Imaging for Lung COVID-19 Infection Detection through Huygens Principle. "In 2021 Photonics & Electromagnetics Research Symposium (PIERS) (pp. 2885-2891),IEEE Xplore.
- Banafsheh Khalesi, **Bilal Khalid**, Navid Ghavami, Giovanni Raspa, Mohammad Ghavami, Sandra Dudley-Mcevoy and Gianluigi Tiberi, 2022. "A Microwave Imaging Procedure for Lung Lesion Detection: Preliminary Results on Multilayer Phantoms." Electronics, 11(13), p.2105,IEEE Xplore.

List of Abbreviations

2D Two-Dimensional

3D Three-Dimensional

CT Computed Tomography

GUI Graphical user interface

HP Huygens Principle

MI Medical Imaging

MRI Magnetic Resonance Imaging

MWI Microwave Imaging

SCR Signal to Clutter Ratio

TSL Tissue Simulating Liquids

UWB Ultra-Wideband

VNA Vector Network Analyser

WHO World Health Organization

List of Symbols

ε_r Dielectric constant

σ Conductivity

f Frequency

a_0 Radius of Cylinder

I Intensity

Δs Spatial sampling

k_1 Wave number

$\vec{\rho}$ Observing Points

\mathbf{G} Green's function

λ Wavelength

\mathbf{tx} Transmitting antenna

\mathbf{rx} Receiving antenna

Z_h Multiple heights along the z-axis

List of Figures

2.1	X-rays Device [2].	26
2.2	X-rays-based Computed Tomography Device [3].	27
2.3	Ultrasound Device [4].	28
2.4	The MRI Device [5].	29
2.5	The Indoor Spectrum allocated by FCC [7, 8].	33
2.6	Detailed UWB Communication System Block Diagram [9].	34
2.7	Microwave Imaging Techniques Comparative Analysis.	38
3.1	The PulsON P200 UWB Antenna [38].	51
3.2	(a) The Planner UWB Horn Antenna, (b) Antenna Pattern [40].	52
3.3	The Vector Network Analyser, MS2028C Anritsu.	54
3.4	The pictorial view, where red dots show receiving points and black dot transmitting position.	57
3.5	Design of lung COVID-19 infection Phantom.	62
3.6	The lung COVID-19 infection fabricated phantom.	64
3.7	(a) Pictorial view of the measurement set up; (b) Position of the torso phantom inside the anechoic chamber. The phantom was placed on the centre of a rotatable table. The external UWB antenna is the transmitter, and the internal PulsON P200 antenna is the receiver.	65
3.8	Pictorial view of the measurements.	66

3.9	Microwave image of the human torso phantom employing frequency range of 1-5 GHz after performing rotation subtraction artifact removal procedure using the difference between measurements obtained with transmitting positions 0° and 5°; Images are obtained following normalization to their correspondent maximum values and forcing to zero the intensity values below 0.5 (x and y axes are given in meters); the blue elliptical shows boundary of the phantom and red circle represents the possible detected infection.	68
3.10	Microwave image of the human torso phantom employing frequency range of 1-5 GHz; after performing “ideal” artifact removal procedure; using the difference between obtained data of a healthy torso phantom and the data of torso phantom having lung infection. Images are obtained following normalization to their correspondent maximum values and forcing to zero the intensity values below 0.5 (x and y axes are given in meters);the blue elliptical shows boundary of the phantom and red circle represents the possible detected infection.	70
3.11	Multi-layered chest phantom V1 by SPEAG.	73
3.12	Top view of filled multi-layered SPEAG chest phantom.	74
3.13	Experimental Setup inside Anechoic Chamber.	75
3.14	Experimental Schematics.	76
3.15	Experimental Schematics (with amplifier).	77
3.16	Reconstructed Image with the detected inclusion (before image adjustment).	77
3.17	Reconstructed Image with the detected inclusion (after image adjustment).	78
3.18	(a) Reconstructed Image with the detected inclusion & underlined margin of the phantom (before image adjustment), (b) Reconstructed Image with the detected inclusion & underlined margin of the phantom (after image adjustment).	79
4.1	Initial MammoWave prototype [75].	85
4.2	Current MammoWave prototype [77].	86
4.3	MammoWave installed at London South Bank University.	87
4.4	2-port VNA (M5065).	87
4.5	Experimental Configuration.	88

4.6	Fabricated Multilayered Phantom [61].	91
4.7	Obtained microwave images of anechoic chamber phantom experiments using frequency 1 GHz to 5 GHz, (a) applying “rotation subtraction” method, (b) employing the “ideal” method. The light green ellipse indicates the phantom region, while the area marked with a red circle shows the exact position of inclusion and the dimension of the circle is in relation to the dimension of the inclusion. Axes scales are meters.	93
4.8	Obtained microwave images of MammoWave device phantom experiments using frequency 1 GHz to 6.5 GHz, (a) applying “rotation subtraction” method, (b) employing the “ideal” method. The light green ellipse indicates the phantom region, while the area marked with a red circle shows the exact position of inclusion and the dimension of the circle is in relation to the dimension of the inclusion. Axes scales are meters.	94
4.9	(a) Depict the fabricated re-miniaturized torso phantom, the position of the torso phantom inside the MammoWave device, (b) the S21 for both the phantom with and without inclusions, (c) calculated when the transmitting antenna is Tx1 and the receiving antenna is 180° apart, respectively. . . .	95
4.10	Reconstructed images of the lung phantom with two inclusions. (a, b) represent the images corresponding to applying the “rotation subtraction” artefact removal method and “ideal” artefact removal method, respectively. The light green ellipse indicates the phantom region, while the areas marked with red circles show the exact positions of the inclusions and the dimension of each circle is in relation to the dimension of the inclusion. Axes’ scales are meters.	96
5.1	(a) MammoWave microwave imaging device having a cylindrical hub and the phantom holder, (b) experimental schematic i.e., fabricated phantom inside phantom holder with changing heights of antennas for multiple cross-sectional analysis along the z-axis.	103
5.2	(a) Fabricated phantom, (b) 3D structured inclusion.	105
5.3	Fabricated head phantom.	105
5.4	Fabricated 3-layer phantom (left) and the experimental setup (right). . . .	107

5.5	Pictorial view of the measurement process, where grey coloured circle represents the fabricated phantom, light blue dots indicate the receiving points, small yellow circle shows the inclusion. The outer dashed black circle shows the transmitting antenna perimeter with dark circles in sets of three showing the transmitter triplets.	108
5.6	Microwave images with detected inclusion at reference planes: (a) h=1, (b) h=2, (c) h=3, (d) h=4, (e) h=5, (f) h=6. Axes units are meters.	113
5.7	Normalized and adjusted microwave images with highlighted inclusion at reference planes: (a) h=1, (b) h=2, (c) h=3, (d) h=4, (e) h=5, (f) h=6. Axes units are meters.	115
5.8	Normalized and adjusted microwave images with highlighted inclusion at reference planes: (a) h=1, (b) h=2, (c) h=3, (d) h=4, (e) h=5, (f) h=6. Axes units are meters.	116
5.9	Microwave images with detected inclusion (circled) at h=2, 4 and 6. Axes units are meters.	119
5.10	Normalized and adjusted Microwave images with detected inclusion (permittivity increased by a factor of 4) at h=2, 4 and 6. Axes units are meters.	120
5.11	Normalized and adjusted Microwave images with detected inclusion (permittivity and conductivity increased by factors of 4 and 2, respectively) at h=2, 4 and 6. Axes units are meters.	120
5.12	Microwave images with detected inclusion at reference planes (head-phantom): (a) h=1, (b) h=2, (c) h=3, (d) h=4, (e) h=5, (f) h=6. Axes units are meters.	124
5.13	Normalized and adjusted microwave images with detected inclusion at reference planes (head-phantom): (a) h=1, (b) h=2, (c) h=3, (d) h=4, (e) h=5, (f) h=6. Axes units are meters.	125
5.14	3D Visualization of the detected inclusion in multiple cross-sections along the z-axis (head-phantom) after normalization and image adjusting. Axes units are meters.	125
5.15	Microwave images with detected inclusion at reference planes (3-layer phantom): (a) h=1, (b) h=2, (c) h=3, (d) h=4, (e) h=5, (f) h=6. Axes units are meters.	127

5.16	Normalized and adjusted microwave images with detected inclusion at reference planes (3-layer phantom): (a) h=1, (b) h=2, (c) h=3, (d) h=4, (e) h=5, (f) h=6. Axes units are meters.	128
5.17	3D Visualization of the detected inclusion in multiple cross-sections along the z-axis (3-layer phantom) after normalization and image adjusting. Axes units are meters.	128
6.1	The multilayered fabricated phantom with 3D structured inclusion.	134
6.2	(a) Spiral-like acquisition configuration, (b) The experimental schematic, (c) MWI device MammoWave.	135
6.3	(a) Reconstructed microwave images with detected inclusion at reference planes (when employing all receiving points at each height), (b) 3D reconstructed image. Images are produced after normalization and image adjustment. Axes units are meters.	138
6.4	(a) Reconstructed microwave images with detected inclusion at reference planes (spiral-like acquisition Configuration-I), (b) 3D reconstructed image, Images are produced after normalization and image adjustment. Axes units are meters.	139
6.5	(a) Reconstructed microwave images with detected inclusion at reference planes (spiral-like acquisition configuration-II), (b) 3D reconstructed image. Images are produced after normalization and image adjustment. Axes units are meters.	140
6.6	Reconstructed microwave images with detected inclusion at h_4 , h_5 , and h_6 using: (a) original setup, (b) spiral-like acquisition configuration-I, (c) spiral-like acquisition configuration-II.	142
6.7	Reconstructed images resulting from the novel spiral acquisition configuration at multiple planes along the z -axis.	146
1	Extraction of 'prcd' files via MATLAB.	167
2	Defining Parameters.	167
3	Defining Parameters (Grid for Reconstruction).	168
4	Defining Parameters (Freespace and Frequency).	168
5	3D Visualisation Code sample.	169

List of Tables

3.1	Characterisation of PulsON P200 [38].	51
3.2	Relative permittivity and conductivity at a frequency of 2 GHz.	63
3.3	Dielectric Properties of Fabricated Materials at 1.75 GHz.	74
4.1	SCR for microwave images of phantom measurements in both the anechoic chamber (chapter 3) and MammoWave device.	92
5.1	Relative permittivity and conductivity of fabricated materials at 2 GHz [52, 101].	104
5.2	Signal to clutter at multiple planes along the z-axis.	117
5.3	Dimensional analysis and error % calculations at multiple planes.	118
5.4	Signal to clutter comparison with increased values of ϵ & σ at multiple planes along the z-axis.	121
5.5	Localization error comparison between free space parameters and increased values of ϵ & σ at multiple planes along the z-axis.	123
6.1	Dielectric properties of materials used in phantom fabrication.	133
6.2	Signal to Clutter Ratio Comparison for all three scenarios.	143
6.3	Dimensional Analysis Error Comparison for all three scenarios.	144
6.4	Localization Error Comparison for all three scenarios.	144

Contents

1	Introduction	17
1.1	Research Motivation	17
1.2	Aim and Objectives of the Research	19
1.3	Innovative Contributions	20
1.4	Thesis Structure	22
2	Literature Review	25
2.1	Introduction	25
2.2	Existing Imaging Diagnostic Technologies	25
2.2.1	X-Rays Based Computed Tomography	26
2.2.2	Ultrasound	27
2.2.3	Magnetic Resonance Imaging	28
2.3	UWB History and Fundamentals	30
2.3.1	UWB Medical Applications	34
2.4	Microwave Imaging	35
2.4.1	Dielectric Properties	36
2.4.2	Microwave Tomography	36
2.4.3	Microwave Imaging Algorithms	37
2.5	Introduction to Cancer	39
2.5.1	Breast Cancer	40
2.5.2	Lung Cancer	41
2.5.3	Brain Tumour	41
2.6	Evolution of Microwave Imaging for Lesion Detection	43
2.6.1	Breast Cancer Detection via MWI	43
2.6.2	Lung Lesion Detection via MWI	44

2.6.3	Brain Lesion/Stroke Detection via MWI	45
2.7	Research Gap and Proposed Research	46
2.8	Summary	48
3	Initial Technical Approach for MWI	49
3.1	Introduction	49
3.2	Experimental Setup	50
3.2.1	UWB PulsON P200	50
3.2.2	Planner UWB Horn Antenna	52
3.2.3	Vector Network Analyser	53
3.2.4	Rotating Stand and Table	55
3.3	Huygens Principle Based MWI Algorithm	55
3.4	Lung COVID-19 Infection Detection via UWB MWI	60
3.4.1	Lung Phantom Fabrication	61
3.4.2	Experimental Methodology	64
3.4.3	HP-based Imaging Algorithm	65
3.4.4	Reconstructed Images	67
3.4.5	Experimental Analysis	69
3.5	Lung Lesion Detection via MWI Implementing Realistic Parameters	71
3.5.1	Phantom Fabrication	72
3.5.2	Measurement Setup inside Anechoic Chamber	74
3.5.3	Image Reconstruction	76
3.5.4	Experimental Analysis	80
3.6	Summary	81
4	Advanced MWI Device	83
4.1	Introduction	83
4.2	Introduction to MammoWave	84
4.3	Imaging Algorithm	88
4.4	MammoWave Validation	89
4.5	Lung Lesion Detection via MammoWave (Preliminary Results)	90
4.5.1	Phantom Fabrication and Experimental Configuration	91
4.5.2	Reconstructed Images	92

4.6	Summary	95
5	3D Huygens Principle based Microwave Imaging through MammoWave Device.	98
5.1	Introduction	98
5.2	Background of Proposed Research	99
5.3	Experimental Configuration	101
5.3.1	Device and Methodology	101
5.3.2	Phantoms Fabrications	103
5.3.3	Imaging Procedure	107
5.4	Results and Discussions	111
5.4.1	2-layer Phantom Results	112
5.4.2	Image Quantification	117
5.4.3	Skull Mimicking Phantom Results	123
5.4.4	3-layer Phantom Results	126
5.5	Summary	127
6	A Spiral-like Acquisition Strategy for 3D Huygens' Principle Based Microwave Imaging	130
6.1	Introduction	130
6.2	Experimental Insights	131
6.3	Methodology	133
6.3.1	Device and Imaging Procedure	134
6.4	Results and Discussions	138
6.5	Summary	147
7	Conclusions and Future Work	149
7.1	Conclusions	149
7.2	Recommendations for Future Work	151
7.2.1	Enhancement Prospects in Lung Lesion Detection	151
7.2.2	Advancements in 3D Visualization	152
7.2.3	Strategies for Improving Time Reduction in Microwave Imaging	152

Chapter 1

Introduction

This chapter exhibits the research motivation, outlines the proposed aim, and objectives. It also provides an overview of the thesis structure, guiding the reader through its sections and chapters.

1.1 Research Motivation

Medical imaging (MI) is an indispensable tool used to visualize the interior of the human body for diagnostic and various medical purposes. Its significance lies in its ability to aid in the identification of diseased areas, leading to improved chances of early-stage disease detection and facilitating effective treatment monitoring. Conventional MI technologies, including X-rays, magnetic resonance imaging (MRI), ultrasound, and computed tomography (CT), have revolutionized the medical industry, saving countless lives. Over the years, X-rays have undergone significant evolution since their introduction about 126 years ago [1]. While these technologies serve diverse applications, they are not without limitations, particularly in the detection of cancer or tumours. X-rays and CT scans involve the use of ionizing radiation, which can pose health risks if used excessively. Additionally, ultrasound faces challenges in penetrating bones and generating high-contrast images, often requiring specialized medical expertise and costly equipment. Meanwhile, MRI scans can be time-consuming, taking up to 45-60 minutes per scan, and the image reconstruction process is dependent on the completion of all scans [2]. The operation of MRI hardware also demands skilled professionals, and the equipment itself is bulky and expensive.

The increasing number of cancer patients each year underscores the importance of research aiming to detect cancer at an early stage to facilitate easier and more successful treatment. Cancer emerges due to genetic changes that disrupt the orderly process of cell growth, leading to the rapid proliferation of abnormal cells. The limitations of conventional MI techniques have motivated researchers to explore alternative approaches that offer higher efficiency, lower costs, and pose no health risks by avoiding the use of ionizing rays.

In recent years, the development of ultra-wideband (UWB) based microwave imaging (MWI) has shown promise, overcoming some limitations of conventional MI technologies through continuous research efforts worldwide. UWB technology in MWI offers superior resolution and reduced multipath interference, enabling precise spatial information retrieval and improved imaging accuracy in complex environments.

When UWB signals are compared with conventional narrowband (NB) signals, the key distinctions between them becomes apparent. A notable characteristic of UWB signals is their significantly lower power spectrum. This reduction in power spectrum is attributed to the extensive bandwidth occupied by UWB signals, which introduces the possibility of interference with other communication systems. However, it is important to note that achieving a high power spectral density is not a requirement for UWB signals. As a result, the power spectrum of UWB is intentionally diminished. MWI operates on the basic principle of differentiating healthy and malignant tissues based on their dielectric properties. Notably, cancerous tissues exhibit different dielectric properties compared to healthy tissues, allowing MWI to effectively locate tumours at an early stage. A wide range of MWI methodologies have emerged, with some even progressing to clinical trials, reflecting the potential of this technology to transform medical imaging and cancer detection, as discussed in this thesis.

The focus of the proposed research is to validate the capability of the existing Huygens principle (HP) based MWI algorithm in detecting cancer at an early stage. The research involves conducting experiments on fabricated phantoms, each with varying dielectric properties, to comprehensively evaluate the algorithm's effectiveness. Additionally, the study aims to develop a cutting-edge 3D MWI algorithm, enabling the visualization of detected malignant tissues in three dimensions, providing crucial information about their dimensions and spatial distribution.

Looking towards the future, the research envisions the construction of a dedicated MWI device, a modified version of the MammoWave, for use in clinical trials specifically targeted at lung imaging. This device offers the advantage of monitoring lung lesions without relying on X-rays, thereby ensuring patient safety. Moreover, its portability and simplified structure could make it an ideal candidate for conducting remote pre-hospital examinations. Furthermore, as the output power may be increased in future experiments, my plan is to monitoring specific absorption rate (SAR) to ensure adherence to safety guidelines. With these objectives and prospects, the proposed research contributes to the advancement of medical imaging technology and the potential for early cancer detection, bringing hope for better patient outcomes and improved healthcare services. As the research progresses, the scientific community eagerly awaits the development of MWI as a transformative tool in medical imaging, saving lives and improving the quality of healthcare globally.

1.2 Aim and Objectives of the Research

The overall aim of this thesis is to extend the 2D HP-based imaging algorithm into a 3D version, leveraging the MWI device for enhanced visualization capabilities, especially when dealing with intricate structures and tumors in different planes along the z-axis. The objectives of this research are as follows:

- Explore the potential of the HP-based MWI algorithm for detecting cancer.
- Conduct experiments on fabricated phantoms for lung lesion and lung COVID-19 infection detection.
- Investigate the ability of a novel HP-based MWI device, initially designed for breast cancer detection, to detect lung lesions using realistic fabricated phantoms.
- Rigorously validate the proposed procedure, employing various quantification methods and introducing complexities to experimental setups, including the use of realistic phantoms and fabrication mixtures.

The methodology involves testing the 3D imaging algorithm using three distinct fabricated phantoms, each representing different challenges and complexities: 3D structured

inclusions, asymmetrical phantom shapes with uniform inclusions, and variations in dielectric properties along the z-axis. A detailed analysis of the reconstructed images obtained through the 3D imaging algorithm is conducted, utilizing various image quantification methods to assess the performance of the MWI technique in detecting and characterizing cancerous tissues.

Additionally, this research aims to reduce imaging time by introducing a novel spiral-like acquisition method. By optimizing the data acquisition process, this approach shows promising potential for enhancing the efficiency and practicality of MWI devices in clinical settings.

In summary, this thesis contributes to advancing the field of microwave imaging for cancer detection and diagnosis by developing a 3D imaging algorithm, exploring the capabilities of the HP-based MWI algorithm, and validating its performance through extensive experiments. The ultimate goal is to pave the way for more effective and efficient cancer detection techniques, with potential applications in various medical fields, leading to improved patient outcomes and healthcare practices.

1.3 Innovative Contributions

The achievements of this research are of significant importance in the field of medical imaging, particularly developing 3D MWI algorithm for 3D visualisation and detecting lung infections and malignant tissues using the Huygens Principle (HP) based MWI algorithm. The research involved various steps and experiments on fabricated phantoms with inclusions having varied dielectric properties. These achievements are outlined as follows:

- **Fabrication of Multiple Phantoms:** One of the key achievements is the successful fabrication of multiple phantoms that simulate lung conditions. This includes fabricating oval-shaped multi-layered lung phantoms that accurately mimic the human torso for detecting lung COVID-19 infection. Using appropriate materials with correlated dielectric properties to the lung is crucial for achieving accurate results. Another achievement is fabricating dedicated phantoms with tissue-simulating liquid, including realistic components. Specifically, a multi-layered chest phantom, designed by SPEAG, is used to validate the proposed methodology further. The realistic dimensions and outer layer of the phantom, mimicking the skin, contribute

to the accuracy and reliability of the validation process. Efforts are made to enhance the complexity of the phantoms by incorporating fabricated inclusions. This increases realism and provides more accurate representations of real-life scenarios, making the experiments more reliable and informative..

- **Validation of Proposed Methodology:** The research also involves the validation of the proposed MWI methodology. An experimental setup with the required hardware for MWI is carefully formatted, and experiments are performed inside an anechoic chamber on the fabricated phantom for detecting fabricated infections.
- **3D MWI Algorithm Development:** A major milestone in the research is the successful development of a novel 3D MWI algorithm based on the Huygens principle. The proposed MWI algorithm extends the image reconstruction capabilities from 2D to 3D, aiming for improved visualization details. This algorithm represents a significant advancement in MWI technology, allowing for more detailed and informative 3D visualizations of detected inclusions and malignant tissues.
- **Successful 3D Visualization:** Through meticulous measurements on the designed and fabricated phantoms, the 3D MWI algorithm demonstrates its capability for successfully detecting and visualizing inclusions with varying dimensions. The ability to visualize the detected abnormalities in three dimensions may provide valuable insights for medical professionals, enabling more accurate diagnosis and treatment planning.
- **Image Quantification Validation:** To ensure the reliability and accuracy of the 3D imaging algorithm, the research includes a detailed validation process using image quantification methods. These methods are applied to the reconstructed images, confirming the algorithm's effectiveness and robustness.
- **Time Reduction Methodology:** The researchers also introduce a novel methodology for achieving imaging time reduction using the 3D MWI algorithm based on HP with the MammoWave device. By fabricating a three-layer cylindrical phantom with a 3D structured inclusion and employing various spiral-like measurement scenarios along the z-axis, they achieve a 50% reduction in imaging time with minimal error. This methodology has promising implications for expediting medical imaging procedures

and enhancing patient care.

In conclusion, the achievements presented in this research signify advancements in the field of microwave imaging, particularly in the detection of lung infections and malignant tissues. The successful fabrication and validation of multiple phantoms, the development of a state-of-the-art 3D MWI algorithm, and the introduction of a time reduction methodology all contribute to the field's growth and innovation. These achievements have the potential to revolutionize medical imaging practices, leading to improved healthcare outcomes and enhanced patient care.

1.4 Thesis Structure

This thesis encompasses seven chapters, each contributing significant advancements to the fields of medical imaging (MI) and microwave imaging (MWI). The chapters are structured as follows:

- Chapter 1: This chapter provides the summary of the research motivation behind the proposed work, emphasizing the original contributions made throughout the study. It serves as an introduction to the thesis, laying the groundwork for the subsequent chapters by highlighting the significance and relevance of the research.
- Chapter 2: In this chapter, a detailed literature review is presented, delving into existing MI technologies and their respective advantages and limitations. The historical background and capabilities of UWB technology in medical applications are explored in depth. Furthermore, the chapter introduces MWI as a novel approach for medical imaging and examines various existing MWI algorithms and methodologies, providing a thorough understanding of the state-of-the-art in the field.
- Chapter 3: This chapter focuses on the proposed MWI experimental setup, particularly the one implemented in the anechoic chamber at London South Bank University (LSBU). It offers a detailed description of the hardware utilized in the setup and introduces the MWI algorithm based on the Huygens principle. The fabrication of two complex multi-layered lung phantoms is thoroughly explained, with one designed to detect COVID-19 infection and the other representing more realistic parameters, dimensions, and dielectric properties. The imaging algorithm

and methodology for both scenarios are detailed, with variations in hardware setup discussed in relation to their respective contributions.

- Chapter 4: This chapter introduces a novel, fast, and accurate MWI device named MammoWave, designed for breast screening by UBT Srl Italy. The basic hardware of the device and two experimental configurations are explained in detail. The chapter emphasizes the device's capabilities in clinical trials, showcasing successful results and the potential for significant advancements in medical imaging. Additionally, the device is subjected to various experimentations, providing valuable insights for future modifications and enhancements. The extension of the HP-based imaging algorithm for lung lesion detection is also thoroughly covered, showcasing the device's versatility in multiple medical applications.
- Chapter 5: Focusing on the development of a 3D MWI algorithm based on HP, this chapter explores the utilization of the MammoWave device for extending image reconstruction from 2D to 3D. Dedicated phantoms with 3D structured inclusions and varying dielectric properties are meticulously prepared, and measurements are taken at multiple planes along the z-axis. The chapter demonstrates the successful detection and 3D visualization of the inclusion at various planes/cross-sections along the z-axis, showcasing the algorithm's robustness and reliability. Furthermore, a detailed analysis of quantification techniques validates the device's capabilities and the efficacy of the proposed 3D imaging algorithm.
- Chapter 6: This chapter introduces a novel methodology for achieving imaging time reduction using the 3D imaging HP algorithm with the MammoWave device. A three-layer cylindrical phantom with a 3D structured inclusion and varying dielectric properties is fabricated to evaluate the device's performance. Spiral-like measurement scenarios along the z-axis are implemented, and a detailed analysis of the proposed methodology is presented, demonstrating the potential for enhanced efficiency in medical imaging. Image quantification validates the results, establishing the optimal configuration achieving time reduction with minimal error.
- Chapter 7: In the final chapter, the conclusion of the proposed research is presented, summarizing the achieved deliverables and significant contributions made

throughout the thesis. The chapter highlights the successful advancements in medical imaging and MWI technology, with a focus on the potential impact on healthcare outcomes. Recommendations for future work and potential areas of further exploration are also provided, encouraging continued research and innovation in the field.

Throughout this thesis, a wealth of knowledge and significant achievements have been made, advancing the field of medical imaging and MWI technology. The original contributions, novel methodologies, and cutting-edge devices presented in this thesis promise to revolutionize the field of medical imaging, opening doors for improved healthcare diagnostics, treatment, and patient outcomes.

Chapter 2

Literature Review

2.1 Introduction

In this chapter, a thorough analysis of the current medical imaging technologies is presented, followed by an introduction to the UWB technology and its historical context in medical applications. Additionally, the chapter delves into the existing MWI algorithms and evolution of MWI as an alternative imaging approach. Existing MWI methodologies are discussed, along with an exploration of their limitations and challenges. This chapter aims to provide a solid foundation for understanding the context and motivation behind the proposed MWI research, highlighting the need for advancements in medical imaging techniques.

2.2 Existing Imaging Diagnostic Technologies

Medical imaging is a crucial tool for visualizing the human body's internal structures and aiding in accurate diagnosis and treatment. Conventional techniques such as X-ray imaging, ultrasound, CT, and MRI have their advantages but also come with limitations and potential health risks [1]. X-ray and CT scans use ionizing radiation, raising concerns about repeated exposure. Ultrasound is safer but has limitations in image quality and operator dependency. MRI provides excellent soft tissue contrast but is time-consuming and expensive.

To overcome these limitations, researchers have explored the potential of UWB based MWI as an alternative approach. MWI utilizes differences in tissues' dielectric properties

for cancer and tumour detection, without using ionizing radiation or invasive procedures. This non-ionizing and non-invasive technique holds promise for enhancing medical imaging capabilities and reducing health risks associated with conventional methods. In summary, while conventional medical imaging techniques have greatly improved healthcare, MWI offers the prospect of overcoming their limitations and revolutionizing medical imaging with safer and more efficient imaging procedures.

2.2.1 X-Rays Based Computed Tomography

X-ray imaging, a pioneering discovery in the medical field over a century ago, continues to be a prominent and widely utilized diagnostic methodology. Its ability to visualize bones and select soft tissues is highly valuable, albeit somewhat limited in distinguishing between different tissue densities. The application of X-rays involves the use of ionizing radiation, and in more complex procedures such as CT scans, the radiation levels may be relatively higher, resulting in increased costs [2]. While the potential risk to the human body from X-ray radiation is generally considered minimal, it is essential to exercise caution and recognize that it cannot be entirely disregarded as devoid of any health risks. Nevertheless, X-rays serve as a crucial diagnostic tool, effectively passing through tissues to provide clear differentiation of various anatomical structures, as depicted in Figure 2.1.



Figure 2.1: X-rays Device [2].

The use of X-rays demands not only skilful execution but also strict adherence to safety measures due to the bulky nature of the equipment and its need for regular mainte-

nance, contributing to the overall expenses of this imaging modality [3]. On the contrary, CT imaging employs an array of low X-ray radiation sources, revolving around the patient, while a sophisticated computer reconstructs this data to produce a comprehensive diagnostic output. While CT scans are highly adept at detecting cancer and other anomalies, the use of higher radiation levels poses potential health risks to patients, warranting careful consideration and medical supervision. Moreover, in certain cases, CT scans may necessitate intravenous access and sedation, adding to the complexity and patient discomfort. As depicted in Figure 2.2, the increased capabilities of CT imaging come with a higher price tag compared to standard X-ray machines, making it a relatively expensive option for medical facilities.



Figure 2.2: X-rays-based Computed Tomography Device [3].

2.2.2 Ultrasound

Another well-established medical imaging technology is ultrasound, which utilizes high-frequency non-ionizing compressional waves, commonly known as ultrasounds [3]. Ultrasound imaging employs sound waves with frequencies ranging from 2 to over 10 MHz, as these waves travel through the body and bounce back from internal organs, their echoes are captured and converted into images [2]. However, this imaging modality also comes with its own set of limitations. For instance, ultrasound is unable to penetrate through bones, which hinders its ability to visualize high-contrast images of bony structures. Additionally, to achieve higher contrast and optimal imaging, lower frequencies are necessary, which in turn can lead to reduced resolution.

Over time, advancements have been made to enhance the quality of ultrasound images; however, this has often been accompanied by increased complexity and cost [4]. Moreover, ultrasound machines (as depicted in Figure 2.3) are typically more expensive than X-ray machines, and the quality of the images heavily relies on the proficiency of the operator. Nevertheless, ultrasound does provide the advantage of real-time evaluation of soft tissues and vessels [2].



Figure 2.3: Ultrasound Device [4].

2.2.3 Magnetic Resonance Imaging

MRI (Figure .2.4) is a renowned imaging technology in the medical field nowadays; it is a form of nuclear magnetic resonance utilizing magnetic field gradients to generate images. Currently, MRI, with its impressive 40,000-unit installations worldwide, stands out as a prominent medical imaging technique used for a wide range of diagnostic purposes [4]. However, this imaging modality does come with certain limitations that must be considered. One of the most significant drawbacks of MRI is the cost and time involved in the procedure. Unlike other imaging methods, MRI is not suitable for emergency

situations due to its time-consuming nature, especially when dealing with injuries to the spinal cord or brain strokes resulting from accidents. Patients undergoing an MRI scan must remain within the magnetic field area for an extended period, which can cause feelings of claustrophobia, particularly in individuals sensitive to confined spaces, and the magnetic field's impact on nearby metal objects [5]. Another factor contributing to the time-consuming aspect of MRI is the necessity for multiple sessions to complete a full scan. Each session may take between 45 to 60 minutes, and image reconstruction can only begin once all sessions are completed [5]. Additionally, the equipment used for MRI scans is both expensive and bulky, requiring skilled professionals to operate it effectively. This limitation may limit accessibility for certain patients and healthcare facilities [5]. Despite these drawbacks, MRI remains an invaluable imaging tool in the medical field, enabling the visualization of a wide range of morphological areas. Its non-invasive nature and ability to produce detailed images of soft tissues make it indispensable for various diagnostic purposes, such as detecting tumours, injuries, and abnormalities within the body. Ongoing advancements in MRI technology continue to improve its efficiency and image quality, making it an essential component of modern healthcare practices [2].

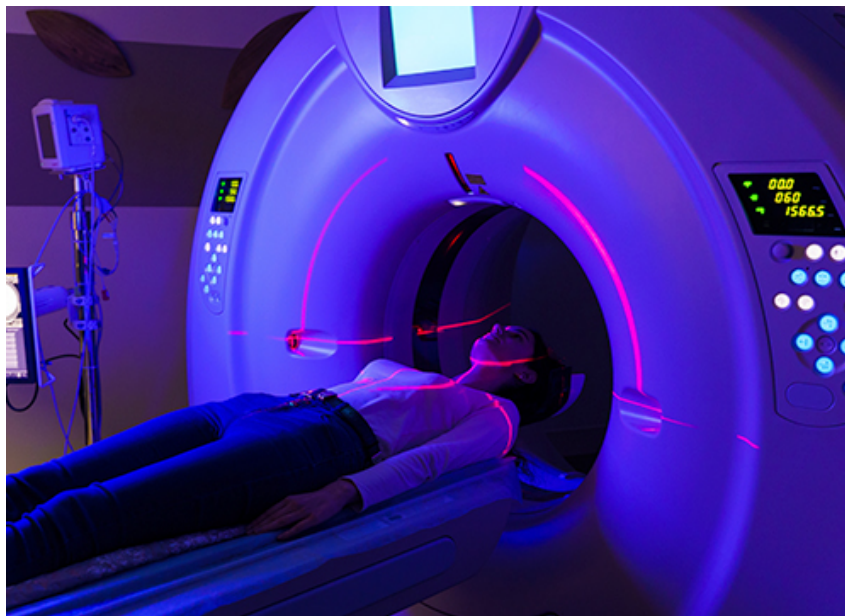


Figure 2.4: The MRI Device [5].

2.3 UWB History and Fundamentals

UWB technology has a long and storied history, dating back to 1973 when the first US patent for UWB communications was submitted by the Sperry research centre. This patent introduced a novel transmission and reception system for short-duration impulses, setting the stage for the widespread applications of UWB technology [6]. In the following years, UWB continued to garner attention, leading to around 50 patents related to various fields of UWB applications by the Sperry research centre in 1989 [6]. Over time, UWB technology underwent significant transformations, earning itself various names such as short-pulse, impulse, and fast frequency chirp. It is characterized by its ability to operate in an ultra-wideband spectrum for short periods. Initially, UWB was primarily utilized for military purposes, including sensing, military communications, and niche applications. However, a major turning point in the history of UWB came in February 2002 when the Federal Communications Commission (FCC) allowed its commercial use for data communications and radar applications. This decision granted UWB a vast spectrum, 1500 times larger than the Universal Mobile Telecommunication System (UMTS) license, effectively elevating UWB into mainstream use [7].

The FCC's approval of UWB for commercial applications opened up new possibilities for the technology, particularly in the domain of indoors, short-range, and accurate communications. This development was warmly welcomed by researchers and industry professionals alike, propelling UWB into the forefront of cutting-edge technologies [7]. For a signal to meet the classification of a UWB signal, it must adhere to specific criteria. It should either have a bandwidth of at least 500 MHz, or it must demonstrate a fractional bandwidth exceeding 20% within the range delineated by the FCC. The fractional bandwidth (B_f) is precisely defined by the equation:

$$B_f = 2 \left(\frac{f_H - f_L}{f_H + f_L} \right), \quad (2.1)$$

where f_H and f_L represent the upper and lower -10 dB frequencies of the signal spectrum, respectively. This equation captures the essence of UWB signals, highlighting their capacity to occupy a broad frequency spectrum, as mandated by regulatory standards [8] [9]. The frequency domain representation of a generic UWB signal can be expressed using its

fourier transform corresponding to a rectangular pulse in the time domain.

$$S(f) = A \cdot \text{sinc} \left(\frac{B}{2} \cdot (f - f_c) \right) \cdot e^{-j2\pi f t_0} \quad (2.2)$$

where:

$S(f)$: UWB signal in the frequency domain,

A : Amplitude of the signal,

B : Bandwidth of the signal,

f_c : Central frequency of the signal,

$\text{sinc}(\cdot)$: Sinc function,

j : Imaginary unit,

f : Frequency variable,

t_0 : Time offset.

UWB's applications expanded beyond its military roots, and it began to find widespread use in various consumer electronics, wireless communication systems, and other industrial applications. Today, UWB continues to evolve and make its mark as a unique and beneficial technology with a wide range of applications across diverse industries. Researchers and engineers continue to invest their time and efforts in further advancements, ensuring that UWB remains at the forefront of technological innovation. With its ever-increasing capabilities and potential, UWB is expected to play a pivotal role in shaping the future of communication and sensing technologies. UWB wide-spectrum impulse radio system is an optimal choice for short-range communications in dense multipath environments, providing secure and risk-free data transfer. The advantages of UWB technology are diverse and highly valuable [8]:

High Data Rates with Low Power Consumption: UWB excels in delivering high data rates while maintaining low power consumption. This characteristic ensures efficient data transfer even in noisy and challenging environments, making it a power-efficient option for various applications.

Secure Communications with Low Power: UWB technology ensures secure communication with minimal power consumption, making it an attractive option for applications

where data security is paramount.

Cost-Effectiveness and Low Operational Power: UWB devices are known for their cost-effectiveness, and the operational power required for UWB systems is minimal, resulting in overall cost savings.

Minimal Hardware Requirements: UWB technology necessitates relatively simple and minimal hardware, making it easier to implement and deploy in various scenarios.

Multiple User Access: The wide spectrum available to UWB allows multiple users to access the system simultaneously without significant interference, increasing its efficiency and usability in crowded environments.

Precise Indoor Positioning: UWB's ability to provide accurate indoor positioning and location tracking enhances its applicability in various industries, including asset tracking and indoor navigation.

Resilience to Interference: UWB signals are robust and resistant to interference, ensuring reliable and uninterrupted communication even in challenging and complex environments.

Ultra-Low Latency: UWB technology boasts ultra-low latency, making it suitable for real-time applications, such as industrial control systems and time-critical data transmission.

Coexistence with Other Technologies: UWB devices can coexist with other wireless technologies without causing interference, making it compatible and versatile in mixed-use environments.

Future Potential: As research and development in UWB technology continues to advance, its potential for future innovations and applications remains promising, opening up new possibilities in various industries.

In summary, the versatility, low power consumption, secure communications, and ability to deliver high data rates make UWB technology a highly sought-after solution for short-range communications across a wide range of applications. The FCC has defined the highest signal strength ever recorded from UWB devices, setting the effective isotropic radiated power (EIRP) limit at -41.3 dB/MHz (as shown in Figure 2.5), which is lower than the noise level. This unique feature of UWB enables secure communications over short periods, making it a highly suitable technology for security applications and military communications [8]. Additionally, UWB possesses the valuable ability to address

multipath complexities by generating pulses for very short durations and distances (less than 23 cm for a 1.3 GHz band). This characteristic allows UWB to avoid overlapping and mitigates multipath fading, further enhancing its reliability [8].

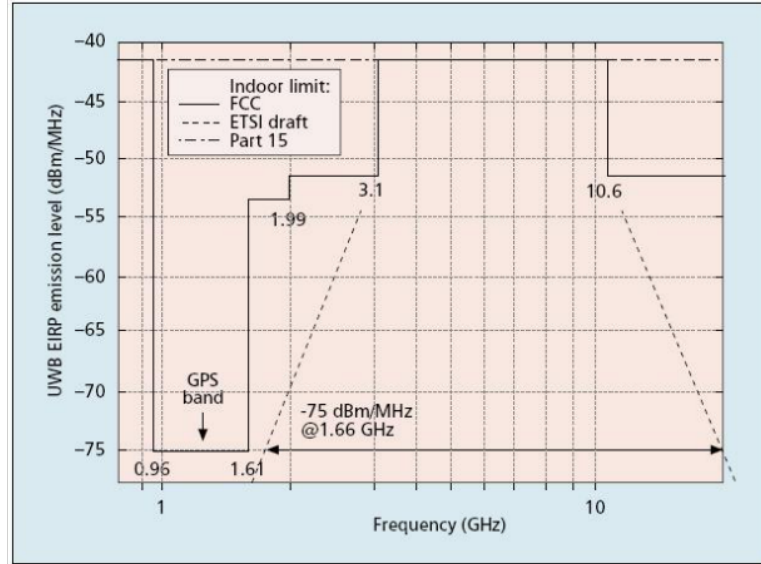


Figure 2.5: The Indoor Spectrum allocated by FCC [7, 8].

Furthermore, UWB utilizes non-ionizing radio pulses, resulting in negligible effects on the human body, making it a crucial asset in medical-related fields. The distinct features and differences of UWB from traditional communication systems have driven researchers to explore its potential applications and develop innovative communication systems. By capitalizing on the exceptionally large accessible bandwidth for short-range communication with data rates approaching gigabits per second, UWB communication systems have become increasingly feasible and efficient. UWB technology facilitates secure wireless communication links at low frequencies, enabling multiple devices to operate within the appropriate range. Moreover, UWB delivers outstanding data rate performance in multi-user network applications [9].

The foundational components comprising the UWB communication system are delineated in Figure 2.6, providing a detailed representation of its essential building blocks.

UWB technology's versatility extends to radar systems, where its short-duration pulses result in high resolution and precision. In radar applications, a single UWB antenna can replace a set of narrowband antennas, enhancing efficiency and enabling cost-effective high-definition radar systems, such as sensors, smart airbags, highway initiatives, and personal security sensors [9, 10]. Another prominent application of UWB technology lies

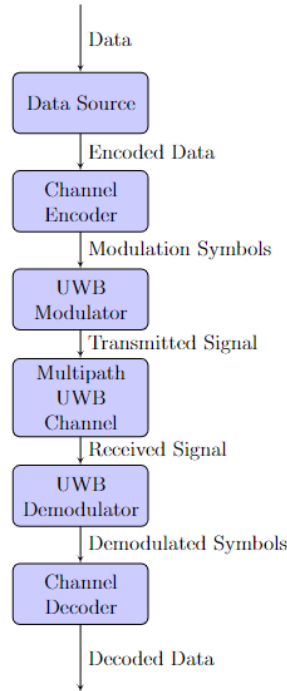


Figure 2.6: Detailed UWB Communication System Block Diagram [9].

in positioning systems (GPS), where its wide bandwidth contributes to signal resolution, enabling precise position determination within tens of meters [10]. UWB’s unique set of advantages positions it as a promising technology with vast potential for transformative applications across diverse industries.

2.3.1 UWB Medical Applications

UWB technology stands out for its uniqueness and numerous advantages, particularly in generating sub-nanosecond pulses below the noise level, rendering it highly suitable for various applications. These exceptional capabilities have piqued the interest of researchers, leading to extensive exploration of the technology’s potential applications. Over the last decade, numerous promising applications of UWB have been discovered, including several in the medical field. One significant medical application of UWB technology is medical monitoring, encompassing patient motion and vital signs monitoring. The high intensity of the generated UWB pulses makes it particularly useful for monitoring patient movements in critical care settings such as ICU and emergency rooms. Moreover, UWB can detect micro-movements inside the human body, enabling the monitoring of respiration and other vital signs with precision [11].

Medical imaging is another key area where UWB technology shines. It finds applica-

tions in cardiology, pneumology, and ear-nose-throat imaging, providing valuable insights for diagnosis and treatment [11]. Moreover, UWB's characteristics make it ideal for medical imaging purposes, such as breast lesion detection. Its ability to perform high-resolution fast data acquisition with short pulses over short distances facilitates precise localization of targets for microwave imaging based on differences in dielectric properties [12]. This feature is particularly valuable in diagnostic applications, where identifying and visualizing abnormalities accurately are critical for effective medical interventions. The versatility and unique features of UWB technology open a world of possibilities, and its application in the medical domain holds tremendous promise for improving healthcare outcomes and patient well-being. As research and development in UWB technology continues to advance, there is expected that even more innovative and transformative applications to emerge in the medical field and beyond.

2.4 Microwave Imaging

In recent years, medical imaging has become an indispensable and critical tool for diagnosing and treating various medical conditions. As a result, researchers have been diligently working on enhancing existing imaging technologies and developing innovative methodologies to improve medical imaging capabilities. Among these endeavours, the unique features of UWB technology have captured the attention of researchers, leading to the development of MWI methods for medical applications. UWB MWI offers a promising approach with several advantages, particularly in providing low-risk medical imaging of internal organs and tissues within the human body. By leveraging the contrast in dielectric properties, UWB enables safe and non-ionizing imaging, making it a health risk-free option for medical purposes. Notably, MWI has made significant strides in early breast cancer detection, demonstrating promising results [12, 13]. The fundamental setup of MWI imaging involves essential components, including UWB antennas (transmitter and receiver), the objects under investigation (human tissues and organs), and a vector network analyzer (VNA) to operate the antennas. The key focus in MWI lies in the dielectric properties, as the healthy and malignant tissues exhibit substantial dielectric contrast [13]. In essence, MWI technology distinguishes between healthy and malignant tissues based on their differences in dielectric properties. The setup is relatively

straightforward, requiring only transmitter and receiver antennas along with an image reconstruction algorithm to accurately localize the malignant tissues. UWB MWI holds great promise in revolutionizing medical imaging and diagnostic capabilities. Its ability to detect subtle differences in dielectric properties offers potential for early and accurate diagnosis of various medical conditions, including cancer. As researchers continue to refine and advance UWB MWI techniques, further breakthroughs and advancements in medical imaging can be anticipated, ultimately benefiting patient care and medical outcomes.

2.4.1 Dielectric Properties

MWI relies on dielectric properties as this technique differentiates healthy and malignant tissues based on the difference in their dielectric properties. MWI depends on high-frequency microwaves and the medium of propagation, which is determined by the absolute permittivity (ϵ_0) [14]. The dielectric properties comprise mainly two parameters: relative permittivity (ϵ_r) and conductivity (σ). Moreover, the absolute permittivity is also known as the permittivity of vacuum or free space and is represented as ϵ_0 with a value of 8.854×10^{-12} F/m (Farad/meter). The permittivity of the medium is represented as ϵ , and the relative permittivity ϵ_r is the ratio of the permittivity of the medium and the permittivity of free space.

$$\epsilon_r = \frac{\epsilon}{\epsilon_0} \quad (2.3)$$

The conductivity (σ) of any material is defined as the extent to which a material conducts electricity, with its measuring unit is S/m (Siemens per meter).

2.4.2 Microwave Tomography

Microwave tomography (MWT) is a powerful technique that utilizes the contrast in dielectric properties to detect and locate malignant tissues. MWT relies on the fact that malignant tissues typically exhibit higher permittivity and conductivity compared to healthy tissues [12]. When tissues with higher permittivity are exposed to UWB microwaves, more waves are reflected back to the source. By processing these waves, MWT can precisely locate the malignant tissues within the body. One of the significant advantages of MWT over conventional medical imaging methodologies is its non-contact nature. MWT does

not require physical or mechanical contact with the object under investigation, making it a safe and non-invasive imaging technique [14]. Additionally, MWT operates in the frequency domain, allowing for individual frequency measurements to avoid data loss and improve accuracy.

Moreover, MWT is robust and insensitive to environmental factors such as dust and water vapours. It can operate effectively even in high-temperature conditions, making it suitable for various real-world applications [14]. The use of microwaves in MWT ensures that the object under investigation remains unharmed during the imaging process, enabling high-frequency and accurate data transfers. Implementing MWT is relatively straightforward and safer compared to other imaging techniques, thanks to the simplicity of the hardware and the avoidance of major complexities [14]. These advantages make MWT a promising tool for various medical applications, including breast cancer detection, lung cancer diagnosis, brain stroke detection, and cardiac imaging [14]. As research in MWT continues to advance, its potential for revolutionizing medical imaging and diagnostics becomes increasingly evident.

2.4.3 Microwave Imaging Algorithms

The configuration of the MWI methodology necessitates an advanced imaging algorithm to process the experimental data and visualize the detected malignant tissues or tumours. Over the past decade, significant research has been conducted in the field of microwave imaging, resulting in the introduction and evolution of several imaging algorithms, particularly focused on breast lesion detection. Some of these notable microwave imaging algorithms include Delay and Sum (DAS), Delay Multiply and Sum (DMAS) or Confocal Imaging, Robust Capon Beamforming (RCB), and Channel-Ranked DAS (CR-DAS) [15].

Confocal Imaging/DMAS: The DMAS algorithm, also known as confocal imaging, is a time-domain technique based on the simple delay and sum method. While it is straightforward, this algorithm poses certain drawbacks and computational challenges. One of the major limitations lies in handling volumes with varying dielectric properties. Since UWB microwave imaging relies heavily on the contrast between normal and tumorous tissues' dielectric properties, accurate results require the ability to easily remove internal refractions, which is not possible using the DMAS algorithm [16].

MIST Beamforming: The MIST (Microwave Imaging via Space-Time) beamforming algorithm utilizes filters

to compensate for fractional time delays and dispersion. These filters are designed to pass signals originating from the inclusion location with unit amplitude and linear phase, while constraining the white noise gain, which helps improve clutter and scattering issues. However, this enhancement comes at the cost of increased computational complexity and burden [17]. Time Reversal: The time reversal technique is even more complex, as it relies on the concept that time-reversing the received scattered signals or spectrum at the receiver's end through the medium can achieve accurate contrast between the dielectric properties of materials at the source point. However, applying this technique requires a thorough examination and detailed information about the channel used, making it a challenging and time-consuming task [18]. While these algorithms have shown promise in microwave imaging, each comes with its own set of advantages and limitations (as presented in Figure 2.7). As researchers continue to explore and refine these methodologies, the field of microwave imaging for medical applications, particularly in detecting breast lesions and other medical conditions, is expected to witness significant advancements.

Technique	Description	Advantages	Limitations
DAS	Time-domain technique for breast lesion detection.	Straightforward implementation.	May lack accuracy, especially in handling volumes with varying dielectric properties.
DMAS	Time-domain technique based on delay and sum.	Simple but faces computational challenges.	Struggles with volumes having diverse dielectric properties; unable to remove internal refractions effectively.
RCB	Beamforming algorithm compensating for fractional time delays.	Improved clutter and scattering handling.	Introduces increased computational complexity.
CR-DAS	Variant of DAS incorporating channel ranking.	Enhanced accuracy achieved through channel ranking.	May still face challenges in accuracy.
MIST Beamforming	Utilizes filters to compensate for fractional time delays and dispersion.	Effective in improving clutter and scattering issues.	Enhancements come with increased computational complexity and burden.
Time Reversal	Complex technique relying on time-reversing received signals.	Achieves accurate contrast but requires detailed channel information.	Challenging and time-consuming application; demands thorough examination of the channel used.

Figure 2.7: Microwave Imaging Techniques Comparative Analysis.

2.5 Introduction to Cancer

Cancer is a devastating disease that arises from genetic changes disrupting the orderly process of cell growth and replacement in the human body. Cells continuously divide and replace old or damaged cells with new ones, but when genetic alterations occur, cells can grow uncontrollably, leading to the formation of tumours. According to the American Society of Clinical Oncology (ASCO), cancer is characterized by the uncontrolled growth and spread of abnormal cells, and in some cases, these rapidly dividing cells can form tumours, which can be life-threatening [19].

Globally, cancer is a leading cause of death, with approximately 10 million cancer-related deaths reported worldwide in 2020, according to the UK cancer research department. Among the most common causes of cancer-related deaths are lung, liver, and stomach cancers. The mortality rate in the UK is lower than two-thirds of Europe but higher than two-thirds of the world. Over the years, nearly 200 different types of cancer have been identified, which can be categorized as follows [20]:

- **Carcinoma:** This type of cancer originates in the skin or the tissues lining the internal organs. Carcinomas include breast cancer, lung cancer, prostate cancer, and colorectal cancer. Carcinoma is the most prevalent type, affecting approximately 85 out of every 100 cancer patients in the UK (85%) [21].
- **Sarcoma:** Sarcomas arise in the connective tissues of the body, such as muscles, fat, bone, blood vessels, cartilage, tendons, and fibrous tissues.
- **Leukaemia:** Leukaemia is a cancer of the white blood cells and affects tissues involved in blood cell production, such as bone marrow. It is caused by the rapid growth of abnormal cells in the blood, which disrupts the proper functioning of blood cells.
- **Myeloma:** Myeloma impacts the cells and tissues of the immune system, particularly plasma cells, affecting the production of antibodies essential for fighting infections.
- **Brain and Spinal Cord Cancers:** These cancers are known as central nervous system cancers and involve tumours forming in the brain or spinal cord.

While there are nearly 200 types of cancer, not all of them cause significant human casualties. Among the most common and deadly types are lung, liver, stomach, breast,

prostate, and colorectal cancers. These types of cancers remain prominent due to their high mortality rates and the number of cases reported globally.

2.5.1 Breast Cancer

Breast cancer has emerged as one of the most prevalent types of cancer in recent years, witnessing a significant rise in the number of patients globally, including the UK. This form of cancer predominantly affects women, making it the second most common cancer overall. Breast cancer occurs when normal breast tissues or cells undergo abnormal and uncontrolled growth, leading to the formation of a tumor that can spread to other parts of the body, causing severe damage. According to the World Health Organization (WHO) report, breast cancer affects around 2.1 million women each year and results in the deaths of approximately 627,000 women annually [21, 22]. Various methods are used to detect breast cancer, employing different techniques:

- **Clinical Examination:** Clinical breast cancer examination involves a physical examination of both breasts, along with a thorough inquiry about symptoms and family medical history, to arrive at a diagnosis.
- **Mammograms:** Mammography is a common detection method that utilizes X-ray imaging of the breast from different angles. Radiographers then analyze these images to identify the presence of tumours.
- **Magnetic Resonance Imaging (MRI):** MRI utilizes magnetic fields to generate images of the interior of the body. Experts analyze these images to detect the presence of cancer.
- **Biopsy:** This approach involves the microscopic analysis of a tissue sample by a pathologist to determine the presence of tumours and devise an appropriate treatment plan [23].

Early detection of breast cancer is crucial for successful treatment and increased survival rates. Regular screening and awareness about the risk factors can significantly contribute to early diagnosis and better outcomes for breast cancer patients.

2.5.2 Lung Cancer

Lung cancer ranks among the most prevalent categories of cancer, accounting for approximately 12.3% of all cancer cases. While several factors can contribute to the development of lung cancer, smoking is recognized as a major risk factor. Research indicates that nearly 80-90% of lung cancer patients are smokers or have a history of using tobacco-related products [24]. The disease originates in the trachea, lung tissues, or the main airway. According to Cancer Research UK, primary lung cancer can be classified into two categories:

- Small Cell Lung Cancer (SCLC): This aggressive type of lung cancer is less common, accounting for about 15% of lung cancer cases. It tends to spread quickly and is often associated with heavy smoking.
- Non-Small Cell Lung Cancer (NSCLC): This is the most common type of lung cancer, making up about 85% of cases. NSCLC can be further divided into subtypes such as adenocarcinoma, squamous cell carcinoma, and large cell carcinoma.

Small cell lung cancer is localized only in the lung and affects a small area of tissues. On the other hand, non-small cell lung cancer is an advanced stage of cancer that has spread to surrounding tissues or other parts of the body [20]. Studies suggest that lung cancer is more commonly diagnosed in individuals over the age of 50. Besides smoking, there are other risk factors that may contribute to the development of lung cancer, including exposure to radon gas, certain workplace chemicals, family history of cancer, and certain cancer treatments used for other types of cancer [20]. Early detection of lung cancer is critical for successful treatment and improved outcomes. Conventional treatments for lung cancer include radiotherapy, chemotherapy, chemoradiotherapy, and immunotherapy [20]. By detecting lung cancer at an early stage and implementing appropriate treatment methods, there is a higher chance of successful management and recovery.

2.5.3 Brain Tumour

A brain tumour occurs when there is an abnormal and uncontrolled growth of brain tissues or a cluster of brain cells. The human body is composed of billions of cells, and in a healthy state, new cells replace old and dead cells in an organized manner.

However, in the case of a brain tumour, this natural process gets disrupted, leading to the uncontrolled growth of cells and the formation of a tumour [20]. Brain tumours can be broadly classified into approximately 100 types, some of which are cancerous (malignant) and others non-cancerous (benign) [20].

Benign brain tumors are non-cancerous growths characterized by homogenous structures. Unlike malignant tumours, benign brain tumors are less likely to reoccur after successful treatment. These tumours can usually be easily localized and identified through radiology, and treatment options may include medications or, in some cases, surgeries [25]. On the other hand, malignant brain tumours are cancerous growths with heterogeneous structures that consist of cancerous cells or tissues. Malignant brain tumours are life-threatening and require immediate and aggressive treatment [26]. Early detection of brain tumors is critical for successful recovery and treatment. Medical imaging devices such as MRI (Magnetic Resonance Imaging) play a crucial role in the detection of brain tumours. MRI produces detailed images of the brain, allowing medical professionals to visualize the tumour and determine its location and characteristics [20]. The most common treatment for brain tumours is radiotherapy, which involves the use of high-energy conventional, ionized X-rays to destroy tumour cells [20]. Chemotherapy is another treatment option where doctors use anticancer drugs to target and destroy cancer cells. Chemotherapy is often prescribed to patients after radiotherapy or surgery to eliminate any remaining cancer cells [20].

In some cases, using conventional imaging techniques like MRI may not provide enough information to determine the exact type of tumour. In such situations, doctors may need to perform additional tests and examinations to make an accurate diagnosis [20]. While treatments for brain tumours can be effective, they can also be painful, especially in the case of malignant tumors. Early detection and diagnosis are crucial in minimizing pain and improving the chances of successful treatment and recovery. Regular medical check-ups and early intervention can significantly improve the outcomes for individuals affected by brain tumours.

2.6 Evolution of Microwave Imaging for Lesion Detection

2.6.1 Breast Cancer Detection via MWI

Breast cancer is a significant cause of mortality, particularly among females, emphasizing the importance of early detection for successful treatment. Over the past few decades, microwaves and UWB technology have gained popularity in biomedical applications, with UWB microwave imaging becoming a promising tool for early-stage cancer detection. MWI utilizes microwaves for a short duration at a very high frequency range, employing non-ionized rays, making it a safe option for health risk-free imaging. In 2010, a UWB microwave imaging methodology was introduced in [26], employing a circular array of antennas to localize small targets within cylindrically shaped objects. The study investigated the ability of MWI to detect dielectric contrasts between the material used in fabrication and breast fat tissues. The researchers fabricated a homogenous cylindrical object and a target with dielectric contrast, like breast tissue characteristics. By reconstructing the signals through an imaging algorithm, the researchers were able to successfully detect the target, demonstrating the potential of UWB microwave imaging for cancer detection.

Another microwave breast imaging prototype was presented in 2013 [27], based on tissue sensing adaptive radar (TSAR) using a monostatic UWB antenna. This prototype aimed to improve the imaging speed and sensitivity of breast tumour detection. The methodology was tested on eight patients, and the reconstructed images closely resembled clinical results with a sensitivity of -80dB. However, this prototype required relatively longer measurement times, which was a limitation to its practical implementation.

In 2016, a new microwave imaging algorithm was developed to detect breast cancer in heterogeneous breasts [28]. The CMOS chip-based time-domain MWI setup provided fast measurements and generated reconstructed images with reliable detection capabilities. The researchers explored the potential of MWI for differentiating healthy and malignant tissues in breasts with varying composition, which is more representative of real-world scenarios. The results showed promise in distinguishing healthy and cancerous tissues based on dielectric contrasts, thereby highlighting the potential of MWI for breast cancer detection.

Furthermore, in 2019, a portable breast tumour detection via microwave imaging was

presented in [29]. This methodology utilized an array of UWB antennas controlled by a microcontroller to capture dielectric contrast between healthy and malignant tissues. The portable nature of this setup made it suitable for on-the-go imaging and demonstrated the potential for MWI to be used as a point-of-care diagnostic tool for breast cancer screening.

In collaboration with researchers at London South Bank University, UBT introduced a novel and fast microwave imaging prototype for breast cancer detection in 2019 [30]. Named MammoWave, this prototype employed UWB microwaves based on the Huygens principle to differentiate healthy and malignant tissues using differences in dielectric properties. The technology showed promising results in accurately detecting breast cancer and demonstrated the potential to revolutionize breast cancer screening and diagnosis.

The advancements in UWB microwave imaging for breast cancer detection are promising and offer potential for early and accurate diagnosis, enhancing the chances of successful treatment and improved patient outcomes. The non-invasive nature of MWI, combined with its ability to provide high-resolution images and distinguish healthy and malignant tissues based on dielectric properties, makes it an attractive candidate for breast cancer screening. With further research and development, MWI could become a standard tool in breast cancer screening and diagnosis, revolutionizing cancer detection and patient care. As technology continues to advance, UWB microwave imaging holds the potential to transform the field of medical imaging, providing safer and more efficient diagnostic options for a wide range of medical conditions.

2.6.2 Lung Lesion Detection via MWI

Lung cancer may not be as commonly discussed as breast cancer, but its prevalence and mortality rate are significant, ranking second in cancer cases worldwide. Unfortunately, screening for lung cancer is not as common as it is for breast cancer, often only occurring in the advanced stages of the disease. However, researchers have been exploring the potential of MWI for early-stage lung cancer detection, inspired by the success of MWI in breast cancer detection. In 2014, a study utilized a multi-layered lung phantom with dielectric properties similar to those of the lung [31]. The experimental setup in this study was simulation-based, where a realistic model was prepared with specific parameters. The researchers considered a tumour size of 10mm and placed the antennas at 10mm from the

model. The results demonstrated the successful detection of millimetre-sized tumours [31].

In 2015, researchers presented a frequency-domain MWI algorithm for lung cancer detection [32]. This algorithm measured the scattered field outside an artificially fabricated lung phantom with varying dielectric properties to detect the dielectric contrast inside the phantom. UWB microwaves were employed, and the Bessel function was used to forward propagate the field, providing crucial information on dielectric contrast. The results showed promise in detecting lung tumours using this method [32].

Building upon these promising studies, a researcher from Najran University in Saudi Arabia performed a simulation-based experiment using UWB microwaves to detect lung tumours in 2018 [33]. The simulation results indicated successful detection of lung tumours as small as 4mm, highlighting the potential of MWI for early-stage lung cancer detection [33].

In 2021, researchers from London South Bank University and UBT introduced a novel methodology to detect lung infection caused by the coronavirus using microwave imaging [34]. For this purpose, a multi-layered phantom with realistic dielectric properties and dimensions was fabricated, and measurements were performed using one transmitter and one receiver UWB antenna. This methodology proved quite successful in generating results with detected tumors, further demonstrating the capabilities of MWI for lung cancer detection [34].

As more researchers continue to explore and refine MWI algorithms and methodologies, lung cancer screening and detection may become more accessible and efficient, ultimately improving patient outcomes, and reducing the burden of this devastating illness.

2.6.3 Brain Lesion/Stroke Detection via MWI

Another crucial medical application of MWI technology is in brain tumour and stroke detection. The shape of the human head bears a resemblance to that of the breast, leading researchers to explore the potential of MWI for brain cancer and stroke detection. Brain cancer occurs due to the uncontrolled and abnormal growth of cells in the brain, while brain strokes result from blocked/burst veins, vessels, or ducts in the brain. Head, skull, and brain injuries are common in accidents worldwide, further emphasizing the need for a rapid and efficient method for brain cancer and stroke detection using microwave imaging.

In 2012, researchers from The University of Edinburgh, UK, proposed a new methodology for brain cancer detection utilizing UWB Vivaldi antennas and MWI [35]. They designed a cancerous brain model using CST Microwave Studio. The microwaves were introduced to the phantom from the transmitter antenna on one side and received by the receiver antenna on the other end. Noise and reflections were effectively removed using an analytical approach [35]. The images generated from the microwave imaging algorithm successfully detected the cancer in the model.

In 2016, researchers from India investigated microwave imaging techniques with modified antennas for brain cancer detection [36]. They used antennas in the range of 6 GHz to 10 GHz, including rectangular microstrip patch antennas and ground plane antennas. A brain model with varying realistic dielectric properties, including a tumour, was prepared using CST. The results obtained from processing the data via the microwave imaging algorithm showed promising tumour detection with potential for further improvement in the future [36].

Furthermore, in 2020, a novel approach for brain stroke detection using microwave imaging was introduced [37]. The researchers fabricated a realistic phantom with multiple layers to mimic different brain tissue layers, including a fabricated tumour for stroke detection. Measurements were performed inside an anechoic chamber at London South Bank University using two micro-strip UWB antennas. The measurement data was then processed through an imaging algorithm. The reconstructed images confirmed the detection of the fabricated inclusion, followed by image quantification with artefact removal [37].

As researchers continue to refine and enhance MWI algorithms and prototypes, it holds immense potential to revolutionize brain cancer and stroke diagnosis, enabling earlier detection and more effective treatment strategies, ultimately improving patient outcomes and quality of life.

2.7 Research Gap and Proposed Research

Over the last decade, MWI has shown remarkable promise as a candidate to revolutionize medical imaging. Research indicates that MWI has the potential to significantly impact medical diagnostic applications, particularly in the detection of breast cancer. One of the most significant advantages of MWI is its ability to provide health risk-free medical

imaging, as it uses non-ionized rays and usually avoids any physical contact with the patient. Researchers have demonstrated that MWI is a cost-effective, easy-to-assemble, and reliable technology for medical imaging, with much of the focus on early-stage disease detection.

Several MWI prototypes are currently undergoing clinical trials, further fuelling the interest of scientists and researchers to explore ways to make this methodology even more efficient. While most experiments in the last decade were performed on phantoms, which are simplified models of human tissues, there is a need to move towards more realistic parameters and complex structures to ensure the effectiveness of MWI in real-world scenarios. MWI has demonstrated potential in detecting cancer in the breast, brain, and skin. However, lung cancer detection using MWI remains challenging due to the larger geometric shape of the lungs compared to the breast or brain. Additionally, most methodologies presented in the last decade focused on locating cancerous tissues in an early stage and generated results in 2D. There has been limited emphasis on measuring the dimensions and size of the detected tumours.

Hence, the proposed research aims to validate the capability of MWI in detecting lung tumors by fabricating various phantoms with realistic parameters and dielectric properties of lung tissues and tumors. The focus of the research is to explore 3D microwave imaging to detect tumors in early stages. Experiments are conducted on different phantoms with symmetrical and asymmetrical shapes, incorporating 3D structured tumors. Moreover, the research aims to analyze the dimensions of the detected tumors in the reconstructed images via MWI and conduct a detailed analysis of image quantification factors.

This proposed research represents a critical analysis of the 3D microwave imaging methodology and explores various approaches to reduce the detection time. By advancing MWI capabilities in detecting lung tumours and providing accurate size information, this research could significantly improve early-stage diagnosis and treatment outcomes for patients with lung cancer. The potential impact of this research extends to other medical imaging applications, positioning MWI as a transformative technology in the field of healthcare.

2.8 Summary

This chapter extensively discussed the current landscape of conventional medical imaging technologies dominating the field of medical diagnostics, including X-ray-based computed tomography, ultrasounds, and MRI. Despite continuous refinements to improve their efficiency and reliability, these modalities come with inherent drawbacks that limit their widespread applicability. One significant limitation is the high cost associated with conventional imaging technologies, which can hinder access to advanced diagnostic tools, particularly in resource-limited healthcare settings. Moreover, the large and cumbersome equipment requires considerable effort and workforce to transport and install, making it challenging for deployment in remote or underserved areas. Additionally, these technologies are typically confined to hospitals, and the expertise of the operator can influence the quality and accuracy of the results. A major concern with conventional imaging methods is their reliance on ionizing radiation, which poses potential risks to patients. Although efforts have been made to minimize radiation exposure, the use of ionizing rays remains a cause for caution, especially in repeated imaging studies. Contrastingly, this chapter introduced a new frontier in medical imaging with the utilization of microwave imaging through UWB technology. MWI has shown immense promise in medical diagnostics, particularly for early cancer detection. Notably, MWI offers a wealth of advantages, such as non-ionizing signals, rendering it a safer alternative to traditional ionizing radiation-based techniques. Moreover, MWI is cost-effective, easy to implement, and does not require direct physical contact with the subject under examination.

The chapter delved into the history of UWB fundamentals and the evolution of MWI algorithms over the last decade. Various methodologies and prototypes have been discussed, demonstrating the successful application of MWI in detecting breast, lung, and brain cancers. Despite the promising results, certain MWI algorithms, such as DMAS, time reversal, and confocal imaging, exhibit computational and cost-related limitations. Addressing these challenges is crucial for wider adoption of MWI in clinical settings. Furthermore, the chapter highlighted the critical importance of cancer detection, providing insights into different cancer types and their impact on mortality rates and cases. Early detection emerges as a key factor in improving patient outcomes and survival rates. However, there remain research gaps and challenges, particularly in applying MWI to lung cancer detection, owing to the complexities of lung geometry.

Chapter 3

Initial Technical Approach for MWI

3.1 Introduction

The proposed research aims to develop a fast and novel methodology for MWI using realistic lung phantoms with accurate dielectric properties. The primary objective is to validate the capability of MWI for lung cancer and lesion detection. The chapter outlines the basic methodology of MWI and the required hardware for the experimental setup. It also introduces the proposed imaging algorithm that will be used for both phantoms. The research focuses on two different realistic lung phantoms with varying dielectric properties. The first phantom was designed to simulate the detection of COVID-19 infections inside the lung, taking into account the global pandemic. The second phantom represented a more comprehensive and realistic model of the lung, aiming to mimic actual lung tissues and tumours accurately.

Both phantoms are crucial in ensuring the validity and applicability of the research findings. The chapter emphasizes that the imaging algorithm and basic methodology remain the same for both scenarios, with only the hardware configuration varying between the two experimental setups. In conclusion, this chapter sets the groundwork for the proposed research, emphasizing the importance of realistic lung phantoms and the potential applications of MWI in lung cancer and lesion detection. The use of accurate dielectric properties in the phantoms enhances the credibility of the research findings. The chapter also highlights the significance of exploring different experimental setups to assess the effectiveness of MWI in various lung imaging scenarios. Ultimately, the goal has been to contribute to the advancement of medical imaging techniques, leading to improved early

detection and treatment of lung conditions, including cancer and COVID-19 infections.

3.2 Experimental Setup

In the investigation of MWI capability for lung lesion/cancer detection, an anechoic chamber at London South Bank University (LSBU) has been utilized. The essential hardware required for MWI includes antennas, a VNA, and an image-processing algorithm. For this research, two types of antennas were employed for both scenarios: one for transmitting and one for receiving. These antennas operated in UWB frequency range, were vertically polarized, and had omnidirectional characteristics in the azimuth plane. To record the transfer function (S_{21}) at different frequency ranges, the antennas were connected to a 2-port VNA. The VNA was responsible for capturing the transmitted and received signals during the measurements. Additionally, a rotating stand and table were incorporated into the experimental setup. These mechanical components were controlled by a Graphical User Interface (GUI) programmed in Python, allowing precise rotation of the antennas and data recording at 6° intervals over a complete 360° rotation. The combination of these hardware components allowed for the comprehensive and accurate detection of lung lesions/cancer using MWI. During each set of measurements, the transmitting antenna was attached to the rotating table/stand, and the receiving antenna collected signals at regular intervals as it rotated around the transmitting antenna. This rotation allowed for a comprehensive sampling of the scattering information from different angles, enhancing the quality and accuracy of the MWI data.

3.2.1 UWB PulsON P200

The choice of antennas is of utmost importance in MWT and radar-based techniques, as they are responsible for transmitting and receiving the UWB signals. UWB antennas offer the advantage of serving as both transmitters and receivers, depending on the selected configuration. The transmitter antenna emits signals towards the object under investigation, and the receiver antenna receives the complex signals at the receiver's end. Hence, selecting the appropriate UWB antenna is critical to ensure better penetration and accurate measurements in MWI. For this research, the PulsON p200 UWB broad-spectrum antenna (shown in Figure 3.1) was utilized.



Figure 3.1: The PulsON P200 UWB Antenna [38].

This vertically polarized antenna emits radiations omnidirectionally in the azimuth plane, and it exhibits a return loss of approximately -14 dB or better, depending on the experimental setup’s precision [38]. An essential feature of this antenna is its high radiation efficiency, which is approximately 90% as in [39]. The functionality of the antenna is determined by coupling it with either the transmitter or the receiver port of the VNA. Furthermore, the gain of the antenna is a crucial factor in the performance of MWI, and the PulsON p200 antenna offers a gain of approximately 3 dB [38]. The choice of this particular antenna was also driven by its availability, cost-effectiveness, and its high-frequency range of 1-10 GHz, which aligns well with the requirements of MWI measurements. The antenna’s properties, such as its high radiation efficiency, gain, and broad frequency range, made it a suitable candidate for this research, ensuring that the MWI system can effectively transmit and receive UWB signals for detecting lung lesions or cancerous tissues. Table 3.1 provides an overview of the antenna patterns and parameters.

Table 3.1: Characterisation of PulsON P200 [38].

Characteristic	Specification
Pattern	Omni in azimuth to ± 15 dB
Polarisation	Linear (vertical)
Matching	VSWR 1.5:1; $ S_{11} $ -14 dB
Gain	Nominally 3 dBi
Phase Response	Linear
Efficiency	Nominally $> 90\%$

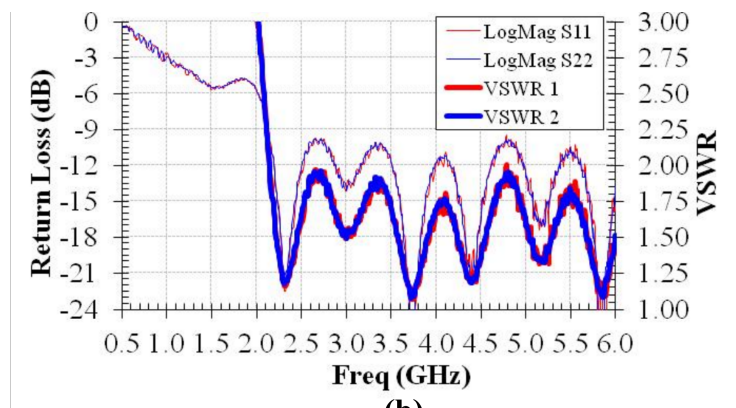
3.2.2 Planner UWB Horn Antenna

During this research, another UWB antenna used was the UWB planner horn antenna (shown in Fig. 3.2(a)). The design of this antenna was motivated by the need to provide increasing gain with an extended frequency range, making it well-suited for impulse responses and UWB applications. The antenna's operable range is from 2 to 10 GHz, and it can be further boosted for the 3-6 GHz range. The UWB planner horn antenna offers a gain of +6 dB at 3 GHz and +9 dB at 6 GHz, demonstrating excellent performance over a wide frequency range (as can be observed from Fig. 3.2 (b)). These values are obtained based on measured data and the study of the antenna's performance, which is presented in reference [40].

The high gain of this antenna at various frequencies makes it an ideal choice for MWI measurements, as it enhances the sensitivity and accuracy of the detection process. The increasing gain with the frequency range allows for better penetration and detection of signals, making it suitable for capturing detailed information about the internal structure of the object under investigation. Additionally, the wide frequency range of the UWB planner horn antenna aligns well with the UWB signals used in MWI, ensuring that it can effectively transmit and receive signals for detecting lung lesions or cancerous tissues. The combination of both antennas provides the necessary versatility and performance needed to capture microwave signals and generate high-quality images for diagnosing lung lesions or cancer at an early stage accurately and efficiently.



(a)



(b)

Figure 3.2: (a) The Planner UWB Horn Antenna, (b) Antenna Pattern [40].

3.2.3 Vector Network Analyser

The VNA is a crucial instrument for UWB microwave imaging in the frequency domain, as it enables the use of step frequency methodology to perform measurements over a wide frequency range. The VNA plays a central role in MWI as it measures the transmitted signal from the component attached to the VNA and records the received signal, providing essential information such as phase and amplitude data. For the detection of lung COVID-19 infection, a two-port VNA model MS2028C from Anritsu (manufactured by Anritsu EMEA Ltd) was utilized. This VNA has an operating frequency range of 5 MHz to 20 GHz, making it suitable for performing MWI measurements (as shown in Fig. 3.3). The transmitter and receiver antennas are connected to port 1 and port 2 of the VNA, respectively. In each recorded measurement, the transmitter antenna emits UWB radiations through the phantom under investigation, and the receiver antenna captures the complex scattered parameters of the received signals. This process is facilitated by the VNA, which plays a vital role in gathering the necessary data for microwave imaging.

The VNA's ability to measure complex scattered parameters, including both phase and amplitude information, is essential for accurate and reliable MWI. This data provides crucial insights into the behaviour of the microwave signals as they interact with the lung phantom, allowing for the reconstruction of high-quality images. The VNA's wide frequency range further enhances its capabilities, enabling MWI measurements to be performed over a broad spectrum of frequencies, which is advantageous for detecting lung lesions or COVID-19 infections at different frequency bands.

In microwave imaging, the scattered parameters calculated by the VNA are complex numbers that represent the characteristics of the transmitted signal and the refraction in the frequency domain. These parameters are presented in the form of a matrix of complex numbers with real and imaginary parts. The matrix is denoted by S_{ij} , where "i" represents the port from which the signal is transmitted, and "j" represents the port at which the signal is received. In the two-port VNA used in this research, the transmitting signal from port 1 is known as the forward signal, and the signal received in terms of scattered parameters is known as the reverse measurement. The four types of scattered parameters commonly used are as follows: In the investigation of microwave imaging (MWI), several scattering parameters are crucial for characterizing the behavior of the antenna system. These parameters provide valuable insights into the interactions of ultra-wideband (UWB)



Figure 3.3: The Vector Network Analyser, MS2028C Anritsu.

signals with the investigated object. The following are the key scattering parameters used in this research:

- **S11:** This parameter measures the signal transmitted from port 1 and received as the reflected signal back at port 1. It determines the power reflected from the antenna, providing information about the reflection coefficient.
- **S12:** In this parameter, the signal is transmitted from port 2 and received at port 1. The transmitter antenna is attached to port 2, and the receiver antenna is attached to port 1. This parameter helps in studying the transmission characteristics of the antenna system.
- **S21:** This parameter measures the signal transmitted from port 1 (as the transmitter) and received at port 2 (as the receiver). It is a crucial parameter for MWI, as it characterizes the transmission and scattering of the UWB signals through the phantom or object under investigation.
- **S22:** This parameter measures the signal transmitted from port 2 and the reflected signal received at port 2. It is useful in analyzing the reflection and scattering properties of the antenna system.

In this research, the **S21** parameter has been recorded and processed for microwave imaging. This choice of scattered parameter is determined by the measurement setup and the specific methodology used for MWI. By analyzing the **S21** data, researchers can gain valuable insights into the interactions between the UWB signals.

3.2.4 Rotating Stand and Table

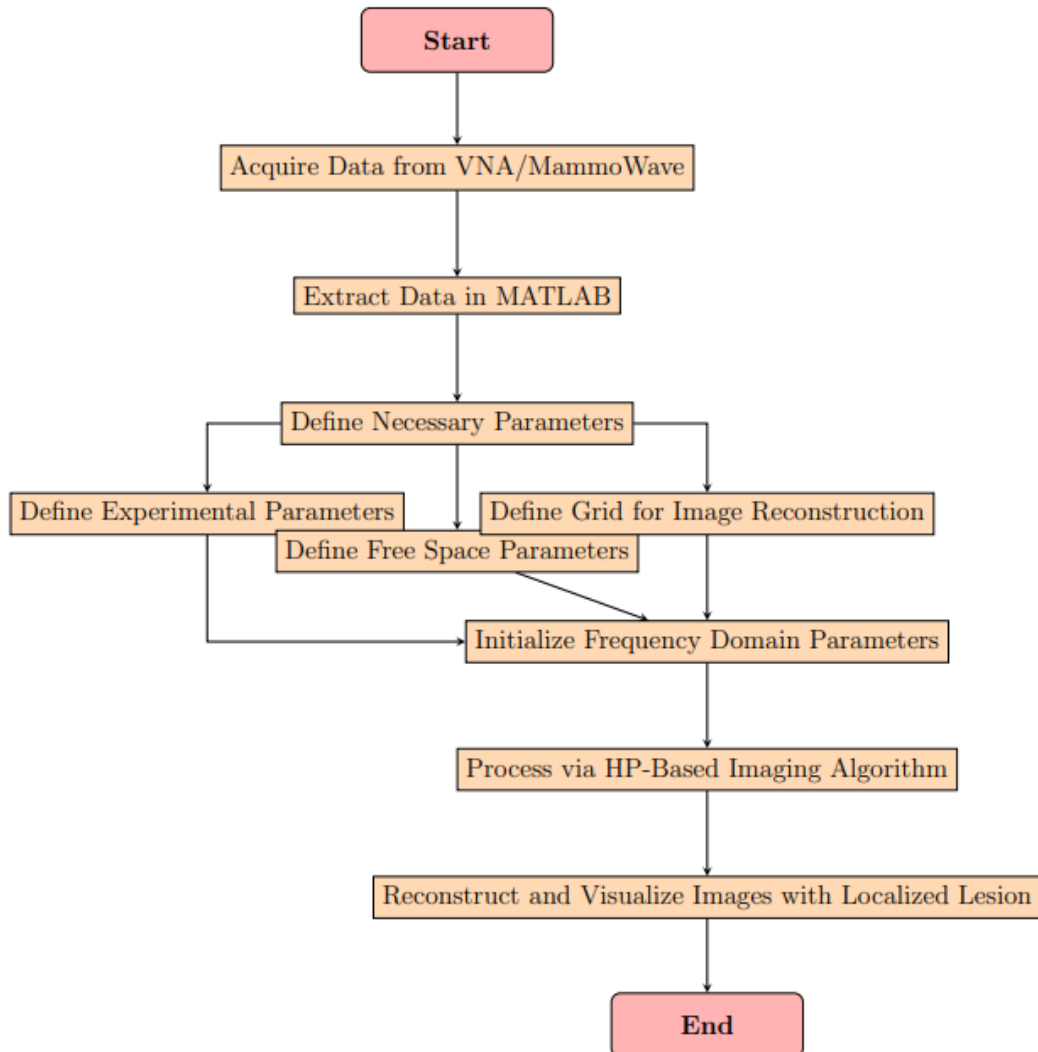
To perform microwave imaging experiments, a rotating stand and rotating table are essential components of the setup. However, due to the requirement of taking measurements at intervals of every 6° from 0° to 360° , manually rotating the phantom for each measurement would be impractical and could potentially introduce errors in the results. To overcome this challenge, the proposed experiments utilize both a rotating stand and a rotating table, each serving a specific purpose. The rotating stand is used for smaller phantoms, while the rotating table is employed for larger phantoms. Both the rotating stand and table are equipped with motors that can be controlled by a modulator running on a GUI designed in python.

The experimental procedure involves placing the fabricated phantom on the rotating table or stand, depending on its size. The GUI then controls the motors, which rotate the phantom at precise intervals of every 6° . During the rotation, measurements are recorded and saved using the VNA, capturing the complex scattered parameters for each orientation of the phantom.

3.3 Huygens Principle Based MWI Algorithm

The fundamental methodology behind MWI is to detect the contrast in dielectric properties between healthy and malignant tissues. UWB technology has gained attention in medical applications due to its ability to generate short-duration pulses over a wide spectrum at high frequencies, making it accurate, reliable, and cost-effective for medical imaging. In MWI, the challenge is to localize and differentiate malignant tissues using an imaging algorithm that reconstructs images based on the dielectric properties of the tissues. The proposed microwave-imaging algorithm in this research is based on the Huygens principle, a physical optics principle. According to the HP, each wave excites local matter, which reradiates secondary wavelets. The superposition of all these wavelets

results in a new wave, representing the envelope of all the individual wavelets [41]. The proposed methodology based on the HP operates in the frequency domain, allowing for gathering information from individual frequencies to generate a coherent image with the dielectric contrast. Although HP does not calculate the exact dielectric contrast, it captures enough information to differentiate between healthy and malignant tissues [42]. The basic methodology of HP-based MWI is shown in the block diagram below.



UWB microwave imaging can be classified into two aspects: UWB tomography and radar-based techniques. Within radar-based methods, the HP-based algorithm offers the ability to differentiate between healthy and malignant tissues in the frequency domain, as initially introduced in [41]. The proposed approach utilizes the HP to transmit waves in the forward direction, eliminating the need for resolving inverse scattering problems, matrix inversion, or generation. By utilizing the HP-based algorithm in UWB microwave

imaging, this research aims to effectively detect lung cancer/lesions using phantoms with realistic dielectric properties. The frequency-domain approach of the proposed methodology ensures the collection of sufficient data to generate accurate images with the potential to differentiate between healthy and cancerous lung tissues.

In order to understand the HP-based MWI algorithm mathematically, consider a cylinder with the known dielectric properties such as dielectric constant ϵ_{r1} and conductivity σ_1 in free space with the radius a_0 . The transmitting source enlightening the cylinder in the free space can be presented as tx_m operating at the frequency f . As the main aim is to differentiate different materials based on the difference in their dielectric properties, assume that there is one more small cylinder inside the cylinder with known dielectric properties but the dielectric constant ϵ_r of the inner cylinder is higher than the outer one (see in Fig. 3.4).

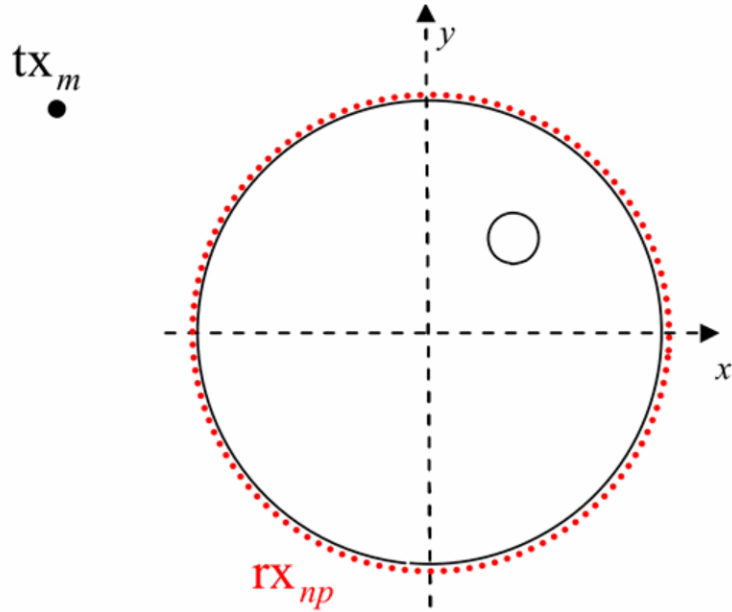


Figure 3.4: The pictorial view, where red dots show receiving points and black dot transmitting position.

As the same methodology is used for the proposed research, the main idea is that the transmitting position is fixed with the phantom and the Rx antenna records measurements with every 6° interval, and those receiving points can be presented as rx_{np} . Suppose that the electric field at the receiving points $rx_{np} \equiv (a_0, \phi_{np}) \equiv (\vec{\rho}_{np})$ (with $\vec{\rho}_{np}$ is presenting the observation point [41–43]) is known and can be presented as:

$$\mathbf{E}_{i\mathbf{t}\mathbf{x}_m}^{\text{known}}|_{\mathbf{r}\mathbf{x}_{np}} = \mathbf{E}_{i\mathbf{n}\mathbf{p},\mathbf{t}\mathbf{x}_m}^{\text{known}} \quad \text{with } np = 1, \dots, N_{pt} \quad (3.1)$$

Now, employing the basics of Huygens' Principle (HP) on the current scenario and re-declaring HP employing $\mathbf{E}_i(\mathbf{n}\mathbf{p},\mathbf{t}\mathbf{x}_m)^{\text{known}}$ as the locus of the wave with the information of the previous waves in the wavefront. The field inside the cylinder can be calculated for the N_{PT} number of observing points as the superposition of the field radiated as:

$$\mathbf{E}_{\text{HP}}^{\text{rcstr}}(\rho, \phi; \mathbf{t}\mathbf{x}_m; f) = \Delta s \sum_{n=1}^{N_{PT}} \mathbf{E}_{i\mathbf{n}\mathbf{p},\mathbf{t}\mathbf{x}_m}^{\text{known}} G(k_1|\vec{\rho}_{np} - \vec{\rho}|) \quad (3.2)$$

where in Eq. (3.2) k_1 represents the wave number and as the measurements have been performed in free space so the wave number has been kept as free space dielectric constant which is 1, Δs is the distance between two adjacent receiving points and is known as the spatial sampling [41, 42]. $\mathbf{E}_{\text{HP}}^{\text{rcstr}}(\rho, \phi; \mathbf{t}\mathbf{x}_m; f)$ is considered as the reconstructed field denoted by 'rcstr', and HP implies the implication of Huygens' principle to reconstruct the field. It has been assumed that this field carries the information of dielectric property differences inside the cylinder, not accurately but the dielectric contrast map, which has been shown in [41–43]. Green's function G , as implemented, has been used to forward propagate the field and can be represented as:

$$G(k_1|\vec{\rho}_{np} - \vec{\rho}|) = \frac{1}{4\pi|\vec{\rho}_{np} - \vec{\rho}|} e^{-jk_1|\vec{\rho}_{np} - \vec{\rho}|} \quad (3.3)$$

Furthermore, the Green's function implies a singularity for $|\vec{\rho}_{np} - \vec{\rho}| = 0$; however, this singularity may be canceled by multiplying the Green's function by $|\vec{\rho}_{np} - \vec{\rho}|$ as pointed out in [41]. HP does not calculate the exact internal field with all the information of the dielectric contrast even for homogenous media. However, as MWI differentiates between healthy and malignant tissues based on the difference in the dielectric properties the main goal is to locate the tumour by gathering the information of dielectric contrast by HP.

For further investigation, assume that the outer cylinder is exposed to transmitting radiations with various numbers of frequencies N_F with the frequencies f_i . The intensity I of the reconstructed image can be obtained by summing the field calculated at all frequencies and can be represented as:

$$I_{\text{HP}}(\rho, \phi; \text{tx}_m) = \sum_{i=1}^{N_F} |\mathbf{E}_{\text{HP}}^{\text{rcstr}}(\rho, \phi; \text{tx}_m; f_i)|^2 \quad (3.4)$$

The images reconstructed using Eq. (3.4) may have artefact affect i.e., some time there may be clutters or complete masking of the localised inclusion due to the transmitter antenna reflection occurring inside the phantom. Hence, the artefact removal process is very important as it can overlap the localised tumour/cancerous tissues in the reconstructed image. For that purpose, an alternative approach can be used; Instead of one fixed transmitting tx_m , the adjacent transmitting position tx_{m1} with an angular distance of 5° on each side can be utilized, and then subtract the both calculated fields to remove the artifact as:

$$\mathbf{E}_{\text{HP}}^{\text{rcstr}}(\rho, \phi; \text{tx}_m - \text{tx}_{m1}; f) = \sum_{n=1}^{N_{PT}} (\mathbf{E}_{i_{\text{np}}, \text{tx}_m}^{\text{known}} - \mathbf{E}_{i_{\text{np}}, \text{tx}_{m1}}^{\text{known}}) G(k_1 |\vec{\rho}_{np} - \vec{\rho}|) \quad (3.5)$$

The basic idea behind the methodology of artefact removal is to subtract the adjacent radar measurements based on the position of the transmitting source's position, which in return cancels the reflection effect caused inside the phantom. This methodology has been proven successful in [41–43]. The algorithm is succinctly outlined below in the form of pseudo code, providing a concise overview of its key components and operations.

Algorithm 1 Huygens Principle 2D Imaging Algorithm

- 1: Load the recorded complex signals S21 via measurements.
 - 2: Initialize constants for free space parameters.
 - 3: Define source parameters.
 - 4: Specify observation grid: $X_{\text{reconstr}}, Y_{\text{reconstr}}$.
 - 5: Set frequency parameters: `freq`, `new_freq_sample`.
 - 6: Applying Huygens principle based MWI algorithm (frequency domain):
 - 7: **for** $i = 1$ to $fmax$ **do** ▷ Loop over frequency samples
 - 8: **for** $np = 1$ to NP **do** ▷ Loop over observation points
 - 9: Compute scattered field contribution using Huygens principle.
 - 10: **end for**
 - 11: **end for**
 - 12: Accumulate incoherent summation
 - 13: **for** $i = 1$ to $\text{freq_samples} \times 1$ **do**
 - 14: Accumulate incoherent scattering contributions.
 - 15: **end for**
 - 16: Reconstructing Images via plotting techniques.
-

3.4 Lung COVID-19 Infection Detection via UWB MWI

COVID-19, the global pandemic that emerged in late 2019, has caused widespread health concerns worldwide. In patients with COVID-19, lung lesions can be detected through chest CT imaging, even in asymptomatic individuals, showing the evolution of diffuse bilateral ground-glass opacities [44]. However, the routine use of CT as a screening tool is not recommended, and it should be reserved for hospitalized and symptomatic patients. Furthermore, the accumulation of ionizing radiation from CT scans may pose health risks, especially when used for monitoring and tracking COVID-19 treatment [45], due to the multiple sources of ionized x-rays involved. Microwave imaging, on the other hand, has garnered increasing attention, particularly for its potential in breast cancer detection. The significant contrast in dielectric properties at microwave frequencies (1-10 GHz) between normal and malignant tissues has motivated researchers to explore microwave imaging for various medical applications [46]. Besides breast cancer detection, microwave imaging has been applied in brain stroke classification, bone imaging, and lung cancer detection [47,48].

In a study mentioned in [47], researchers introduced a three-dimensional electromagnetic torso scanner operating between 0.83 and 1.9 GHz, demonstrating its potential for medical imaging applications. Studies in [47, 48] report that cancerous tissues exhibit up to 3 times higher relative permittivity and 2 times higher conductivity compared to normal tissues, highlighting the potential of microwave imaging in differentiating between healthy and malignant tissues. Unlike CT, microwave imaging utilizes non-ionizing radiation, making it a safer alternative for medical imaging. The ability of microwave imaging to detect variations in dielectric properties has shown promise in various medical conditions, including lung cancer detection and potentially COVID-19 lung lesions. By employing MWI, healthcare practitioners can avoid the risks associated with ionizing radiation while efficiently monitoring lung lesions in COVID-19 patients and other medical conditions. As researchers continue to explore and refine the capabilities of microwave imaging, its potential impact on medical diagnostics continues to grow, offering a safer and reliable imaging modality for a wide range of applications. COVID-19 infection leads to ground-glass opacities in the lungs, which implies a contrast in dielectric properties compared to the surrounding normal tissues [49]. This characteristic suggests that mi-

microwave imaging could be used to detect such opacities, which are larger in size than lung cancers.

This research experiment aims to assess the capability of the proposed HP procedure in detecting lung COVID-19 infection through measurements inside an anechoic chamber using dedicated phantoms that mimic the dimensions and dielectric properties of a human torso, including a target that mimics an infection. To detect lung COVID-19 infection inside the human torso phantom, frequency-domain measurements were performed in an anechoic chamber using a VNA arrangement to obtain the transfer function (S_{21}) between two microstrip antennas operating between 1 and 5 GHz in a multi-bistatic fashion. This frequency band has been found to be optimal for lung imaging [47], and previous research [41] has highlighted that a large bandwidth can enhance performance in lesion detection. The S_{21} signals obtained from the measurements are then used for image reconstruction, with artefacts removed through a rotation subtraction procedure. By utilizing the HP and performing frequency-domain measurements, this research seeks to evaluate the potential of microwave imaging for detecting lung COVID-19 infection in a human torso phantom. The use of anechoic chambers and realistic phantoms allows for a controlled and reliable assessment of the proposed methodology. The findings from this study may contribute to the development of a safer and more efficient medical imaging technique for COVID-19 lung lesions and potentially other lung-related conditions.

3.4.1 Lung Phantom Fabrication

The design and fabrication process of the human torso phantom for microwave imaging experiments is detailed in this section. The objective was to create a realistic phantom with appropriate relative permittivity and conductivity to validate the efficiency of the HP imaging algorithm in detecting lung COVID-19 infection. The torso-mimicking phantom is composed of two layers in an elliptical shape. The external layer of the phantom is designed in an oval shape with axes measuring 31 cm and 20 cm, and a height of 25 cm. The circumference of the external layer is 82 cm, which is representative of a small-size chest circumference. The internal layer of the phantom is also oval shaped with axes of 27 cm and 14 cm, and a height of 25 cm. The two-layer configuration aims to mimic the complex structure of the human torso.

To simulate an infection or lesion, a small cylindrically shaped plastic tube with a

volume of 15 ml has been mounted on the inner layer’s wall. This cylindrical inclusion serves as the target mimicking the lung COVID-19 infection for the microwave imaging experiments. The fabrication of the phantom involves carefully choosing the materials with relative permittivity and conductivity that closely match those of human tissues. The elliptical shape of the phantom represents the human chest region more accurately, and the inclusion of the cylindrical target allows for the validation of the HP imaging algorithm in detecting lung lesions.

The phantom’s dimensions and materials are selected based on empirical data and knowledge of the dielectric properties of lung tissues. By creating a realistic phantom with appropriate dielectric properties, the experiments can accurately assess the capability of the HP-based microwave imaging in detecting lung COVID-19 infection. Fig. 3.5 illustrates the design and configuration of the human torso phantom with the internal cylindrical inclusion, which will be used for the microwave imaging experiments. This phantom will serve as the test subject to validate the proposed methodology for lung infection detection using microwave imaging in the frequency range of 1 to 5 GHz.

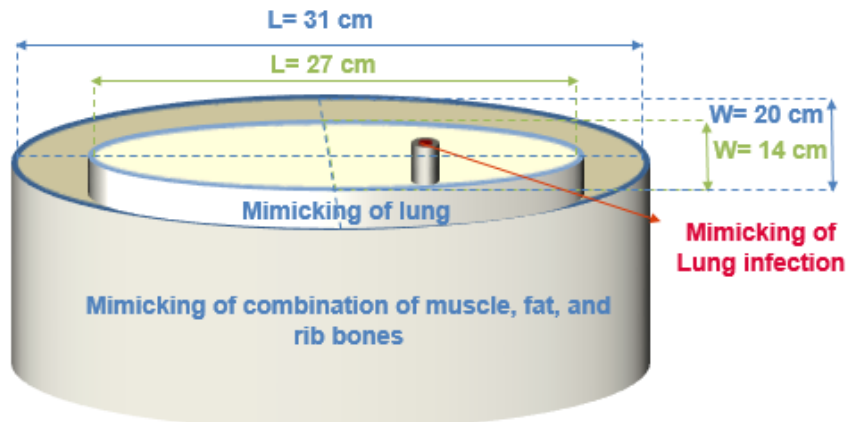


Figure 3.5: Design of lung COVID-19 infection Phantom.

The external layer mimics a combination of muscle, fat and rib bone tissues; the internal layer mimics the lung tissue, and the cylindrical tube simulates the lung infection. Table. 3.2 displays the dielectric properties of real tissues, derived from [50, 51].

The fabrication process of the human torso phantom involved several steps to accurately mimic the dielectric properties of the different tissues in the chest region.

Preparation of lung layer: A small oval-shaped container was used to represent the lung tissue. Glycerol, with a relative permittivity of 10 and conductivity of 0.1 S/m at 2 GHz, was filled inside the container. Glycerol was chosen as it closely mimics the

Table 3.2: Relative permittivity and conductivity at a frequency of 2 GHz.

Different Layers of Human Torso Phantom	Relative permittivity	Conductivity (S/m)
Fat	5	0.08
Muscle	50	1.45
Rib Bone	12	0.3
Lung (inflated)	20	0.1
Lung infection	60	2.5

dielectric properties of the lung tissue when it is inflated.

Positioning of lung layer: The small oval-shaped container filled with glycerol was placed inside the external layer of the phantom. This internal layer represented the lung tissue in the chest. **Filling Surrounding Space:** A dedicated oil (TLe11.5C.045) was used to represent a combination mixture of muscle, fat, and rib bone tissues. This oil has a relative permittivity of 7 and conductivity of 0.3 S/m at 2 GHz [52,53]. The oil was poured to completely fill the remaining space surrounding the lung layer. This step ensured that the external layer accurately mimicked the dielectric properties of the combination of muscle, fat, and rib bone tissues.

Lung infection simulation: A small cylindrically shaped plastic tube was filled with tap water. This tap water served as the material to simulate the lung infection. The tube was then positioned inside the internal wall of the phantom, representing the region of infection within the lung tissue.

By following these steps and using materials with the appropriate dielectric properties, the human torso phantom was successfully fabricated. The phantom represented the complex structure of the human chest, with distinct layers mimicking different tissues and an inclusion representing the lung infection. Fig. 3.6 provides a visual representation of the fabricated human torso phantom.

Indeed, the fabrication process of the human torso phantom was meticulously carried out with careful consideration of the dielectric properties of each layer to accurately mimic the different tissues present in the human chest. Table 3.2 provided the dielectric properties of the real tissues, which served as a reference for selecting the appropriate materials for each layer. To ensure the authenticity of the phantom, stability of the materials used was considered. The selected materials could maintain their dielectric properties over the desired frequency range, which is crucial for the success of the microwave imaging



Figure 3.6: The lung COVID-19 infection fabricated phantom.

experiments.

Moreover, geometric dimension similarity was a key aspect during the fabrication process. The dimensions of each layer, including the external and internal layers, were carefully designed to closely resemble realistic scenarios in the human chest. By adhering to these realistic dimensions, it was ensured that the phantom closely mimicked the actual anatomical structure of the chest. The careful consideration of dielectric properties, material stability, and geometric dimension similarity in the fabrication procedure enhances the reliability and accuracy of the human torso phantom. As a result, the phantom is well-suited for performing microwave imaging experiments in the frequency range of 1 to 5 GHz to validate the efficiency of the HP imaging algorithm in detecting lung COVID-19 infection.

3.4.2 Experimental Methodology

The frequency domain measurements for detecting lung COVID-19 infection were conducted within the anechoic chamber at LSBU. To capture the backscattered signals from the human torso phantom, a multi-bistatic configuration was employed, involving two different UWB antennas that are vertically polarized and omni-directional in the azimuth plane. These antennas were placed in free space and connected to the VNA (model MS2028C, Anritsu) for transmitting and receiving signals after calibration. In the multi-

bistatic fashion, one antenna served as the transmitter, while the other acted as the receiver, rotating around the object (human torso phantom) to collect the scattered S_{21} signals in various directions.

The multi-layered infected lung phantom was positioned at the centre of a rotatable table, 21 cm and 30 cm away from the receiver and transmitter antennas, respectively. The measurement procedure involved two different transmitting positions, placed at 0° and 5° . For each transmitting position, the S_{21} signal was recorded for 60 receiving points, with a rotation interval of 6° , covering the frequency range from 1 to 5 GHz, using a frequency sample spacing of 5 MHz.

The experiment was repeated for the "healthy" scenario, representing the torso phantom without the lung-infection layer, to serve as a reference for comparison. Figures 3.7 (a) and (b) provide a visual representation of the measurement setup and the position of the multi-layered torso phantom inside the anechoic chamber, respectively.

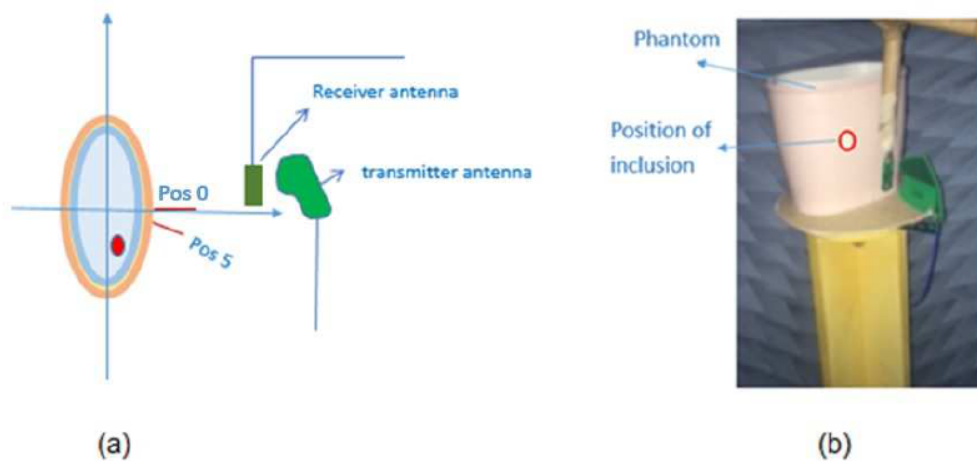


Figure 3.7: (a) Pictorial view of the measurement set up; (b) Position of the torso phantom inside the anechoic chamber. The phantom was placed on the centre of a rotatable table. The external UWB antenna is the transmitter, and the internal PulsON P200 antenna is the receiver.

3.4.3 HP-based Imaging Algorithm

The HP imaging procedure has been applied to the measured complex S_{21} of the VNA to reconstruct the images [43]. Specifically, the torso phantom, which has been placed in free space, is exposed to the signal emitted by the transmitter antenna located at the position TX_m . The S_{21} signals have been collected at the point $RX_{np} \equiv (r_0, \phi_{np}) \equiv \rho_{np}$ by rotating the receiving antenna around the phantom displaced along a circular surface having radius

r_0 (see Figure. 3.8), which can be expressed as $S_{21_{TX_m}}|_{RX_{np}} = S_{21_{np, TX_m}}$. The position of the receiving antenna is shown by RX_{np} , where np is the number of receiving positions that varies from 1 to N_{PT} , and subscript m represents the transmitting positions with $m = 1, 2$. The two transmitting positions displaced 5° apart from each other have been synthesized by accurately rotating the phantom instead of displacing the transmitting antenna positions.

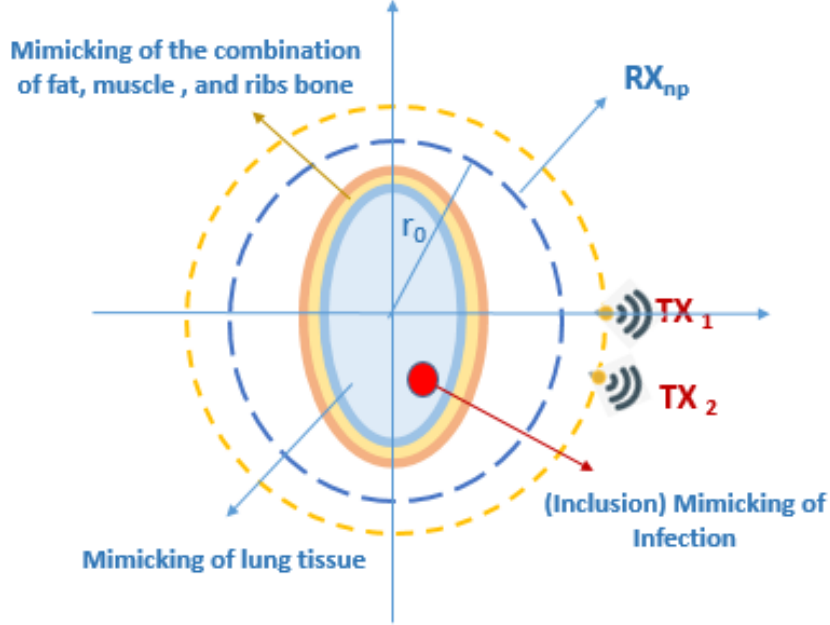


Figure 3.8: Pictorial view of the measurements.

By referring to HP, It can be written as in [43]:

$$E_{HP,2D}^{rcstr}(\rho, \phi; TX_m; f) = \Delta_s \sum_{np=1}^{N_{PT}} S_{21_{np, TX_m}}^{known} G(k_1 |\rho_{np} - \rho|) \quad (3.6)$$

In Eq. (3.6), the observation point is shown by $(\rho, \phi) \equiv \rho$, while the spatial sampling and wave number are presented by the parameters Δ_s and k_1 respectively. In $E_{HP,2D}^{rcstr}$, two strings "rcstr" and "HP" indicate the reconstructed internal field and the employed Huygens principle-based procedure, respectively. $G(k_1 |\rho_{np} - \rho|)$ represents the Green's function.

Subsequently, the intensity of the final image I can be defined by assumption of using N_f frequencies through Eq. (3.4), i.e., by summing incoherently all the solutions.

To address the issue of artefacts in the measured data, a signal pre-processing method was applied to suppress these artefacts and achieve accurate detection. Two distinct

artifact removal methods were employed in this research:

- **Rotation Subtraction:** In this method, the S_{21} signals obtained from two slightly displaced transmitting positions (5° apart) were subtracted from each other. This rotation subtraction helps to eliminate artefacts, such as images of the transmitter or reflections of the layers, which could potentially mask the region of interest.
- **Ideal Artefact Removal:** This method involved subtracting the data obtained from a “healthy” torso phantom (without lung infection) from the data of the multi-layered torso phantom with lung infection. By performing this subtraction, the artefacts specific to the lung infection scenario were effectively removed, leaving behind only the relevant information for accurate detection [54].

To evaluate the performance of the imaging procedure, image quantification was introduced using a metric called the Signal to Clutter Ratio (SCR). The SCR is calculated as the ratio between the maximum intensity evaluated within the region of the lesion (lung infection) and the maximum intensity outside the region of the lesion. This metric provides a quantitative measure of the ability of the imaging algorithm to distinguish between the lesion and the surrounding healthy tissues. By applying these artefact removal methods and quantifying the images using SCR, the research aimed to enhance the accuracy and reliability of the microwave imaging algorithm in detecting lung COVID-19 infection inside the human torso phantom. These techniques contribute to improving the sensitivity and specificity of the imaging system for potential future clinical applications.

3.4.4 Reconstructed Images

In Fig. 3.9, the microwave image of the phantom is presented after employing the rotation subtraction artefact removal procedure between S_{21} signals obtained using transmitting positions 0° and 5° . While some residual clutter can be observed in the image, the lung infection inclusion is clearly detectable in its correct position. In Fig. 3.10, the microwave image of the human torso phantom is shown after performing the “ideal” artefact removal procedure, which involves subtracting the data obtained from a healthy torso phantom from the data of the torso phantom with lung infection. As depicted in Fig. 3.10, the lung infection inclusion is visible in its correct position without any residual clutter. This result

confirms the effectiveness of the artefact removal method using the difference between the data of a healthy torso phantom and the data of a torso phantom with lung infection.

It is important to note that all the presented images have been normalized and adjusted, with intensity values below 0.5 being forced to zero. This normalization process enhances the visualization of the relevant features and helps in distinguishing the lung infection from the surrounding tissues. Overall, the microwave imaging algorithm based on HP has shown promising results in detecting lung COVID-19 infection inside the human torso phantom. By employing appropriate artefact removal methods, the algorithm has been able to enhance the accuracy and reliability of the images, making the lung infection clearly visible in its correct position. These findings validate the efficiency of the proposed HP imaging procedure for lung infection detection and contribute to the potential application of microwave imaging in medical diagnostics.

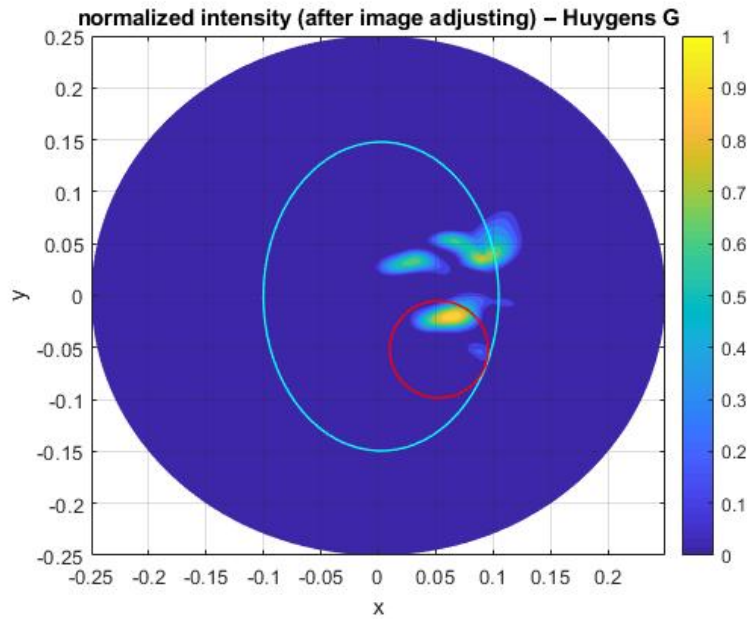


Figure 3.9: Microwave image of the human torso phantom employing frequency range of 1-5 GHz after performing rotation subtraction artifact removal procedure using the difference between measurements obtained with transmitting positions 0° and 5° ; Images are obtained following normalization to their correspondent maximum values and forcing to zero the intensity values below 0.5 (x and y axes are given in meters); the blue elliptical shows boundary of the phantom and red circle represents the possible detected infection.

The visual inspection of the microwave images obtained using the imaging procedure confirms its capability for lung infection detection. The lung infection inclusion is clearly visible in its correct position, indicating the successful detection of the infection using the microwave imaging algorithm based on HP. In addition to visual inspection, image

quantification has been performed by calculating the SCR. The SCR value is a metric that provides a quantitative measure of the imaging performance in terms of detecting the lung infection while suppressing artefacts and clutter in the image. When applying the rotation subtraction artefact removal procedure, the calculated SCR value is 4.65 dB. This indicates a good level of performance in terms of distinguishing the lung infection from the surrounding clutter, but there is still some residual clutter in the image.

On the other hand, when using the “ideal” artefact removal procedure, the calculated SCR value increases to 7 dB. This higher SCR value suggests that the “ideal” artefact removal method effectively removes the clutter and enhances the visibility of the lung infection, resulting in a more accurate and reliable detection. The increase in SCR value when using the “ideal” artefact removal procedure highlights the importance of employing appropriate artefact removal techniques in microwave imaging. It also demonstrates the significance of image quantification in evaluating the performance of the imaging procedure and provides valuable insights for further optimization and improvement.

Overall, the combination of visual inspection and image quantification through SCR calculation reaffirms the effectiveness and potential of the proposed microwave imaging algorithm for lung infection detection. The promising results encourage further research and development in this area to advance the application of microwave imaging in medical diagnostics, especially for detecting lung infections like COVID-19.

3.4.5 Experimental Analysis

The experiment presented in this study demonstrates the feasibility of using microwave imaging based on HP for detecting lung COVID-19 infection. The measurements were conducted on a human torso phantom inside an anechoic chamber using two Microstrip antennas operating in the frequency range of 1 to 5 GHz. The successful identification of the lung infection was achieved by applying an artefact removal procedure to eliminate unwanted images that could mask the region of interest. The rotation subtraction artefact removal method, which involves using two slightly displaced transmitting positions, and the “ideal” artefact removal method, involving the subtraction of data between a healthy torso phantom and an infected torso phantom, were both effective in suppressing artefacts and enhancing the visibility of the lung infection. The quantification of the microwave images using the SCR yielded a value of 7 dB, indicating a high level of performance in

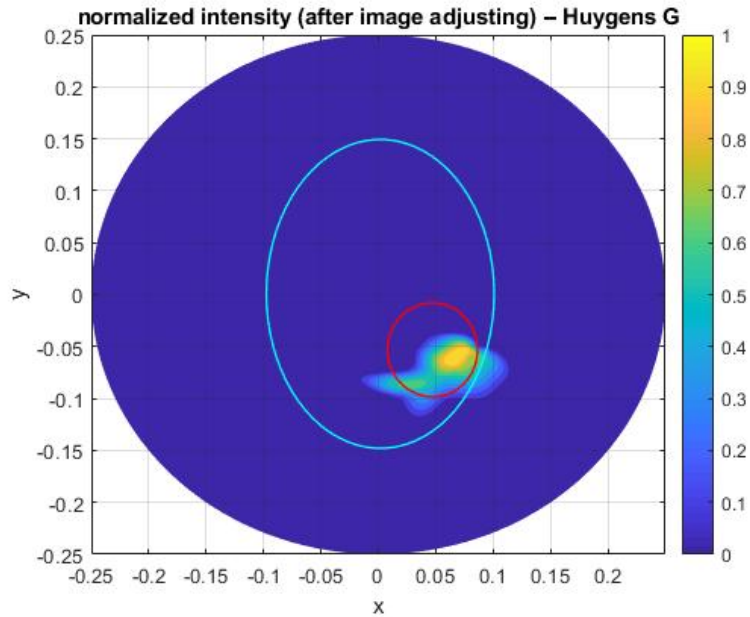


Figure 3.10: Microwave image of the human torso phantom employing frequency range of 1-5 GHz; after performing “ideal” artifact removal procedure; using the difference between obtained data of a healthy torso phantom and the data of torso phantom having lung infection. Images are obtained following normalization to their correspondent maximum values and forcing to zero the intensity values below 0.5 (x and y axes are given in meters);the blue elliptical shows boundary of the phantom and red circle represents the possible detected infection.

distinguishing the lung infection from surrounding clutter.

One of the key advantages of the HP-based technique is its versatility in handling different measurement setups. It can be used with antennas and phantoms placed in free space, eliminating the need for coupling liquids and simplifying the experimental setup. Additionally, HP does not require prior knowledge of the antennas’ responses, making it easier to implement and integrate into a cost-effective and user-friendly device. The potential of the HP-based technique for remote pre-hospital examinations and monitoring of Lung COVID-19 infection is noteworthy. With its ability to detect lung infections and its ease of use and integration, this microwave imaging approach shows promise in facilitating early detection and monitoring of COVID-19 cases, especially in remote or resource-limited settings. By providing a non-invasive and radiation-free imaging solution, this technique may contribute to improved medical diagnostics and patient care, offering valuable insights and potential benefits for healthcare providers and patients alike.

3.5 Lung Lesion Detection via MWI Implementing Realistic Parameters

Lung cancer is one of the foremost causes of mortality worldwide, with an estimated death toll reaching 1.8 million in 201 [55], with 2.1 million cases discovered annually [56], making it a global health problem. Lung cancer can be subdivided into two main types based on cell structural properties: small cell lung cancer (SCLC) comprises 15% of the cases discovered annually, while the remaining 85% fall into the non-small cell lung cancer (NSCLC) category [56]. Lung cancer is most likely to be diagnosed in countries with a high smoking population. In the UK, the mortality rate caused by lung cancer is higher than any other type of cancer, with a 5-year survival rate of less than 13%, which is quite alarming [57]. Early detection of lung cancer, lung lesions, and lung damage can significantly improve treatment outcomes and save lives.

Currently, screening for lung cancer involves the use of x-rays and x-ray-based CT scans, which are considered reliable but sometimes require additional tests for accurate location of the lung cancer. Other methodologies include MRI and, in more complex cases, biopsy of possible cancerous lung tissues. However, all these conventional medical imaging techniques use ionizing radiation, which can pose health risks to patients. Additionally, lung cancer is often screened for after physical symptoms are discovered, by which time the cancer growth may have already progressed significantly. Researchers have therefore considered using UWB microwave imaging technology to detect lung cancer at an early stage, as UWB has shown promising results in breast lesion detection [58]. MWI relies on differentiating healthy and cancerous tissues based on the difference in their dielectric properties. Studies have shown that the dielectric properties of cancerous tissues are significantly higher than those of healthy tissues [59, 60] providing an opportunity for improvement and significant results.

Recently, a new MWI approach based on the Huygens Principle for lung cancer and infection detection has been presented. The researchers fabricated a lung phantom to match realistic parameters in terms of dimensions and dielectric properties contrast [61]. The reconstructed images indicated successful localization but leave room for improvement by using more realistic parameters. In this research, I have attempted to overcome the challenge of using realistic parameters by adopting a professional approach and applying the

HP-based MWI methodology to validate its capability. Specifically, the investigation of lung lesion detection using MWI has been performed with the aid of a fabricated phantom with varying dielectric properties. For this research, I have used the multi-layered chest phantom V1 by Schmid & Partner Engineering AG (SPEAG) as the phantom and Tissue Simulating Liquids (TSL) for its fabrication. The inclusion exhibiting realistic dielectric properties and placed it inside the phantom. The measurements were performed inside an anechoic chamber using two UWB antennas connected to the VNA and an amplifier to enhance the signal strength. The measurements were performed in the frequency domain, and the data was collected as the complex S21 signals. The data were then processed using the HP-based imaging algorithm to reconstruct images with the localized inclusion [61]. The HP-based technique has the advantage of not requiring knowledge of antenna responses and can be easily integrated into a cost-effective and easy-to-use device for dedicated detection space, enabling remote pre-hospital examinations and monitoring of Lung COVID-19 infection.

3.5.1 Phantom Fabrication

In this research, a multi-layered chest phantom (Figure 3.11), which was designed and developed by SPEAG in Switzerland [62] was utilized. This phantom was specifically developed to provide accurate evaluation with realistic parameters and assured quality when integrated with medical devices and exposed to high-frequency radiations. The phantom presented in [62] is known for its precise and repeatable assessment with path loss in real humans, including inner-tissue reflections. With dimensions of 400mm width, 260mm depth, and 365mm height, the phantom matches realistic parameters effectively. The phantom consists of two different layers or volumes: an inner volume with a size of 6.2 liters and an outer volume with a size of 8.2 liters, separated by high precision low radio frequency loss plastic to ensure accuracy and authenticity. The outer layer, depicted in black in Figure 3.11, is a skin layer manufactured using a mixture of silicon and carbon, with dielectric properties that closely match the skin of a human arm, as stated in [62]. One of the essential features of this phantom is its reusability for multiple experiments, and it comes with handles on both sides for easy handling during fabrication of the inner layers/volumes. By employing this advanced multi-layered chest phantom, precise and realistic parameters were achievable for performing measurements, which contributes to

the validity and reliability of the results obtained in this research.



Figure 3.11: Multi-layered chest phantom V1 by SPEAG.

To simulate the lung lesion, a cylindrical tube with a volume of 15 mL was fabricated with a mixture that mimics the dielectric properties of lung tissues. This inclusion was then placed inside the internal layer of the multi-layered chest phantom. To ensure proper placement and suspension of the inclusion, a moving knob on the top of the phantom was used. The main objective of this research was to conduct experiments with realistic parameters, including the dielectric properties of lung tissues and lesions, as presented in [61, 63]. For this purpose, various mixtures have been utilized to simulate different tissues, and the details of these mixtures are provided in Table 3.3. Additionally, the phantom-compatible liquids developed by SPEAG have been used to fabricate the muscle and fat layers, with more information available in [62] (Figure 3.12). By using these mixtures and phantom-compatible liquids, I was able to create a realistic and accurate representation of human tissues and lesions within the chest phantom.

Indeed, the tissue simulating liquids provided by SPEAG have been crucial in fabricating the multi-layered chest phantom with realistic dielectric properties. The internal layer, which simulates lung tissue, and the outermost layer, which mimics skin, were both fabricated using the tissue simulating liquids to achieve dielectric properties like muscle, fat, and lung tissues. Additionally, the external layer of the phantom, which represents rib bone tissues, was fabricated using a specific oil mixture to closely match the dielectric properties of rib bones. The mixtures used in the fabrication process were carefully se-



Figure 3.12: Top view of filled multi-layered SPEAG chest phantom.

lected to be optimistically close to the realistic dielectric properties of the multiple layers, including the fabricated inclusion representing the lung lesion.

Table 3.3: Dielectric Properties of Fabricated Materials at 1.75 GHz.

Fabrication material	Relative permittivity (ϵ_r)	Conductivity (σ) [S/m]
Tissue simulating liquid (internal layer)	43.2	1.37
Sunflower oil (external layer)	5	0.34
Water and Salt	78	2

3.5.2 Measurement Setup inside Anechoic Chamber

The experimental setup for conducting measurements inside the anechoic chamber involved several key components. Two UWB antennas, specifically the Planer Horn Antenna 310C, were utilized for both transmitting and receiving signals. These antennas were vertically polarized and emitted radiations omni-directionally in the azimuth plane while being placed in free space within the anechoic chamber. The VNA used in this research was the 2-port Cobalt Series VNA manufactured by Copper Mountain in Indianapolis, IN, USA. The UWB antennas were connected to the transmitter and receiver ports of the VNA. The VNA was controlled by a laptop through a USB port, which allowed it to record the transfer function (S_{21}) between the two antennas in terms of complex signals.

To facilitate the measurements, a rotating table was incorporated into the setup. The rotating table enabled the recording of measurements at different angles around the phan-

tom, which was placed on a stand inside the anechoic chamber. The stand was designed to securely hold the multi-layered chest phantom during the experimentation process. Figure 3.13 illustrates the complete experimental setup inside the anechoic chamber, showing the positioning of the UWB antennas, VNA, rotating table, and the multi-layered chest phantom during the measurements. This setup allowed for the collection of the necessary data to validate the efficiency of the HP-based microwave imaging algorithm for detecting lung COVID-19 infection.

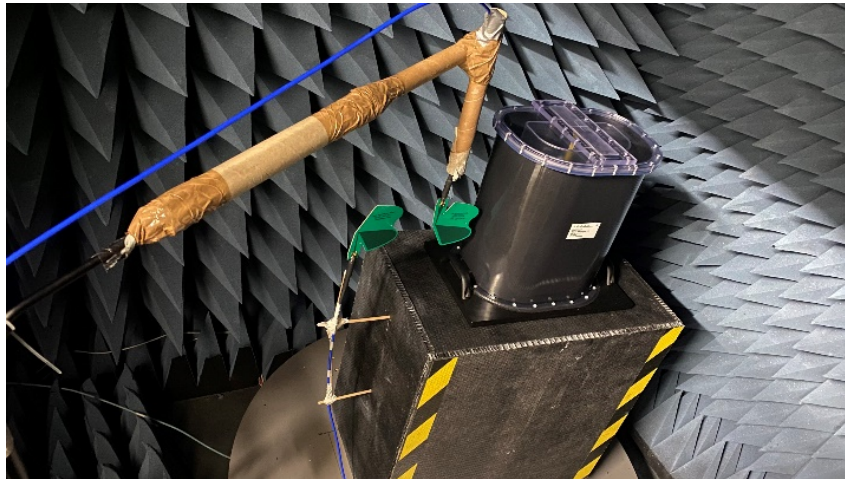


Figure 3.13: Experimental Setup inside Anechoic Chamber.

The experimental setup utilized the frequency domain, with a frequency range of 0.5 GHz to 3 GHz. The chosen low frequency range was intended to enhance signal penetration through the phantom, thereby achieving better results, although some image resolution was compromised. The two UWB antennas used in the setup were aligned, with the transmitter antenna attached to the stand that held the multi-layered chest phantom. The transmitter antenna rotated along with the phantom, while the receiver antenna remained fixed with the aid of the stand. For each set of measurements, two adjacent transmitting positions, 5 degrees apart, were utilized. The measurements were initiated from 0 degrees and recorded every 6 degrees, continuing until 360 degrees, resulting in a total of 60 recorded measurements for each transmitting position. Figure 3.14 illustrates the basic experimental configuration, showcasing the placement of the UWB antennas, the rotating stand holding the phantom, and the fixed receiver antenna.

In the experiment described in this section, microwave imaging was conducted using the setup shown in Figure 3.14. Multiple measurements were performed with the transmitting antenna placed at different positions, and the direction of the phantom was



Figure 3.14: Experimental Schematics.

changed from vertical to horizontal by rotating the phantom by 180 degrees. However, despite these efforts, the results showed only artifacts and transmitter image reflections, and no successful detection was achieved. Upon troubleshooting, it was discovered that the signal power was not strong enough, especially at 180 degrees where the antennas were at their farthest positions. This weak signal reception was attributed to the realistic parameters of the setup.

To overcome this challenge, an amplifier by Mini Circuits, specifically the ZX60-8008E model, was incorporated into the experimental setup. The amplifier was connected between the Vector Network Analyzer (VNA) and the transmitting antenna to boost the signal power. With the amplified signal, the weak reception issue was addressed, and the transmitter reflection in the reconstructed images was minimized. The schematic of the experimental setup with the amplifier is depicted in Figure 3.15. By using the amplifier, the signal power at the farthest positions was increased by approximately 15 dB, thus improving the overall performance of the microwave imaging procedure. With this enhanced setup, the researchers aimed to achieve better results and increase the accuracy of the detection process during further experiments.

3.5.3 Image Reconstruction

The images with the detected lesion were reconstructed via HP-based MWI algorithm as presented in the previous section. The measurements were performed at the two adjacent transmitting positions (5° apart). Therefore, I subtracted the signals recorded from both transmitting positions to remove the artefact and furthermore measurements were performed at the same position without inclusion and then subtracted the signals with and without inclusion. The images reconstructed after implementing the HP based

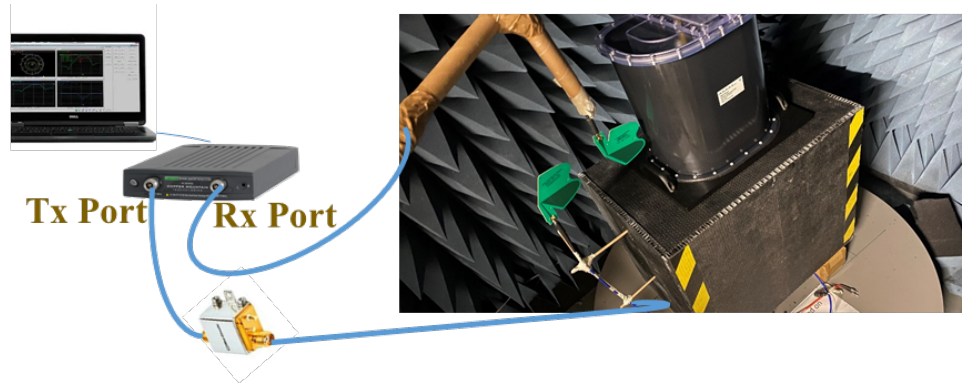


Figure 3.15: Experimental Schematics (with amplifier).

MWI imaging algorithm are shown in Figures 3.17 and 3.18. In Figure 3.17, the actual position of the detected inclusion is represented by the red circle. The detected inclusion is aligned with the yellow part with higher intensity. It is important to note that the images in Figures 3.17 and 3.18 are not raw images, but they have been normalized to the maximum value to highlight the detected inclusion.

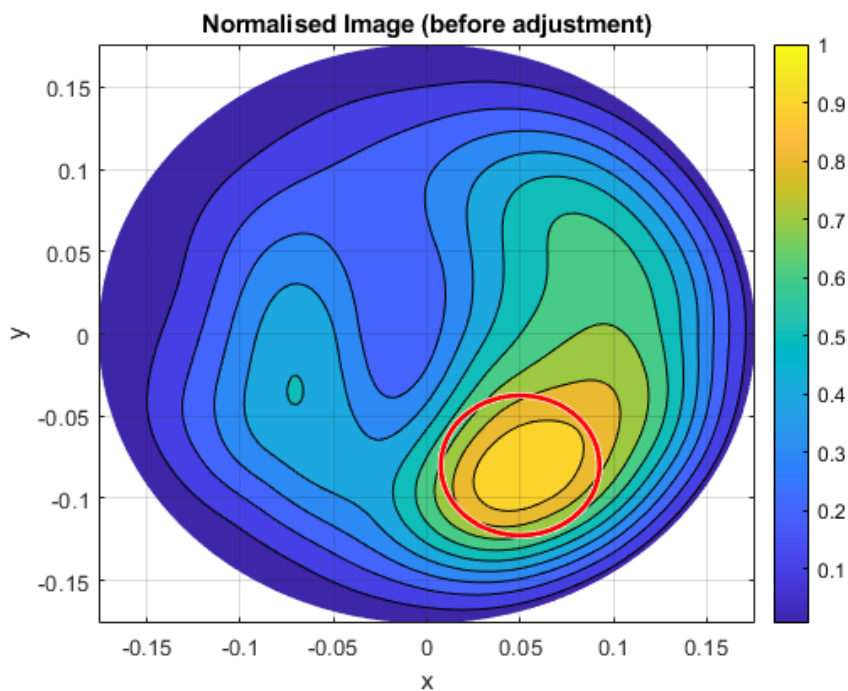


Figure 3.16: Reconstructed Image with the detected inclusion (before image adjustment).

In Figure 3.18, the artefact removal has been applied by subtracting the signals from the two adjacent transmitting positions. It can be observed that the proposed methodology has been successful in removing transmitter reflections and highlighting the inclusion more prominently. The detected inclusion is aligned with the red circle, which indicates

the original position of the inclusion and validates the accuracy of the detection. This is further supported by the calculated SCR of 9.97 dB for the normalized image before image adjustment. Moreover, after implementing the image adjustment methodology and image adjustment, the SCR increases from 9.97 dB to 13.48 dB, demonstrating the successful implication of the technique along with the removal of artefact residuals. The increased SCR value indicates a higher level of confidence in the accuracy of the detection and the localization of the inclusion within the phantom.

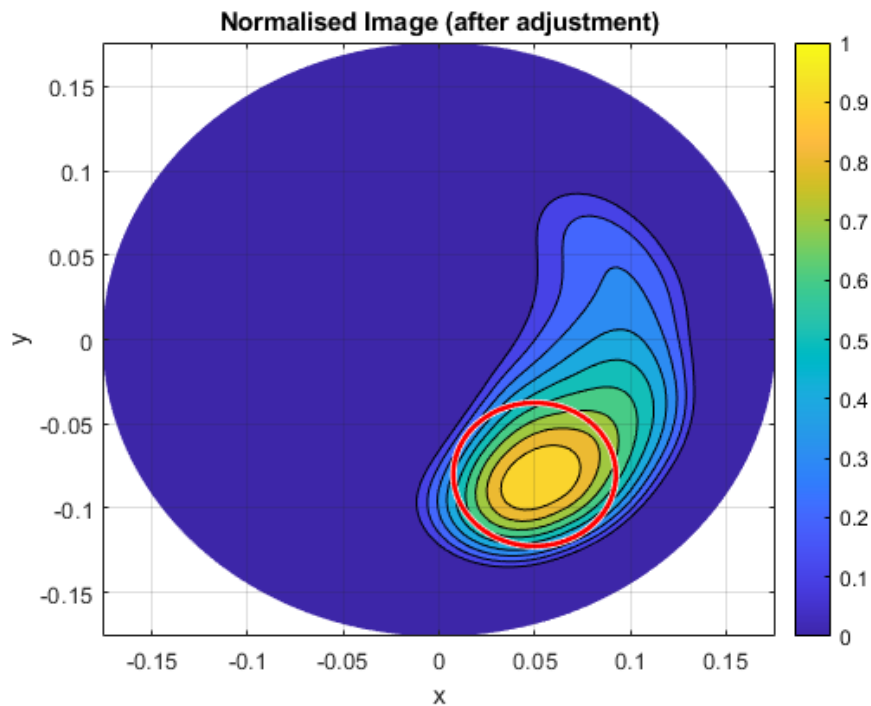
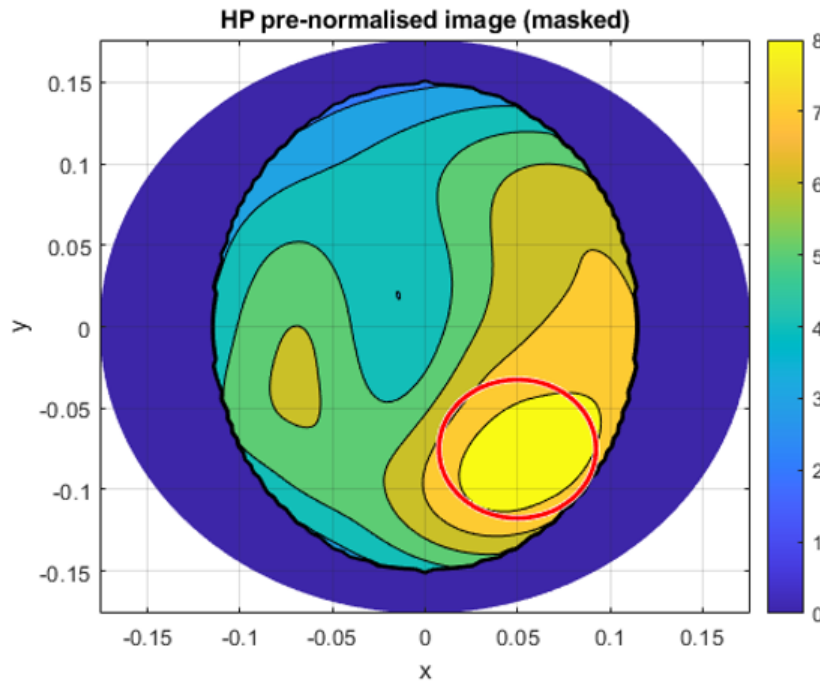


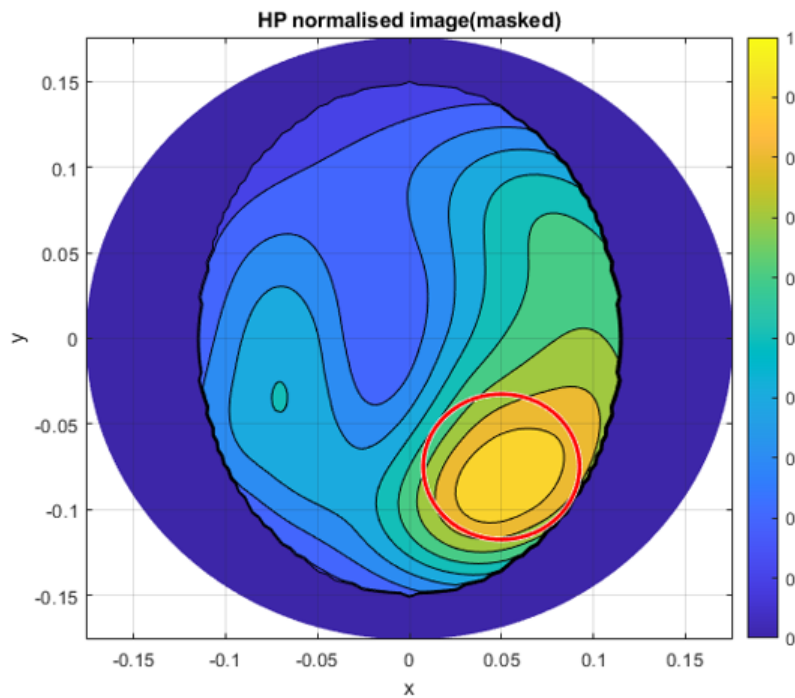
Figure 3.17: Reconstructed Image with the detected inclusion (after image adjustment).

Figures 3.17 and 3.18 further highlight the region of interest, which corresponds to the multi-layered chest phantom with the detected inclusion. To achieve this, a mask has been applied to the reconstructed images to outline the margin of the external layer of the phantom. Figures 3.19 (a) and (b) display the highlighted area with an elliptical margin equivalent to the dimensions of the fabricated phantom, represented in the normalized axis. These images show the detected inclusion before and after image adjustment, respectively. The application of the mask helps to visually focus on the specific region of interest and provides a clearer representation of the detected inclusion within the phantom.

The masking of the rest of the reconstructed image serves multiple purposes in this research. Firstly, it helps to highlight the boundary line of the phantom and facilitates the detection of the inclusion, which is essential for calculating the dimensional analysis



(a)



(b)

Figure 3.18: (a) Reconstructed Image with the detected inclusion & underlined margin of the phantom (before image adjustment), (b) Reconstructed Image with the detected inclusion & underlined margin of the phantom (after image adjustment).

error. The dimensional analysis error represents the difference between the dimensions of the realistic parameters of the inclusion and the dimensions detected in the reconstructed image. In this study, the dimensional analysis error is found to be less than 6%, indicating a high level of accuracy in the detection of the inclusion. Secondly, the masking of the reconstructed image allows to focus specifically on the region of interest, which is the multi-layered chest phantom with the detected inclusion. This focused view enables a more accurate and precise examination of the detected inclusion. Overall, the reconstructed images obtained from implementing HP-based microwave imaging technique have demonstrated the capability of MWI to detect lung lesions with realistic parameters. The successful detection of the inclusion within the phantom using MWI highlights its potential as a promising imaging technique for lung cancer detection and diagnosis.

3.5.4 Experimental Analysis

This research demonstrates the successful capability of the Huygens Principle-based MWI technique in detecting lung lesions using a multi-layered chest phantom. The phantom, designed by SPEAG, was specifically tailored for accurate evaluation of the chest, with tissue simulating liquids provided to mimic various body tissues, ensuring realistic dielectric properties. The experimental measurements were conducted inside the anechoic chamber, utilizing UWB planar horn antennas and a VNA by Cobalt Networks. The reconstructed images were generated through the HP-based imaging algorithm, resulting in the successful localization of the inclusion (lung lesion) within the phantom. To improve the quality of the reconstructed images and eliminate artefacts, a rotation subtraction technique was employed between two adjacent transmitting positions. This approach effectively removed any residual artefact, enhancing the accuracy of the detected inclusion. Additionally, an image-processing tool was introduced to highlight the region of interest by applying a mask, further improving the accuracy and precision of the evaluation process. Overall, the findings of this study showcase the potential and efficacy of HP-based MWI in detecting lung lesions with high accuracy and reliability. The combination of realistic phantom design, careful measurements, and advanced image processing techniques makes MWI a promising modality for early detection and diagnosis of lung cancer and other lung abnormalities.

3.6 Summary

This chapter provided a comprehensive overview of the experimental setup for the proposed MWI technology in this research, detailing the necessary hardware and parameters involved. The characteristics of the used hardware, including UWB antennas, VNA, rotating table, and stand, are briefly explained, along with the setup within the anechoic chamber. The chapter also delved into the HP-based MWI algorithm utilized in this research to differentiate between healthy and malignant tissues based on their dielectric properties. The fundamental principle behind HP is described, stating that each locus of the wave carries information from previous waves passing through the medium. HP does not calculate the exact external field but carries information about the dielectric properties of tissues, which aids in the detection of cancerous tissues. This algorithm has previously shown promise in detecting abnormalities in other biomedical applications, particularly breast cancer and brain strokes. The chapter further encompassed the measurements have been performed using the described method and hardware inside the anechoic chamber for lung COVID-19 infection detection. A multi-layered torso phantom mimicking lung tissues was fabricated, with mixtures having varied dielectric properties and an inclusion representing the infection. The phantom was placed at the centre of a rotating stand in the anechoic chamber, controlled by a Python GUI. UWB vertically polarized antennas were used for transmitting and receiving signals, connected to the VNA, which recorded complex S_{21} signals for two different transmitting positions with a 5-degree angular displacement. The obtained data was processed using the HP-based imaging algorithm, and the images were reconstructed, successfully detecting the inclusion, validated by the calculated SCR of 7 dB.

Additionally, a more complex experiment was conducted using a realistic phantom designed by SPEAG in Switzerland. This phantom closely matched the dimensions and dielectric properties of real humans, with multiple layers mimicking various tissues. UWB antennas with increased power, aided by an amplifier, were used to accommodate the realistic parameters of the lung phantom. The measurements have been recorded using a two-port VNA connected to a laptop, and the data was processed through the HP-based imaging algorithm, resulting in the successful detection of the inclusion. Image artefact removal was applied, and the images were normalized. The results were validated using image quantification parameters, demonstrating promising results in terms of SCR

and dimensional analysis error. Additionally, an image-processing tool was introduced to highlight the region of interest by applying a mask, further improving the accuracy and precision of the evaluation process. In conclusion, this chapter summarized the MWI technology and the proposed HP-based imaging algorithm, detailing a series of experiments performed to validate the approach, which yielded successful and validated results.

Chapter 4

Advanced MWI Device

4.1 Introduction

In the preceding chapter, the fundamental methodology of MWI and the HP-based imaging procedure is introduced. This chapter focuses on detailing the necessary hardware for the MWI measurement setup in the anechoic chamber. In the first experiment, measurements are conducted on a fabricated multi-layered phantom designed for detecting lung COVID-19 infections, featuring a fabricated inclusion. The fabricated inclusion is successfully localized by the HP-based imaging algorithm, and the resulting images are normalized and adjusted for better visualization, removing any artifacts. The second experiment is more intricate, involving a realistic phantom with dimensions mimicking human anatomy, and the outer layer of the phantom replicates the dielectric properties of human skin. Tissue-simulating liquids with realistic dielectric properties are used to create the multi-layered chest phantom, and an inclusion resembling a lung lesion is fabricated for localization. The capabilities of the HP-based imaging algorithm are again validated, with the localized inclusion quantified using SCR and dimensional analysis. Successfully validating the HP-based imaging algorithm and the measurement setup in the anechoic chamber. This chapter describes a novel, efficient, and accurate MWI device called MammoWave. A concise description of the device and the HP-based imaging algorithm is provided. Furthermore, the device's capabilities are illustrated through various experiments, highlighting its ability to deliver precise results. Additionally, this chapter expands on the HP-based imaging algorithm discussed in the previous chapter, specifically focusing on lung lesion detection. For preliminary experimentation and to validate

the device's capability, a lung phantom with minimal parameters is fabricated compared to the experiments in Chapter 3. The images reconstructed using the HP-based imaging algorithm for this experiment are validated through image quantification approaches. A brief comparison with the previously conducted experiment in the anechoic chamber is also presented.

4.2 Introduction to MammoWave

Breast cancer is one of the most common causes of mortality in the whole world, specifically in women. It is mostly symptom-free in the early stage and somehow only recognized while in the late stages of the disease, therefore early detection with the health risk-free environment was needed for the early cure of the disease. The most common and widely used medical imaging technology for breast cancer diagnostic is mammography, which uses multiple sources of low bout X-rays [64]. Mammography uses ionized rays and over-usage of this imaging methodology can cause health risks. Moreover, this technique is not the routine modality for the females of certain age group (40 years or less) but is suitable for women aged 45-50 years and over [64,65]. Besides this, there are other imaging methodologies as well for breast screening, involving self-examination (SE), which is done by the patient by looking for lymph and any sort of abnormalities in the breast and noticing a sudden change in the tissues of the breast.

Meanwhile, the other method is clinical examination (CE) implicating the medical health care specialist's involvement in the execution of a thorough physical examination of the breast for any possible irregularities [64]. Furthermore, there is ultrasonography involving ultrasounds and MRI. All these mentioned conventional medical imaging technologies are very costly with bulky hardware, and require healthcare assistance [66]. The other major drawback in the mentioned techniques is the age limitation a recent new research shows that the breast cancer diagnosed in women includes 6% of the women age under 40 years [67], and in Europe, the percentage increases to 20% according to the statistics provided in [68].

The widely used mammography breast-screening methodology uses ionized x-rays and is not capable of detecting the cancer in dense breasts, resulting in more diagnosis and exposure to the ionized rays. The excessive diagnosis on women in some cases resulted

in severe casualties and complexities in detecting the tumour involving the reduction of the dense breast and other painful methods as indicated in [69–71]. Consecutively MWI has emerged as a promising alternative to conventional ionized rays based imaging technologies, differentiating healthy and malignant tissues based on the difference in their dielectric properties. Researchers have developed various MWI methodologies for breast screening as presented in [72, 73] showing the promising nature of the UWB by doing measurements in the frequency domain. Some of the proposed techniques and MWI prototypes have reached clinical trials stage, such as those in [74] and [75] differentiating healthy and malignant tissues based on dielectric properties in frequency and time domain, respectively.



Figure 4.1: Initial MammoWave prototype [75].

Based on MWI, a recent novel, fast, and accurate prototype named MammoWave (developed by UBT Srl, Italy) was introduced in 2015, where the experimentation was performed on the fabricated phantoms as presented in [12]. The initial prototype of MammoWave, shown in Figure. 4.1 was installed in the department of diagnostic imaging, Perugia, Italy. The device includes a cup known as the breast holder, whereas the patient lies prone on the examination table, and examination is performed. This initial prototype contains two vertically polarized UWB antennas transmitting and receiving antenna emitting radiations in the azimuth plane in omnidirectional inside the cylindrical hub with microwave absorbers. The prototype has the operating frequency range of 1-9 GHz, and antennas are connected to the VNA by Copper Mountain Technologies. After phantom validations, in [30], the prototype was tested on 22 healthy breasts and 29 breasts having lesions, and the performance of the device was successfully validated by accurate results generated in [12, 30].

The current MammoWave prototype presented in [76,77] is shown in Figure 4.2. MammoWave is uniquely skilled to work with two antennas spinning in the azimuth plane, operating within the microwave band. The device has a cylindrical hub made of aluminium with a radius of 50 cm and is equipped with internal microwave absorbers, specifically flat absorbers AH model, SIEPEL CyBer, France [76].



Figure 4.2: Current MammoWave prototype [77].

The device consists of two antennas, namely the Tx (transmitter) and Rx (receiver), operating in the frequency range of 1 to 6.5 GHz. These antennas rotate in a circular direction in the azimuth plane within a free space environment. The rotation of the antennas is automated and can be configured and adjusted using a GUI developed by UBT Srl, Italy. This GUI enables users to control the antenna's height and execute specific configurations to record measurements.

Moreover, the device includes a mini anechoic chamber located inside the cylindrical hub, along with a holder designed for breasts, allowing patients to lie in prone position during examinations, or for positioning fabricated phantoms. Both antennas surround the holder within the cylindrical hub and rotate around it to capture the necessary measurements.

The UWB antennas utilized in the device are Vivaldi antennas, and they are connected to a two-port VNA model M5065 by Copper Mountain Technologies, USA, as shown in Figure 4.3. The VNA, depicted in Figure 4.4, has two configurable ports, with port 1 acting as the transmitter and port 2 as the receiver. The M5065 VNA incorporates a



Figure 4.3: MammoWave installed at London South Bank University.

radiofrequency measurement module and an operating software developed by the manufacturers. This software can be easily installed on any Windows or Linux operating systems and is connected via a standard USB port. The VNA has a frequency range of 300 kHz to 6.5 GHz and can measure all four parameters, namely S11, S12, S21, and S22. It comes with a calibration kit, which ensures that the antennas are calibrated for optimal performance. Additionally, the VNA boasts a rapid measurement speed of 70 μ s, making it highly efficient for MammoWave data collection and analysis.



Figure 4.4: 2-port VNA (M5065).

One significant advantage of using this VNA is its user-friendly software interface, which simplifies operation and integration. Additionally, the VNA software allows for automatic data saving, eliminating the need for manual recording of measurements. This automated feature streamlines the entire measurement process, distinguishing it from the setup used in the anechoic chamber described in the previous chapter.

4.3 Imaging Algorithm

The capability of MammoWave allows for different configurations to be executed by programming the device accordingly. In the measurement configuration, both antennas are the same and are attached to a two-port VNA (M5065, Copper Mountains, USA) operating at a frequency range of 1-6.5 GHz [78]. Both antennas are rotatable, covering a full 360°. The Tx plane is divided into 5 angular sections with an angular difference of 72°, corresponding to transmitting signals from the 5 central points (0°, 72°, 144°, 216°, 288°).

Additionally, for each triplet of central points, the Tx antenna transmits signals from two other angularly displaced positions, $\pm 4.5^\circ$ rotation with respect to the central points, resulting in a total of 15 transmitting positions. The receiver antenna can receive signals at intervals of 4.5°, leading to 80 receiving points. A pictorial view of this configuration is depicted in Figure 4.5 [79].

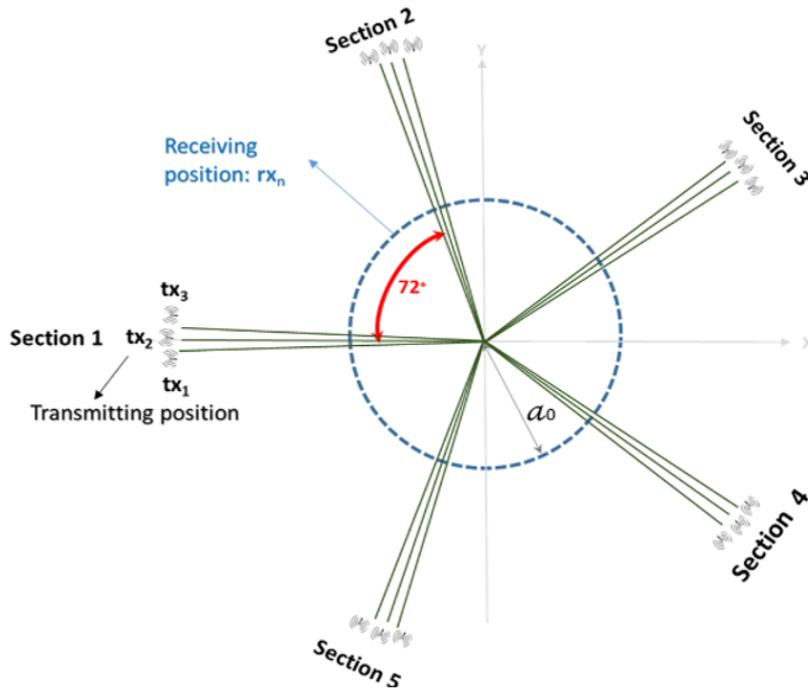


Figure 4.5: Experimental Configuration.

In this configuration, for one central transmitting position, two adjacent transmitting positions have been used with an angular displacement of $\pm 4.5^\circ$. The received complex signal S_{21} can be presented as $S_{21}^{m,p}(a_0, \phi_n; Tx_{m,p}; f)$, where $n = 1, 2, \dots, 80$ indicates the receiving points; $m = 1, 2, \dots, 5$ specifies the central transmitting positions, $p = 1, 2, 3$

indicates the positions inside transmitting sections in the form of triplets, and f is the frequency. Therefore, applying HP, the external field carrying information of the dielectric contrast can be presented the same as:

$$E_{HP,2D}^{rcstr}(\rho, \phi; Tx_{(m,p=1,2,3)}; f) = \sum_{n=1}^{NPT} E_{i_n, Tx_{m,p=1,2,3}}^{known} G(k_1|\rho_{np} - \rho|). \quad (4.1)$$

Meanwhile the intensity of the consistent image can be obtained by summing all the solutions incoherently as:

$$I_{2D}(\rho, \phi; Tx_{(m,p=1,2,3)}) = \sum_{f=1}^{NF} |E_{HP,2D}^{rcstr}(\rho, \phi; Tx_{(m,p=1,2,3)}; f_i)|^2. \quad (4.2)$$

An artifact can be removed by subtracting between S_{21} obtained using two measurements at different positions in the triplet, such as $p = 1, 2, 3$ and $p' = 1, 2, 3$, with $p \neq p'$. This methodology is more efficient in terms of artifact removal as the basic methodology of artifact removal through rotation subtraction can be successfully achieved on both sides of the central transmitting positions.

$$E_{HP,2D}^{rcstr}(\rho, \phi; Tx_{m,p} - Tx_{m,p,h'}; f) = \sum_{n=1}^{NPT} (S21_{np}^{m,p} - S21_{np}^{m,p'}) G(k_1|\rho_{np} - \rho|). \quad (4.3)$$

4.4 MammoWave Validation

MammoWave is based on the HP-based MWI methodology, which has been thoroughly researched and validated in various experiments on objects with canonical and cylindrical shapes, with single and multiple inclusions [41–43]. The methodology has been verified through different image quantification parameters, such as SCR, resolution, and HP phase weighted modality, and its capabilities have been tested on various scenarios, including skin mimicking phantoms, brain stroke detection, and bone lesion detection [80]. MammoWave has successfully undergone initial clinical trials authorized by the Italian Ministry of Health and the Ethical Committee of Regione Umbria, Italy, at Perugia Hospital, yielding promising results [12, 30, 81]. The device has the potential to revolutionize breast screening, as it can be used without age restrictions or health risks, and without involving breast compression or liquid, making it a more comfortable experience for patients. It has completed multicentric trials in several hospitals, including Humanitas

Milano, San Martino Genova, and Toledo Hospital in Spain, and is extending its reach to other countries under the MammoScreen project [82,83].

The UBT team and researchers are continuously working on further advancements in the MammoWave prototype, performing various experiments to test its capabilities. A recent experiment using a multi-layered phantom mimicking bone properties successfully localized bone lesions with a SCR of 3.35 dB and a resolution of 5 mm [84,85]. Another prototype called StrokeWave is being developed for brain stroke and cancer detection using the HP-based MWI algorithm and has shown promising results in preliminary trials [86]. Additionally, the MammoWave has been tested on a miniature lung phantom for lung COVID-19 infection detection, and the results have been compared with the experiments described in Chapter 3 [61]. These advancements and successful trials showcase the potential of the MammoWave and HP-based MWI technology in the field of medical imaging and early disease detection.

4.5 Lung Lesion Detection via MammoWave (Preliminary Results)

Lung damage is a pervasive respiratory disease that can manifest in the form of lung lesions, including lung cancer, tumours, or lung infections. Early detection of lung lesions is crucial for preventing further damage, controlling the spread of lung infections, and reducing the mortality rate of pulmonary patients. Currently, CT scans and X-ray imaging are reliable methods for detecting lung lesions and monitoring treatment progress. However, the use of ionizing radiation in these techniques raises concerns about potential health risks [87,88]. In this experiment, a miniaturized torso phantom was fabricated to conduct phantom experiments using the MammoWave device, exploring different scenarios.

The images are obtained using the HP-imaging procedure, and an artefact removal method named “rotation subtraction” was applied, involving two slightly displaced transmitting positions. Additionally, an “ideal” artefact removal method is employed, which subtracted the received data from the unhealthy torso phantom from the data of the healthy torso phantom [61].

4.5.1 Phantom Fabrication and Experimental Configuration

. A miniaturized model of the torso phantom was constructed for the measurements using the MammoWave device, as depicted in Figure 4.6. The external layer of the phantom has dimensions with axes of 12 cm and 6 cm, and a height of 17 cm, while the internal layer has axes of 9.5 cm and 3.5 cm, and a height of 16 cm. The phantom was made using tissue-mimicking materials to simulate the characteristics of human tissues. To replicate a combination of fat, muscle, and rib bones tissues, a specific type of oil named TLe11.5C.045 was used. This oil has a dielectric constant value of 7 and a conductivity value of 0.3 S/m, and it was provided by ZMT Zurich MedTech Company [53]. For mimicking the lung layer, a mixture containing 90% glycerol and 15% water was used, resulting in a dielectric constant of 15 and a conductivity of 2 S/m (at 2 GHz) [52]. To simulate lung lesions, tap water was employed, following a similar approach as done in [49]. These tissue-mimicking materials allowed for accurate representation of the human torso and enabled the MammoWave device to perform measurements effectively.

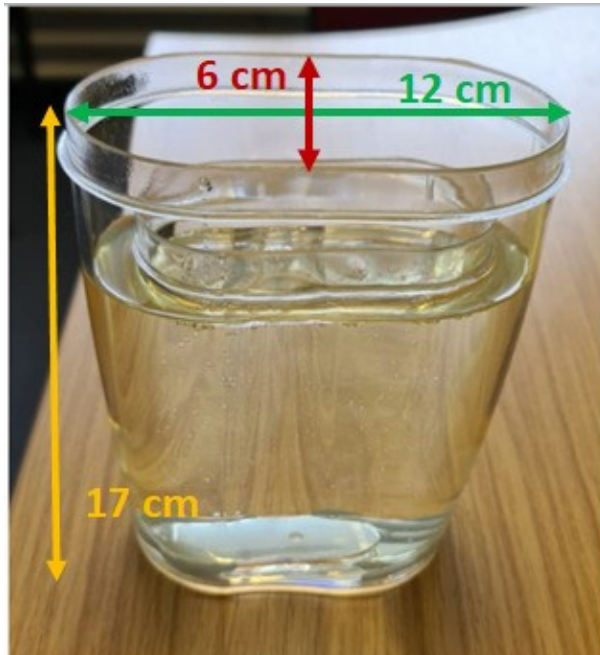


Figure 4.6: Fabricated Multilayered Phantom [61].

The imaging algorithm strategy employed is the same as described earlier in this chapter, following the experimental Configuration with a total of 15 transmitting positions arranged in the form of triplets. By applying the HP-based imaging algorithm, the external field can be measured as given by Eq. (4.1), with all the parameters defined in the previous section.

Furthermore, to obtain a consistent image, all the solutions can be reconstructed by summing them incoherently, as demonstrated in Eq. (4.2). However, even after applying artefact removal procedures, some clutter may still be present in the resulting images. To assess the capabilities of image detection and to compare the performance of various artefact removal methods, the SCR has been utilized, as defined by the ratio between the maximum intensity within the region of the lesion and the maximum intensity outside the region of the lesion. This SCR metric was introduced in [89] for quantitative evaluation of the imaging capabilities and to provide a measure of the image quality.

4.5.2 Reconstructed Images

The primary goal of this research is to investigate the potential of HP imaging in the context of elliptical, asymmetric, and multi-layer torso-mimicking phantoms. Additionally, the study aims to compare and evaluate the effectiveness of two artefact removal methods, namely “rotation subtraction” and “ideal” artefact removal, in suppressing artefacts and achieving successful lung lesion detection. This approach differs from the average subtraction method employed in [41]

To assess the performance of these artefact removal methods in lung lesion detection, both within the anechoic chamber and using the MammoWave device, SCR metric is used. The computed SCR values are summarized in Table 4.1. To achieve this objective, Table 4.1: SCR for microwave images of phantom measurements in both the anechoic chamber (chapter 3) and MammoWave device.

Artefact Removal Method	Anechoic Chamber SCR (dB)	MammoWave Device SCR (dB)
Rotation Subtraction	4.65	7
Ideal Artefact Removal	6	9.88

phantom experiments were conducted both inside an anechoic chamber (as described in chapter 3) and using the MammoWave device. Microwave images were generated employing both ideal and rotation subtraction artefact removal techniques. The obtained microwave images, as shown in Figures 4.7 and 4.8, were normalized to their corresponding maximum values, and intensity values below 0.5 were set to zero. However, the calculation of the SCR was performed prior to image adjustment. In these images, the green elliptical region indicates the area of the torso phantom, while the lung lesion area is highlighted by a red circle (as described in chapter 3).

Figures 4.7 (a) and (b) display the microwave images obtained from anechoic chamber phantom experiments. Figure 4.7 (a) shows the microwave image after applying the “rotation subtraction” method, which involves subtracting the obtained S21 of transmitting position 0° from transmitting position 5° . Despite some clutter in the image, successful detection has been achieved with an SCR value of 4.65 dB. Figure 4.7 (b) illustrates the microwave image after applying the “ideal” method. As shown in Figure 4.7 (b), the inclusion (lung lesion) has been visually detected in the right position with reduced clutter, achieving an SCR value of 7 dB.

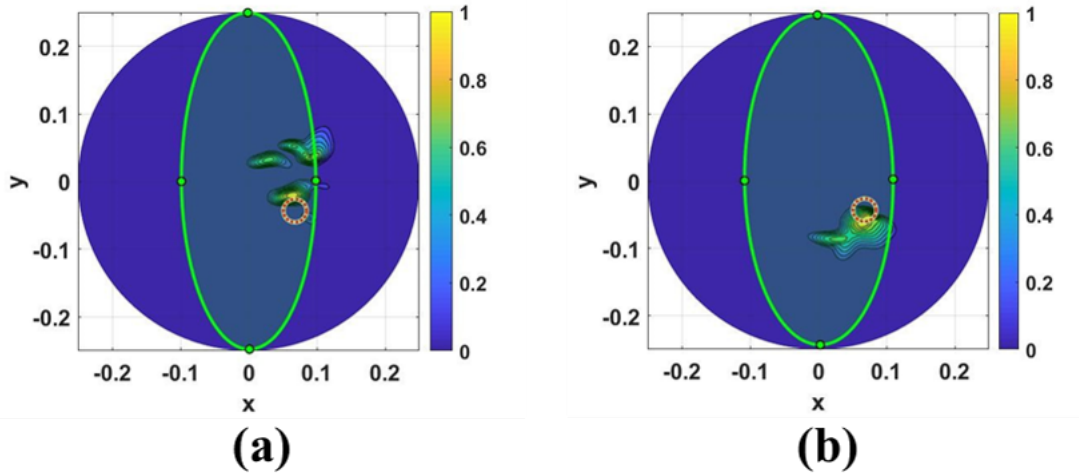


Figure 4.7: Obtained microwave images of anechoic chamber phantom experiments using frequency 1 GHz to 5 GHz, (a) applying “rotation subtraction” method, (b) employing the “ideal” method. The light green ellipse indicates the phantom region, while the area marked with a red circle shows the exact position of inclusion and the dimension of the circle is in relation to the dimension of the inclusion. Axes scales are meters.

Now, shifting the focus to the MammoWave device, the microwave images obtained from the miniaturized lung lesion phantom experiments are presented in Figures 4.8 (a) and (b). Figure 4.8 (a) shows the microwave image of the lung phantom obtained through the rotation subtraction artefact removal procedure. As evident from Figure 4.8 (a), the detection of the lung lesion has been successfully achieved in its correct position, with an SCR value of 6 dB. Figure 4.8 (b) illustrates the result of applying the “ideal” artefact removal procedure. In this case, the inclusion (lung lesion) is visible with even less residual clutter, and the detection has been accomplished effectively, with an SCR value of 9.88 dB.

In both the anechoic chamber and the MammoWave experiments, the highest SCR values were achieved when applying the “ideal” artefact removal method, with SCR values of

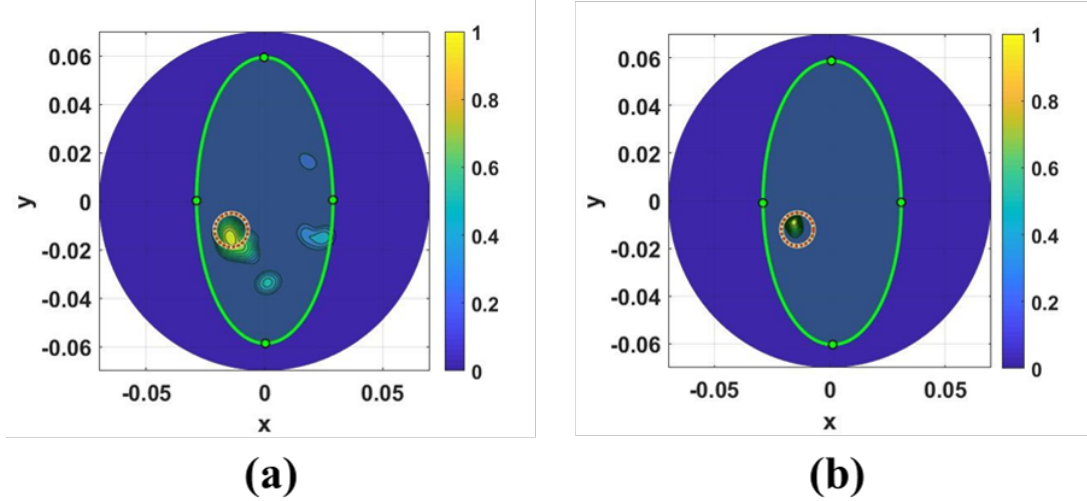


Figure 4.8: Obtained microwave images of MammoWave device phantom experiments using frequency 1 GHz to 6.5 GHz, (a) applying “rotation subtraction” method, (b) employing the “ideal” method. The light green ellipse indicates the phantom region, while the area marked with a red circle shows the exact position of inclusion and the dimension of the circle is in relation to the dimension of the inclusion. Axes scales are meters.

7 dB and 9.88 dB, respectively. The higher SCR value obtained with the MammoWave device could be attributed to the fact that it employs more transmitting positions, providing more comprehensive data for the imaging process. To further investigate the lung lesion detection capability using the proposed method, a more realistic and complex scenario was considered. The measurement was repeated using a re-miniaturized torso phantom that contained two cylindrical inclusions filled with tap water to mimic lung lesions. The two cylindrical inclusions had different radii, 0.7 cm and 0.25 cm, respectively. The re-miniaturized torso phantom had external layer dimensions of 10 cm \times 5.5 cm \times 15 cm and internal layer dimensions of 9 cm \times 4.5 cm \times 14 cm, using the same tissue-mimicking materials as the previous phantom. Figures 4.9 (a) and (b) show the fabricated re-miniaturized torso phantom and its position inside the MammoWave device, respectively. Additionally, Figure 4.9 (c) displays the S21 values for both the phantom with and without the inclusions, calculated when the transmitting antenna is Tx1 and the receiving antenna is 180° apart.

Finally, Figures 4.10 (a) and (b) depict the obtained microwave images using the MammoWave device with the re-miniaturized torso phantom, employing the “rotation subtraction” and “ideal” artefact removal methods, respectively. The results confirm that lung lesion detection can be successfully achieved even in more complex scenarios, such as a phantom containing two inclusions of varying sizes. Figure 4.10 (a) reveals

some clutter in the obtained image; however, both inclusions can be clearly observed in their approximate positions, with an SCR value of 5.2 dB. Shifting to Figure 4.10 (b), the detection of both inclusions was completed with greater clarity and less clutter, resulting in an improved SCR value of 6.19 dB. These findings demonstrate the potential of the proposed HP imaging method for detecting lung lesions even in scenarios involving multiple inclusions of different sizes.

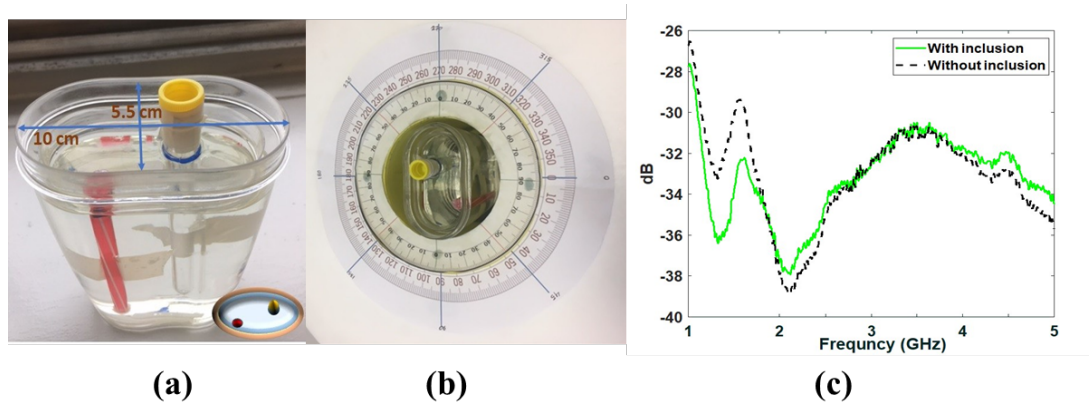


Figure 4.9: (a) Depict the fabricated re-miniaturized torso phantom, the position of the torso phantom inside the MammoWave device, (b) the S21 for both the phantom with and without inclusions, (c) calculated when the transmitting antenna is Tx1 and the receiving antenna is 180° apart, respectively.

One limitation of this study is that the constructed phantoms do not fully represent the heterogeneity of the human torso. For instance, the phantoms did not account for the alternate distribution of ribs and muscle, which were instead mimicked using a dedicated layer with average dielectric properties. This simplified representation of the human torso might result in a potential reduction of SCR. To address this limitation and gain a more comprehensive understanding of the HP imaging method's performance in real-world scenarios, dedicated clinical trials are planned as the next step. These trials will involve actual patients and will consider the full heterogeneity of the human torso. By conducting these clinical trials, the potential impact of the heterogeneity on SCR values and the overall effectiveness of the imaging method will be thoroughly assessed.

4.6 Summary

In this chapter, the validation of an HP-based MWI procedure for detecting lung lesions in phantoms was performed using the MammoWave device. Initially, lung lesion detection

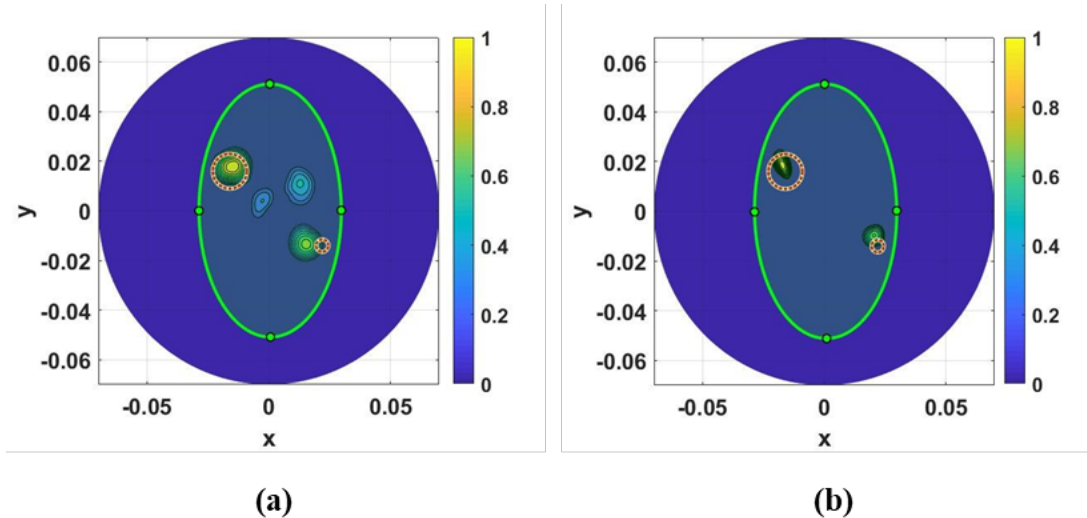


Figure 4.10: Reconstructed images of the lung phantom with two inclusions. (a, b) represent the images corresponding to applying the “rotation subtraction” artefact removal method and “ideal” artefact removal method, respectively. The light green ellipse indicates the phantom region, while the areas marked with red circles show the exact positions of the inclusions and the dimension of each circle is in relation to the dimension of the inclusion. Axes’ scales are meters.

was achieved through performing measurements on a dedicated multi-layer oval-shaped torso phantom using an anechoic chamber setup with two antennas operating in the 1 to 5 GHz frequency range, as briefly described in chapter 3. Subsequently, a miniaturized torso phantom investigation was conducted using the MammoWave device, exploring different scenarios involving torso phantoms with two different sizes of cylindrical inclusions to mimic lung lesions. Precisely, the experiments performed in the previous chapter (Chapter 3, Sections 3.4 and 3.5) with fabricated lung phantoms with more complexities and results generated shows the capability of the MWI in lung lesion detection. In this chapter, the capability of the MammoWave has been tested via fabricating a miniature (in dimensions) multi-layered lung phantom with the same dielectric properties as in chapter 3 section 3.4. Rather than manual approach to conduct the experiments as described in previous chapter, the MammoWave automated the whole measurement procedure making it more reliable in terms of accuracy.

To ensure accurate detection and avoid masking the region of inclusion caused by potential artefacts, two distinct artefact removal methods were applied before reconstructing the images. Both artefact removal procedures demonstrated the capability to achieve lung lesion identification, with an SCR of 9.88 dB achieved using the “ideal” artefact removal method with the MammoWave device.

Future steps in this research involve constructing a dedicated MWI device, a modified version of the MammoWave, specifically designed for lung imaging clinical trials. This device would facilitate monitoring of lung lesions without the use of X-Rays, making it safe and advantageous for pre-hospital examinations. The device's portability and low structural complexity offer additional benefits. The output power of the VNA used in these experiments (1 mW) currently poses no concerns about SAR; however, in the event of increased output power, SAR would be appropriately monitored to ensure safety.

Chapter 5

3D Huygens Principle based Microwave Imaging through MammoWave Device.

5.1 Introduction

In the preceding chapter of this thesis, a detailed introduction is provided to the groundbreaking MWI device named MammoWave. This research explains the device's swift and accurate capabilities, shedding light on its potential applications in the field of medical diagnostics. A comprehensive overview of the device's features and a meticulous characterization of its measurement procedures is also presented to establish a solid foundation for its subsequent applications. In the preceding chapter, the successful clinical trials of the device and its impressive capability in breast cancer screening are also being explored. The report documents the positive outcomes of these trials, showcasing MammoWave's efficacy and reliability in identifying potential breast cancer cases. Additionally, the report details the research efforts aimed at further advancing the MammoWave technology beyond the clinical trials. One notable aspect of this research involves conducting experiments on fabricated phantoms. These phantom models provide a controlled and reproducible environment for studying the device's behaviour under various conditions, enabling to fine-tune its capabilities. Notably, one experiment involved testing the MammoWave device on a miniature multi-layered lung phantom specifically designed to mimic the complexities of human lung tissue. The phantom featured fabricated inclusions and

layers with mixtures having varied dielectric properties, which are crucial factors in lung cancer detection. The results of this experiment were promising and encouraging. The reconstructed images resulting from the MWI measurements exhibited great potential for detecting abnormalities within the lung tissue.

This Chapter focuses on developing a 3D MWI algorithm based on HP. Specifically, MammoWave MWI device has been exploited for its capabilities of extending image reconstruction from 2D to 3D. For this purpose, dedicated phantoms containing 3D structured inclusion are prepared with mixtures having different dielectric properties. Phantom measurements are performed at multiple planes along the z-axis by simultaneously changing the transmitter and receiver antenna height via the GUI integrated with MammoWave. The complex S21 multi-quote data is recorded at multiple planes along the z-axis. The complex multidimensional raw data is processed via an enhanced HP based image algorithm for 3D image reconstruction. This Chapter demonstrates the successful detection and 3D visualization of the inclusion with varying dimensions at multiple planes/cross-sections along the z-axis with a dimensional error lower than 7.5%. Moreover, the Chapter shows successful detection and 3D visualization of the inclusion in a skull-mimicking phantom having a cylindrically shaped inclusion, with the location of the detected inclusion in agreement with the experimental setup. Additionally, the localization of a 3D structured spherical inclusion has been shown in a more complex scenario using a 3-layer cylindrically shaped phantom, along with the corresponding 3D image reconstruction and visualization.

5.2 Background of Proposed Research

Medical imaging is a widely acclaimed technique that allows to visualize the inner workings of the human body and plays a pivotal role in distinguishing between healthy and diseased tissues. In the field of medicine, there exists an array of imaging techniques employed for treatment and diagnostics purposes, including X-rays, ultrasound, CT, and positron emission tomography (PET). While these methods have been instrumental in medical practice, they come with certain drawbacks such as high costs, demanding maintenance, and cumbersome instruments that are challenging to reposition. Additionally, some techniques involve the use of ionized rays, which can potentially pose health risks [90,91]. This

has led to a growing interest in the development of fast, innovative, and risk-free imaging technologies for diagnostic applications. The short duration of the pulses enables them to operate within the permissible noise levels, endowing UWB with high gain, speed, and precision. Remarkably, UWB impulses can effortlessly penetrate through objects, making it an outstanding candidate for medical imaging [92, 93].

In the past decades, extensive research has been conducted in the realm of microwave imaging, leading to the introduction and evolution of several imaging algorithms, particularly in the field of breast lesion detection. These MWI algorithms are based on radar techniques in the time domain and utilize real-time filters to compensate for fractional time delays. Alternatively, microwave tomography techniques can be employed, but they may suffer from drawbacks such as low signal-to-clutter ratios and complex mathematical formulations [94]. More recently, the focus of research has shifted towards developing novel methodologies and advancing existing algorithms for 3-dimensional (3D) imaging. The incorporation of 3D medical imaging proves immensely useful for diagnostic purposes, allowing for the accurate detection of the dimensions of diseased areas and lesions. Noteworthy prototypes and methodologies for 3D MWI can be found in [95–98], particularly concerning breast lesion detection. Furthermore, a comprehensive prototype for 3D microwave brain stroke imaging has been presented in [99], showcasing validated experimental results on fabricated phantoms. These advancements in medical imaging technology hold immense promise in revolutionizing the way to approach diagnostics and treatment, ultimately contributing to better patient care and improved health outcomes.

In addition to these prototypes, MammoWave, developed by UBT Srl in Italy, has been introduced for breast lesion detection. What sets MammoWave apart is its unique ability to work with two antennas spinning in the azimuth plane, operating within the microwave band.

MammoWave employs a HP-based imaging algorithm, initially introduced in [41]. This imaging algorithm significantly reduces the computational burden as it eliminates the need to solve the inverse problem and perform matrix generation or inversion, making it an ideal technique for medical microwave imaging. The methodology adeptly gathers all information from individual frequencies in the frequency domain to reconstruct a consistent image [41]. Clinically, MammoWave's capability in breast lesion detection has been successfully verified [77]. Moreover, the device has been adapted to perform

phantom imaging for brain stroke and bone lesion detection [85, 100]. All MammoWave images are thoroughly evaluated in 2D and at a single plane along the z-axis after the removal of artefacts [101].

The research in this chapter focuses on exploiting the MammoWave device shown in Figure. 5.1(a) to extend the imaging algorithm from 2D to 3D by conducting a multi-plane scanning experiment. To accomplish this, a cylindrical fabricated phantom with a 3D structured tube as an inclusion, mimicking a lesion, has been employed for experimentation. Measurements have been acquired in multiple planes along the z-axis. By implementing a modified HP-based algorithm via the superimposition theorem, the inclusion has been successfully detected in various planes. To enable 3D visualization and ascertain the dimensions of the inclusion at multiple planes, image processing and adjustment have been applied to the reconstructed images.

Furthermore, this chapter seeks to evaluate the proposed 3D imaging algorithm's capability in a more realistic scenario by repeating the measurements using a skull-mimicking phantom with an inclusion. In contrast to a previous study [102], which presented preliminary results without quantification, the present research quantifies and validates 3D imaging performances by calculating SCR and dimensional error. Additionally, performance degradation under modified imaging parameters has been quantified, with measurements performed using a 3D skull-shaped head phantom. Finally, a comprehensive localization error quantification has been included in the research.

This Chapter showcases the significant advancement achieved by incorporating the MammoWave device and the HP-based imaging algorithm in the realm of medical imaging. The extension to 3D imaging opens up new possibilities for improved accuracy and visualization, particularly in diagnosing and understanding breast lesions and other medical conditions.

5.3 Experimental Configuration

5.3.1 Device and Methodology

In this Chapter, the acquisition of all results and images has been facilitated by leveraging the unique capabilities of the MammoWave device. With the well-defined frequency range and the circular rotation of antennas, the MammoWave device can effectively penetrate

and scan the target area, providing valuable insights into the internal structures and characteristics of the subjects under examination.

In this research, both the transmitter (Tx) and receiver (Rx) antennas of the MammoWave device are designed to provide complete coverage of 360° . The Tx plane is divided into 5 angular sections, each separated by 72° . This means that the device transmits signals from 5 central points located at 0° , 72° , 144° , 216° , and 288° . However, the transmission process is not limited to just these central points. For each triplet of central points, the Tx antenna also transmits signals from two additional angularly displaced positions, rotated by $\pm 4.5^\circ$ with respect to the central points. This results in a total of 15 transmitting positions. On the other hand, the receiver antenna is configured to receive signals every 4.5° . This setup provides a total of 80 receiving points for capturing the transmitted signals accurately and comprehensively [12].

By utilizing this precise and well-coordinated rotation and transmission scheme, MammoWave device captures a vast amount of data points, facilitating high-resolution imaging across the entire region of interest. The strategic arrangement of transmitting and receiving points ensures optimal coverage and minimizes any potential data gaps, leading to reliable and detailed 3D imaging results.

Additionally, the MammoWave device includes a cylindrically shaped phantom holder, where both Tx and Rx antennas rotate in a circular direction around the phantom holder. Previous studies [12,77,85,100] utilizing the device have taken measurements solely in one plane along the z-axis, resulting in 2D imaging results. However, this research introduces a novel and groundbreaking methodology for applying MWI at different planes or heights along the z-axis, thus enabling 3D imaging capabilities.

The research employs the superimposition theorem on measurements taken at various planes adjacent to the z-axis. The process involves selecting one reference plane and subsequently moving downwards along the z-axis with equal distances between each successive pair of planes. This innovative experimental methodology is depicted in Figure 5.1(b). By capturing measurements at different planes, the research enables the reconstruction of a comprehensive 3D image, providing valuable insights into the internal structures and dimensions of the subjects under examination.

To facilitate this methodology, a GUI designed to operate the MammoWave device efficiently has been used. The GUI allows for the simultaneous and synchronized ad-

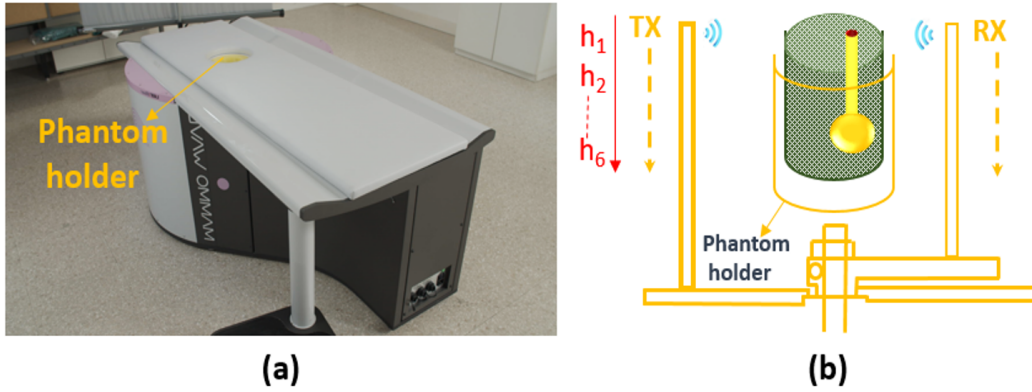


Figure 5.1: (a) MammoWave microwave imaging device having a cylindrical hub and the phantom holder, (b) experimental schematic i.e., fabricated phantom inside phantom holder with changing heights of antennas for multiple cross-sectional analysis along the z-axis.

justment of the height of both antennas (Tx and Rx). By maintaining the antennas at the same height throughout the process, changes in height are conducted simultaneously for both Tx and Rx antennas, ensuring accurate and consistent data acquisition. This pioneering research marks a significant advancement in the field of medical microwave imaging, unlocking the potential for precise and detailed 3D visualization of internal organs and tissues. The ability to capture data at multiple planes along the z-axis empowers medical professionals with a deeper understanding of anatomical structures and disease progression, ultimately enhancing diagnostic accuracy and patient care.

5.3.2 Phantoms Fabrications

In the research, a cylindrical plastic container was utilized as a phantom, featuring a diameter of 11 cm and a height of 13 cm. For the first measurement, a 3D-shaped tube with a spherical bottom was employed as the inclusion within the phantom. The tube exhibits a diameter of 1 cm at its upper part, which extends for a length of 7.5 cm. As it progresses downwards, the diameter of the tube gradually increases to 3.5 cm at its lower part, as illustrated in Figure 5.2(b).

The incorporation of a 3D structured inclusion serves a specific purpose in the research. Its main objective is to validate the 3D imaging algorithm by enabling the detection and visualization of the inclusion's dimensions at multiple planes along the z-axis. By scanning the inclusion at various heights, the reconstructed images can verify the algorithm's accuracy in reconstructing the complete 3D shape of the inclusion. This process allows for the assessment of the algorithm's performance and its capability to precisely capture

the size and shape of the inclusion from different perspectives. This experimental setup with the 3D-shaped inclusion in the cylindrical phantom adds a critical dimension to the research, as it paves the way for reliable and robust 3D medical microwave imaging techniques.

The primary concept behind MWI revolves around utilizing the contrast in dielectric properties, specifically the relative permittivity and conductivity, between healthy tissues and tissues containing abnormalities, such as tumours or lesions. These dielectric properties affect the propagation of microwave signals through the different tissues, providing valuable information about their composition and internal structures. To create a suitable experimental setup for MWI, a cylindrical phantom made from TLe11.5c.045 oil, a material by ZMT Zürich MedTech, Switzerland was employed. This specific material exhibits desirable properties for mimicking human tissues, allowing for accurate simulation and analysis of microwave signal behavior in a controlled environment.

Table 5.1: Relative permittivity and conductivity of fabricated materials at 2 GHz [52, 101].

Fabrication Material	Relative Permittivity (ϵ_r)	Conductivity (σ) [S/m]
ZMT Zürich MedTech, Swiss, TLe11.5c.045 oil	7	0.3
40% glycerol and 60% water	60	2

For the inclusion, which serves as a representation of the lesion, a mixture of 40% glycerol and 60% water was used. This combination is selected to replicate the dielectric properties of tissues that might contain abnormalities or lesions. The introduction of this inclusion into the cylindrical phantom allows to assess how microwave signals interact with and are affected by the simulated lesion within the complex tissue environment. The utilization of these materials in the research is crucial in ensuring realistic and reliable results during the MWI experiments.

The materials used to fabricate the phantom and inclusion are prepared by considering dielectric property differences and the stability of the materials. The dielectric properties of both materials at a frequency of 2 GHz are presented in Table. 5.1 [52, 101].

To further validate the capability of the 3D imaging algorithm, a skull-mimicking phantom with specific dimensions of 7 cm \times 10 cm \times 15.5 cm was also fabricated. This phantom includes a cylindrically shaped tube serving as an inclusion, with a radius of 0.7

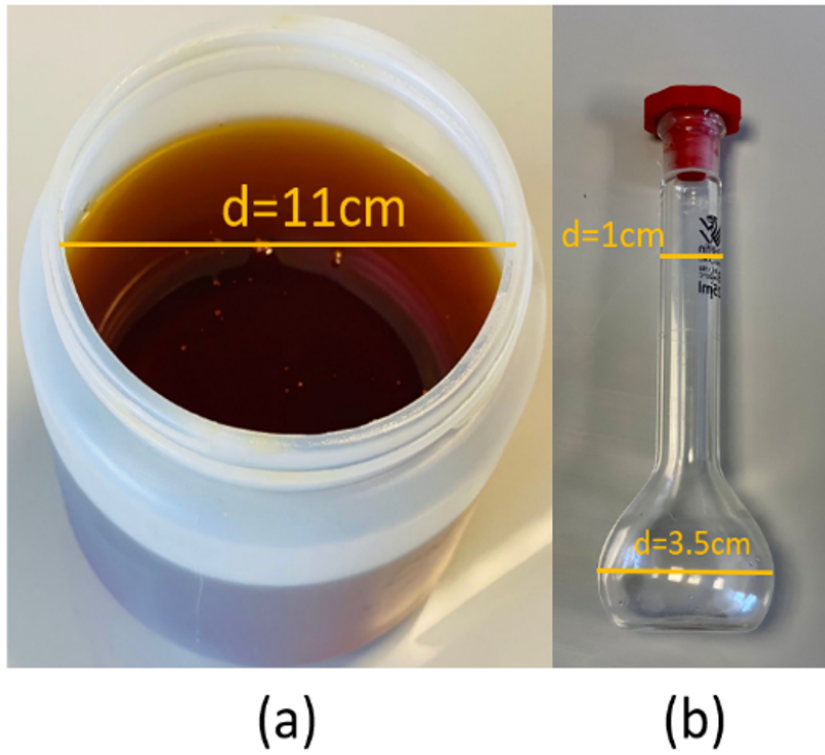


Figure 5.2: (a) Fabricated phantom, (b) 3D structured inclusion.



Figure 5.3: Fabricated head phantom.

cm, as illustrated in Figure 5.3. The skull-mimicking phantom was meticulously prepared by filling it with oil. Within the phantom, the bottom 1 cm of the cylindrical tube was filled with water, while the remaining part of the tube was filled with the same oil used in the construction of the skull. To achieve a realistic simulation of skull-like properties, oil with specific dielectric properties was utilised. The precise dielectric properties of the oil used in the skull-mimicking phantom can be found in reference [85]. These properties are essential for creating a phantom that closely replicates the dielectric behavior of human skull tissues, allowing for accurate simulation and evaluation of microwave signal interaction within the head-like structure. The performance and accuracy of the 3D imaging algorithm in detecting and reconstructing the inclusion inside the complex skull structure can be validated by employing this carefully designed skull-mimicking phantom.

In addition to the previous validation scenario, a more complex setup is considered to further validate the proposed 3D imaging algorithm. This extended scenario involves the addition of an internal cylindrical layer with a diameter of 7 cm to the initial experimental setup, as depicted in Figure 5.4. The internal cylindrical phantom has been positioned eccentrically within the primary setup, with an offset of 3.5 cm from the centre. This internal layer is filled with TLe5c24 liquid oil, which has dielectric properties of permittivity $\epsilon = 5$ and conductivity $\sigma = 0.2$. The choice of TLe5c24 liquid oil enables the creation of a distinct dielectric environment within the internal cylindrical layer, different from the surrounding materials in the primary phantom. Within this complex scenario, this experiment has used the same 3D structured spherical inclusion employed in the first experiment. However, for this specific scenario, only the spherical part of the inclusion, positioned inside the internal layer, has been filled with the fabrication mixture.

This advanced setup poses a more challenging and realistic scenario for the 3D imaging algorithm to demonstrate its efficacy. The algorithm's ability to handle complex variations in the dielectric environment can be assessed by incorporating the eccentrically positioned internal cylindrical layer with different dielectric properties. Additionally, the inclusion with its specific filling further adds to the complexity of the imaging task. The successful validation of the 3D imaging algorithm in this intricate scenario would reinforce its robustness and reliability, highlighting its potential for various medical imaging applications that involve complex internal structures and varying dielectric properties.

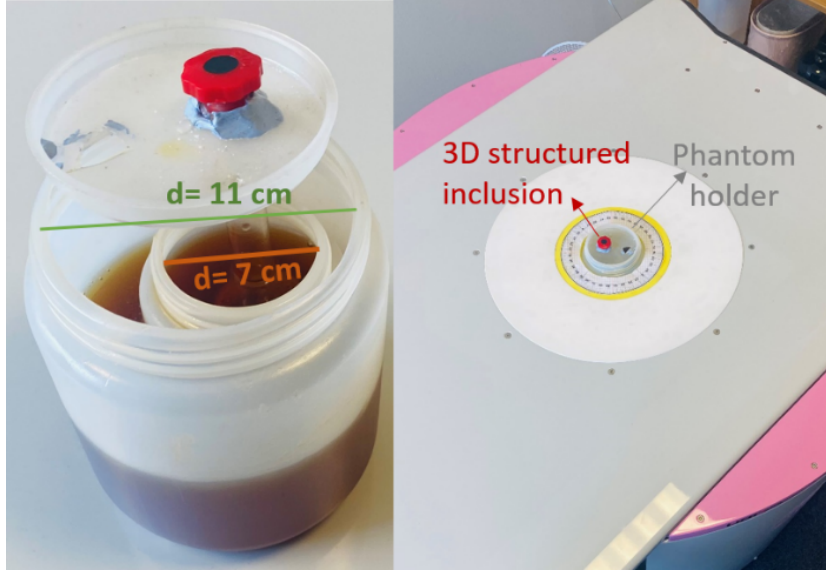


Figure 5.4: Fabricated 3-layer phantom (left) and the experimental setup (right).

5.3.3 Imaging Procedure

In the MammoWave system, both antennas have been programmed to rotate in an azimuth plane while operating in free space around the object of interest during experimentation. In this research, HP is applied to the measurements obtained at different planes along the z -axis. The ability to capture and preserve information from multiple perspectives is taken advantage of by the HP. By applying the HP to the measurements acquired at various heights, a consistent and accurate 3D image of the object under examination has been reconstructed.

The measurements are further processed to create images based on the differences in dielectric properties of the materials present in the experimental setup. These differences in dielectric properties mimic the contrast between tumour or abnormal tissues and healthy tissues. By leveraging the variation in dielectric properties, the 3D imaging algorithm can effectively distinguish between different types of tissues within the object. The successful application of the HP in this research demonstrates its effectiveness in producing high-quality 3D microwave images for medical imaging purposes.

Rx antenna can rotate $\pm 4.5^\circ$ to receive the transmitted signals at receiving points, which can be stated as $Rx_{n,h} \equiv (a_0, \phi_n, Z_h) \equiv (\vec{\rho}_{n,h})$ in the circular direction having radius a_0 at multiple planes alongside the z -axis. The received signal at multiple planes Z_h along the z -axis at different heights h can be represented as $S21$:

$$S21_{n,h}^{m,p}(a_0, \phi_n, Z_h; Tx_{m,p,h}; f) \quad (5.1)$$

where $n = 1, 2, \dots, 80$ indicates the receiving points; $m = 1, 2, \dots, 5$ specifies the central transmitting positions, $p = 1, 2, 3$ indicates the positions inside transmitting sections with the angular displacement of $\pm 4.5^\circ$, f is the frequency, Z_h represents the multiple planes along the z -axis, and $h = 1, 2, \dots, H$ is the number of heights along the z -axis (variable heights, i.e., H can be changed as per requirements). Figure. 5.5 shows the pictorial view of the measurement process with the phantom and inclusion.

The measured received signal $E_{iTx_{m,p,h}}^{known} |_{Rx_{n,p,h}} = E_{i_n, Tx_{m,p,h}}^{known}$ on multiple planes Z_h is then processed using HP to evaluate the field inside the cylinder. The measured external field carries the information of dielectric contrast of the mixtures inside the fabricated phantom for NPT observing points at multiple heights h_n , which can be represented as the reconstructed field:

$$E_{HP,3D}^{rcstr}(\rho, \phi, Z; Tx_{m,p,h}; f) = \sum_{h=1}^{h_n} \sum_{n=1}^{NPT} S21_{n,h}^{m,p}(a_0, \phi_n, Z_h; Tx_{m,p,h}; f) G(k_1 | \vec{\rho}_{n,h} - \vec{\rho} |) \quad (5.2)$$

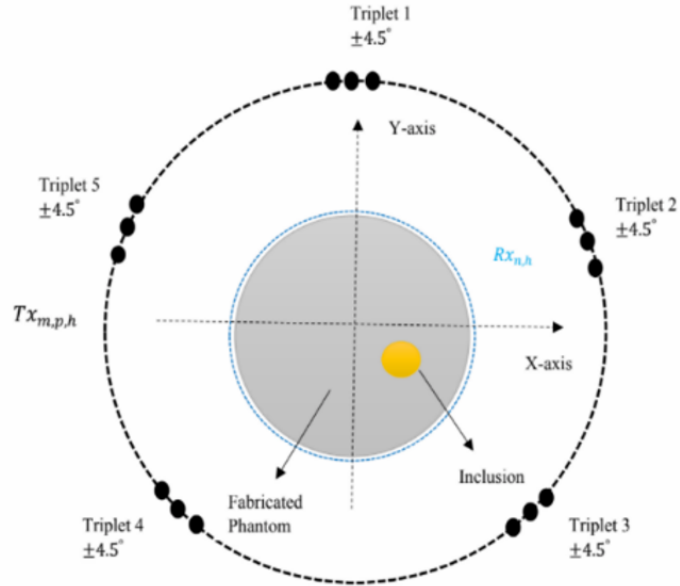


Figure 5.5: Pictorial view of the measurement process, where grey coloured circle represents the fabricated phantom, light blue dots indicate the receiving points, small yellow circle shows the inclusion. The outer dashed black circle shows the transmitting antenna perimeter with dark circles in sets of three showing the transmitter triplets.

In Eq. (5.2), 'rcstr' indicates the reconstructed internal field, 'HP' indicates the pro-

cedure used to measure the reconstructed field, and '3D' indicates the employment of the superimposition theorem for 3D visualization of the inclusion. Moreover, $\rho = (\rho, \phi, Z)$ and $\vec{\rho}_{n,h} = (a_0, \phi_n, Z_h)$ in Eq. (5.2) are the observation points at multiple planes Z_h . k_1 indicates the wavenumber, which is set here to be the free space dielectric constant.

$$G(k_1|\vec{\rho}_{n,h} - \vec{\rho}|) = \frac{1}{4\pi|\vec{\rho}_{n,h} - \vec{\rho}|} e^{-jk_1|\vec{\rho}_{n,h} - \vec{\rho}|} \quad (5.3)$$

Green's function G , as implemented in Eq. (5.3), has been used to propagate the field for multiple planes alongside the z -axis. Furthermore, the Green's function implies a singularity for $|\vec{\rho}_{n,h} - \vec{\rho}| = 0$; however, this singularity may be cancelled by multiplying the Green's function by $|\vec{\rho}_{n,h} - \vec{\rho}|$ as pointed out in [41]. $E_{HP,3D}^{rcstr}$ is calculated separately for Z_h and does not calculate the accurate field but rather captures the dielectric contrast between the inclusion and the surrounding material, enough for locating the target. It is essential to highlight that the evaluation of the internal field is not of interest; instead, the aim is to capture the contrast (mismatched boundaries) and locate the inclusion within the volume [41, 43].

Assume using N_F frequencies f_i in the frequency band B at multiple planes h_n , intensity I of the image can be obtained by incoherently summing all the solutions.

$$I_{3D}(\rho, \phi, Z; Tx_{m,p,h}) = \sum_{h=1}^{h_n} \sum_{i=1}^{N_F} |E_{HP}^{rcstr}(\rho, \phi, Z; Tx_{m,p,h}; f_i)|^2 \quad (5.4)$$

Artefacts can be removed by subtracting between S_{21} obtained using two measurements at different positions in the triplet such as $p = 1, 2, 3$ and $p' = 1, 2, 3$, with $p \neq p'$ for multiple planes as shown in Eq. (5.5). By implementing this artefact subtraction process for the measurements acquired at different positions within each triplet for multiple planes along the z -axis, the artefacts that may arise during the imaging process can be effectively reduced or eliminated. This step is essential for improving the accuracy and reliability of the 3D microwave imaging algorithm, ensuring that the final reconstructed images provide a clear representation of the internal structures and tissues without interference from artefacts.

The procedure used in this research is theoretically justified and draws inspiration from holography theory, which was originally developed by R. P. Porter and A. J. Devaney in the early 1980s [103, 104]. The proposed methodology is based on the concept that an

inverse source problem can be determined by analyzing the value of the field and its normal derivative over any closed surface surrounding the volume of interest. However, it is worth noting that while the works by Porter and Devaney [103,104] focus on recovering the map of dielectric properties in the volume and recognizing the contrast in dielectric properties, the approach proposed in this research addresses a simpler computational problem. Instead of recovering the complete map of dielectric properties, the proposed methodology aims to identify significant scatterers within the volume. To achieve this goal, only the field data obtained on an arbitrary closed surface surrounding the object of interest has been utilized.

$$E_{HP,3D}^{rcstr}(\rho, \phi, Z; Tx_{m,p,h} - Tx_{m,(p,h)'}; f) = \sum_{h=1}^{h_n} \sum_{n=1}^{NPT} \left(S21_{n,h}^{m,p}(a_0, \phi_n, Z_h; Tx_{m,p,h}; f) - S21_{n,h}^{m,p'}(a_0, \phi_n, Z_h; Tx_{m,(p,h)'}; f) \right) \quad (5.5)$$

The images of the sections are then summed up to get the final image at multiple heights along the z -axis as follows:

$$\begin{aligned} I_{3D}(\rho, \phi, Z) &= \sum_{h=1}^6 \sum_{m=1}^5 \sum_{p=1}^3 \sum_{p'=1, p' \neq p}^3 (I(\rho, \phi, Z; Tx_{m,p,h} - Tx_{m,(p,h)'}; f_i))^2 \\ &= \sum_{h=1}^6 \sum_{m=1}^5 \sum_{p=1}^3 \sum_{p'=1, p' \neq p}^3 \sum_{i=1}^{NF} (|E_{HP}^{rcstr}(\rho, \phi, Z; Tx_{m,p,h}; f_i)|)^2 \end{aligned} \quad (5.6)$$

The proposed HP-based imaging algorithm sets itself apart from the Kirchhoff migration algorithm, which typically involves back-propagation and time reversal to solve the inverse problems and find the phase or time traces [15]. In contrast, the HP-based algorithm in this research focuses on capturing dielectric contrast during the reconstruction process without explicitly finding the phase information. It performs a non-coherent summation in the frequency domain, allowing to gather information from individual frequencies, which is crucial for reconstructing a consistent image [41]. By leveraging the unique features of the HP-based algorithm, this methodology can achieve accurate and coherent imaging results that emphasize the contrast in dielectric properties between different tissues or structures. This approach provides valuable insights into the internal composition of the object under examination, making it particularly relevant for medical

microwave imaging applications. The HP-based 3D MWI algorithm is outlined below in the form of pseudocode, providing a concise overview of its key components and operations.

Algorithm 2 Huygens Principle 3D Imaging Algorithm

- 1: Load the recorded complex signals S21 via measurements.
 - 2: Initialize constants for free space parameters.
 - 3: Define source parameters:
 - 4: Specify observation 3D grid: $X_{\text{reconstr}}, Y_{\text{reconstr}}, Z_{\text{reconstr}}$.
 - 5: Set frequency parameters: `freq`, `new_freq_sample`.
 - 6: Applying Huygens principle based MWI algorithm (frequency domain):
 - 7: **for** $i = 1$ to $fmax$ **do** ▷ Loop over frequency samples
 - 8: **for** $Z_h = 1$ to 6 **do** ▷ Loop over observation points
 - 9: Compute scattered field contribution using Huygens principle.
 - 10: **for** $np = 1$ to 80 **do** ▷ Loop over observation points
 - 11: Compute scattered field contribution using Huygens principle.
 - 12: **end for**
 - 13: **end for**
 - 14: **end for**
 - 15: Accumulate incoherent summation in 3D
 - 16: **for** $i = 1$ to $\text{freq_samples} \times 1$ **do**
 - 17: Accumulate incoherent scattering contributions.
 - 18: **end for**
 - 19: Reconstructing images representing 3D visualisation.
-

5.4 Results and Discussions

In the experimental setup, a total of six measurements were performed for each phantom at multiple planes along the z-axis denoted as Z_h . For each measurement, 15 transmitting positions (organized in 5 triplets) and 80 receiving points are utilized in the frequency range of 1-6.5 GHz. This results in generating a raw data matrix of complex values for S21, with dimensions of 1200×1101 . To capture the measurement data, the antenna setup only considers the copolar component of the field, which, in this specific case, is vertically polarized. Although this component does not provide an exact reconstruction of the internal field, previous works [41] have demonstrated that it is sufficient for detecting mismatches and variations.

The measurement process for each plane takes approximately 9 minutes. Subsequently, the raw data is processed using the HP, which takes around 4-5 minutes to process the data from all planes simultaneously. This processing time corresponds to performing measurements with 80 receiving positions and a 5 MHz frequency sampling rate. However,

it is noted that the measurement time can be significantly reduced by decreasing the number of measurement points or increasing the frequency step. In previous works [41, 105], it has been demonstrated that the number of receiving points can be reduced to a spatial sampling of $\lambda/2$, where λ represents the wavelength in the phantom calculated at the maximum measured frequency. This leads to a reduction to 24 receiving points [41] without significantly affecting the SCR.

Similarly, frequency sampling can be increased to 20 MHz without compromising the detection and localization capabilities, as shown in the same research [41]. The previous works using a multilayer lousy gel phantom [25], which had properties similar to human tissues, indicate that such time reduction strategies are still effective in real scenarios for achieving accurate detection and localization. The implementation of these time-saving techniques allows for the efficient acquisition and processing of measurement data, making the overall imaging process more time-effective while maintaining a high level of accuracy in detecting and localizing targets of interest.

5.4.1 2-layer Phantom Results

In this work, the raw data collected from all six planes along the z-axis have been processed simultaneously and treated in the same coordinate system during the application of the superimposition theorem in the modified HP-based 3D imaging algorithm. The use of superimposition theorem allows to combine the information from multiple planes to reconstruct a comprehensive 3D image. The images obtained from the processed data for the first phantom (Figure 5.2) are presented in Figure 5.6, which demonstrates the detected inclusion at multiple planes along the z-axis. Measures have been taken to remove artefacts to ensure the accuracy of these images. One of the techniques used for artefact removal involves subtracting the S21 values at different positions with respect to the transmitting positions. Specifically, a 9° displacement has been employed in the images presented in this Chapter.

Improved image quality and fidelity, enhancing the ability to visualize and identify the inclusion accurately, are achieved by applying this artefact removal process at each plane. The resulting 3D images offer valuable insights into the internal structures and properties of the object under examination. The simultaneous processing of raw data from multiple planes and the artefact removal technique contribute to the effectiveness and reliability of

the proposed 3D imaging algorithm. This innovative approach holds significant promise for various medical imaging applications, where accurate and detailed 3D visualization of internal structures is crucial for diagnosis and treatment planning.

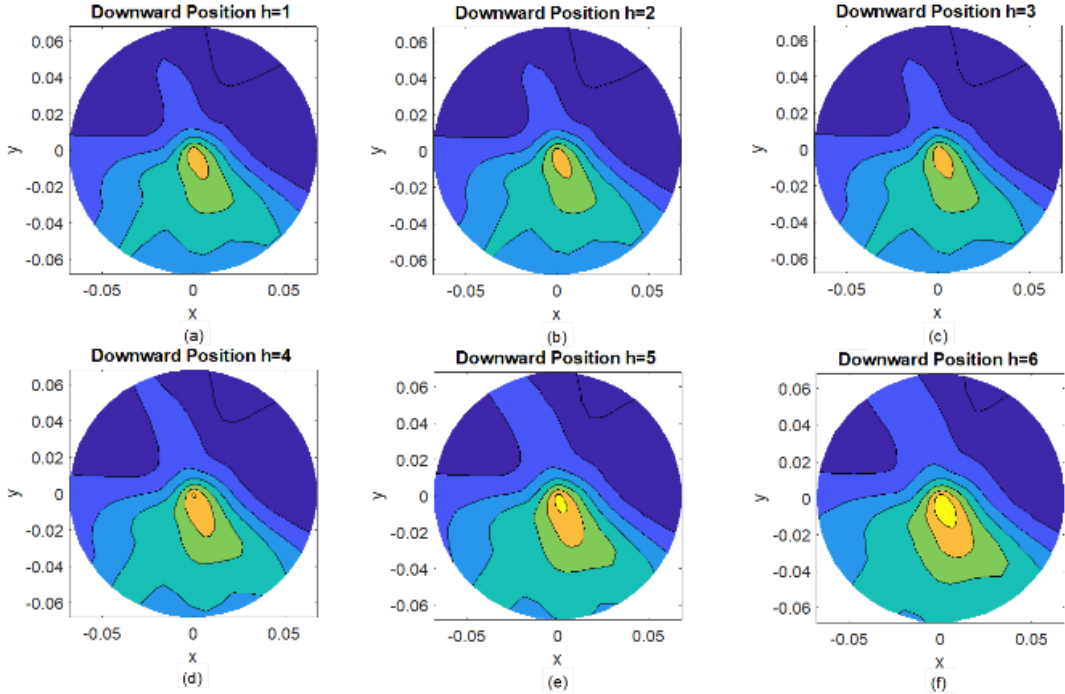


Figure 5.6: Microwave images with detected inclusion at reference planes: (a) $h=1$, (b) $h=2$, (c) $h=3$, (d) $h=4$, (e) $h=5$, (f) $h=6$. Axes units are meters.

In Figure 5.6, the detected inclusion is shown at different reference positions along the z -axis. Specifically, Figure 5.6 (a) illustrates the inclusion detected at the topmost position, denoted as $h=1$. As moving downward along the z -axis, Figure 5.6 (b) displays the detected inclusion at $h=2$, Figure 5.6 (c) at $h=3$, and so on until $h=6$. The presented results in Figure 5.6 provide a clear visual representation of how the size of the detected inclusion varies when measurements are taken at multiple planes along the z -axis. The dimensional analysis of the detected inclusion can be observed by comparing the results from different planes with realistic parameters.

Insights into how the detected inclusion's dimensions change as they move through the object along its depth can be gained by plotting the results for each plane separately along the z -axis. This analysis helps to understand the internal structure better and allows for comparison with realistic dimensions, which are crucial for accurate diagnostic purposes. The visualization of the inclusion at different planes and the dimensional analysis provide valuable information for evaluating the proposed 3D imaging algorithm's effectiveness in

detecting and localizing targets inside the object of interest. These results demonstrate the algorithm's capability to reconstruct a consistent image across multiple planes and illustrate the potential applications of the method in medical imaging scenarios, such as detecting tumors or abnormalities with varying sizes and positions within the human body.

All the images generated at multiple planes have been aligned on the same coordinates. Figures 5.6(d), 5.6(e), and 5.6(f) clearly demonstrate that the size of the detected inclusion increases as the imaging proceeds downwards at different planes along the z-axis. This observed increase in the size of the inclusion validates the successful implementation of the superimposition theorem, which enables 3D visualization of the inclusion at multiple planes. To further enhance the clarity and visual representation of the detected inclusion, images have been processed using an image processing toolbox in MATLAB. The processing involves adjustments and highlights to clearly depict the varying size of the inclusion at multiple planes. A threshold value of 0.5 has been selected to remove clutter without affecting the detection of the target inclusion.

The results of this image processing are presented in Figure 5.7, which displays the highlighted detected inclusion after artefact removal and normalization to the global maximum value. In Figure 5.7, the size of the inclusion is seen to vary and expand while moving downwards along the z-axis. Importantly, the size of the detected inclusion at different heights corresponds well with the actual size of the inclusion present in the experimental setup.

Indeed, the applied image adjustment, which involves applying a threshold to the intensity values, serves to enhance the 3D visualization without altering the information content that could affect target detection and localization. The thresholding process helps emphasize certain features of the image without changing its underlying data or affecting the accuracy of the target detection and localization. Figures 5.6 and 5.7 demonstrate the effectiveness of this image adjustment technique. Both sets of figures show correct detection and localization of the inclusion at multiple planes along the z-axis. However, the visualization of the inclusion varies between the two sets of figures. The applied adjustment highlights the inclusion, making it more prominent in Figure 5.7, which allows for a clearer observation of its varying dimensions and detections at different heights.

The focus on specific features of interest, such as the changing size of the inclusion,

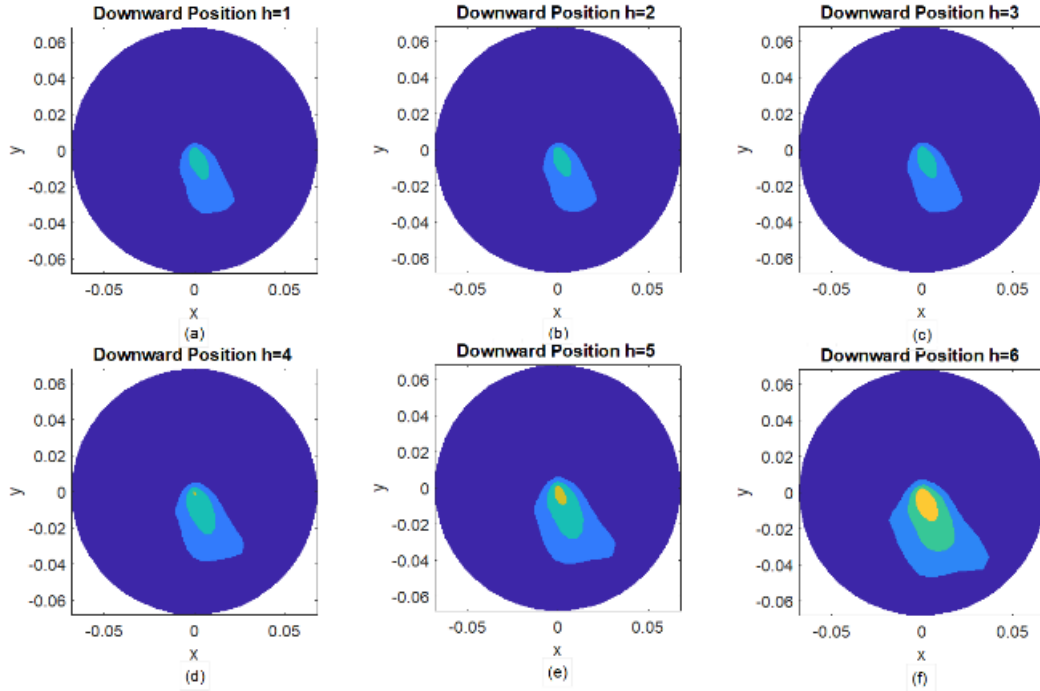


Figure 5.7: Normalized and adjusted microwave images with highlighted inclusion at reference planes: (a) $h=1$, (b) $h=2$, (c) $h=3$, (d) $h=4$, (e) $h=5$, (f) $h=6$. Axes units are meters.

while maintaining the accuracy of the imaging and detection process, can be achieved by applying this adjustment. The adjustment does not alter the underlying data or affect the image reconstruction process, ensuring that the results remain reliable and valid for further analysis and interpretation. This method of image adjustment is valuable for improving the visual representation of the detected inclusion and providing valuable insights into the 3D structure and properties of the object under examination.

Figure 5.8 provides a comprehensive 3D visualization of the detected inclusion with reference to the cross-sections along the z-axis, both before and after normalization and adjustment, respectively. The visualization showcases the detected inclusion at all planes along the z-axis, where measurements were conducted, highlighting the resemblance in dimensions with the realistic inclusion. The results presented in Figure 5.8 serve as strong validation for the potential of the HP-based 3D imaging algorithm, demonstrating its capability to detect the dimensions of the inclusion and effectively reconstruct a 3D image using the superimposition theorem.

The fact that the detected inclusion exhibits consistent dimensions across all planes along the z-axis, and closely resembles the realistic inclusion, reinforces the reliability and accuracy of the proposed 3D imaging algorithm. Overall, the results presented in Figure

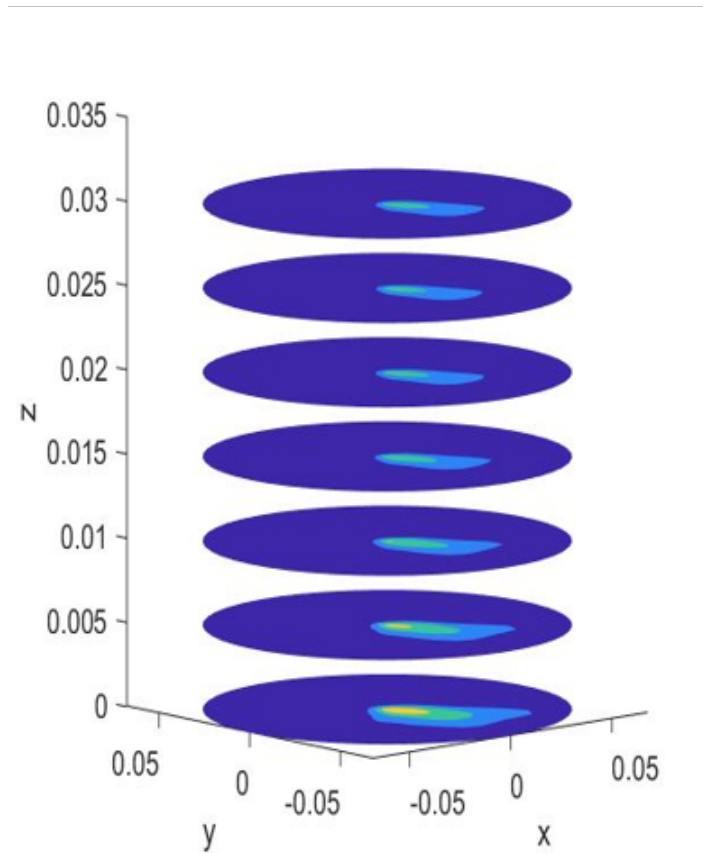
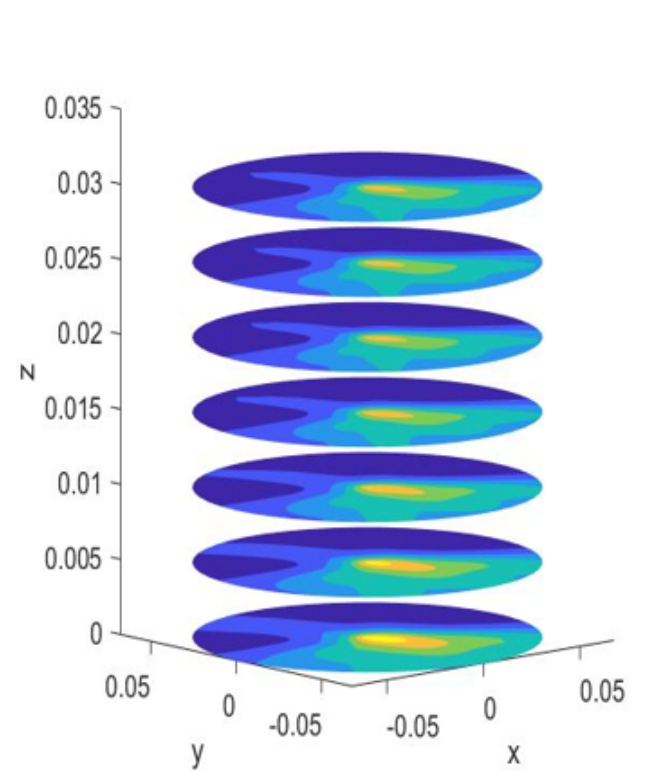


Figure 5.8: Normalized and adjusted microwave images with highlighted inclusion at reference planes: (a) $h=1$, (b) $h=2$, (c) $h=3$, (d) $h=4$, (e) $h=5$, (f) $h=6$. Axes units are meters.

5.8 demonstrate the successful implementation of the HP-based 3D imaging algorithm in detecting and localizing the inclusion accurately. The ability to generate realistic 3D images via the superimposition theorem further establishes the algorithm’s potential as a valuable tool for various medical imaging scenarios, enabling improved diagnostic capabilities and aiding in the understanding of complex structures and abnormalities within biological tissues.

5.4.2 Image Quantification

Quantifying the results is an essential step in validating the performance of the HP-based 3D imaging algorithm. For this purpose, two key metrics were employed: SCR and dimensional analysis of the inclusion at multiple planes along the z-axis. SCR is a crucial measure of the algorithm’s ability to detect and distinguish the inclusion from the surrounding clutter. It is defined as the ratio between the maximum intensity calculated within the region of the inclusion and the maximum intensity outside the region of the inclusion [54]. Insights into how effectively the algorithm identifies the inclusion amid the surrounding noise or clutter can be gained by calculating the SCR at each plane along the z-axis. The results of the SCR calculations are presented in Table 5.2. The table clearly indicates that the inclusion has been successfully detected along the z-axis dimensions. The high SCR at each plane demonstrates the algorithm’s robustness in identifying and isolating the inclusion from the background, ensuring accurate localization and detection.

In addition to the SCR, a dimensional analysis of the inclusion at multiple planes was also conducted. By comparing the detected dimensions of the inclusion at different heights with the actual dimensions of the fabricated inclusion, accuracy and reliability of the 3D imaging algorithm can be assessed. This analysis further validates the algorithm’s ability to reconstruct consistent and realistic 3D images.

Table 5.2: Signal to clutter at multiple planes along the z-axis.

Z_h along the z-axis	Planes / Cross-sections	Signal to Clutter ratio (SCR) [dB]
Reference plane	h=1	7.88
0.5 cm Downward	h=2	7.94
1 cm Downward	h=3	7.92
1.5 cm Downward	h=4	10.52
2 cm Downward	h=5	10.59
2.5 cm Downward	h=6	10.54

The dimensional analysis is a critical aspect of validating the 3D HP-based imaging algorithm. In this study, a comparison between the realistic parameters of the inclusion and the parameters detected by the algorithm has been performed. The 3D structured inclusion used in the study possesses different dimensions at various cross-sections along the z-axis. Table 5.3 presents the dimensions of the detected inclusion at multiple planes, measured in terms of the average diameter, and compares them with the realistic parameters. The calculated error percentage is also provided to assess the accuracy of the algorithm in detecting the dimensions of the inclusion. The results of the image quantification demonstrate the successful implementation of the 3D HP-based imaging algorithm. The SCR, ranging from 7 to 10 dB, indicates the algorithm's ability to effectively distinguish the inclusion from the clutter in the images, ensuring reliable target detection and localization.

Moreover, the detection of the dimensions of the inclusion with an error lower than 7.5% further confirms the accuracy and precision of the algorithm's dimensional analysis. The close agreement between the detected and realistic parameters of the inclusion showcases the algorithm's capability to accurately reconstruct the 3D structure of the target. The quantitative results presented in Table 5.3 provide strong evidence of the algorithm's effectiveness in detecting and visualizing the inclusion's dimensions at different planes along the z-axis. The low error percentage and high SCR ratio validate the algorithm's robustness and potential for practical applications in medical imaging, offering valuable insights for diagnostic and research purposes.

Table 5.3: Dimensional analysis and error % calculations at multiple planes.

Z_h / Cross-sections	Diameter of Fabricated Inclusion [cm]	Diameter (average) of detected Inclusion [cm]	Error Percentage [%]
h=1	1	1.02	2
h=2	1	1.07	7
h=3	2.2	2.04	7.27
h=4	2.6	2.5	3.8
h=5	3	2.9	3.3
h=6	3.5	3.7	5.71

To validate the ability of the 3D HP-based imaging algorithm to accurately localize the inclusion, a specific methodology was developed. For comparison purposes, they have considered the results obtained at specific heights along the z-axis, namely h=2, 4, and

6, as shown in Figure 5.9.

In Figure 5.9, the true position and dimension of the inclusion at each height is marked with a red circle. This true position and dimension are known from the experimental setup and serve as the ground truth for validation. By comparing the detected inclusion’s position and dimension with the ground truth (represented by the red circles), the accuracy of the algorithm’s localization can be quantitatively assessed.. This validation step provides a rigorous examination of how well the algorithm can pinpoint the actual position and size of the inclusion at different heights within the object.

The comparison results shown in Figure 5.9 provide important insights into the algorithm’s performance in localizing the inclusion accurately. If the detected positions and dimensions closely align with the ground truth, it confirms the algorithm’s precision in reconstructing the 3D structure and spatial distribution of the inclusion within the object.

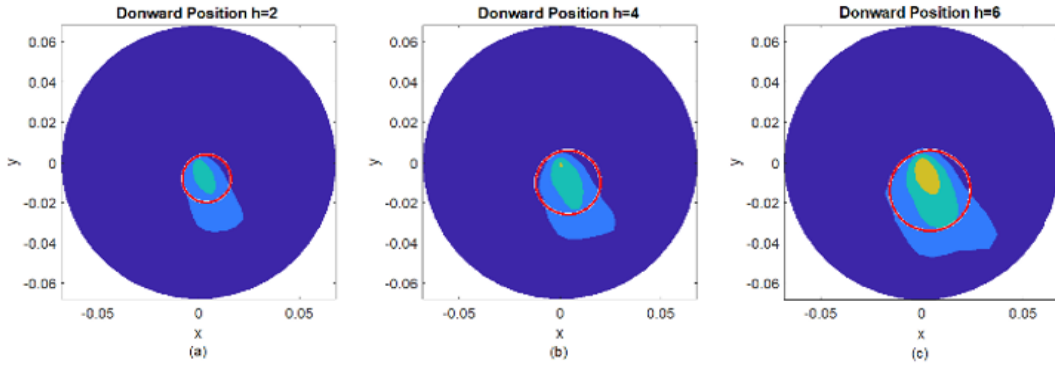


Figure 5.9: Microwave images with detected inclusion (circled) at $h=2$, 4 and 6. Axes units are meters.

The robustness of the HP-based imaging algorithm is a crucial aspect to assess its reliability and applicability in real-world scenarios. In order to evaluate its performance under different conditions, two studies have been conducted where the algorithm was provided with altered permittivity and conductivity information as input. Despite the changes in the dielectric properties of the surrounding medium (free space), the algorithm was still able to successfully detect the inclusion. This outcome indicates that the HP algorithm demonstrates robustness in the face of errors or uncertainties in the knowledge of dielectric properties.

While the detected inclusion’s position remains slightly displaced from the original, and the dimension accuracy is slightly decreased, the fact that the algorithm can still detect the inclusion even with altered parameters is a positive sign of its stability and re-

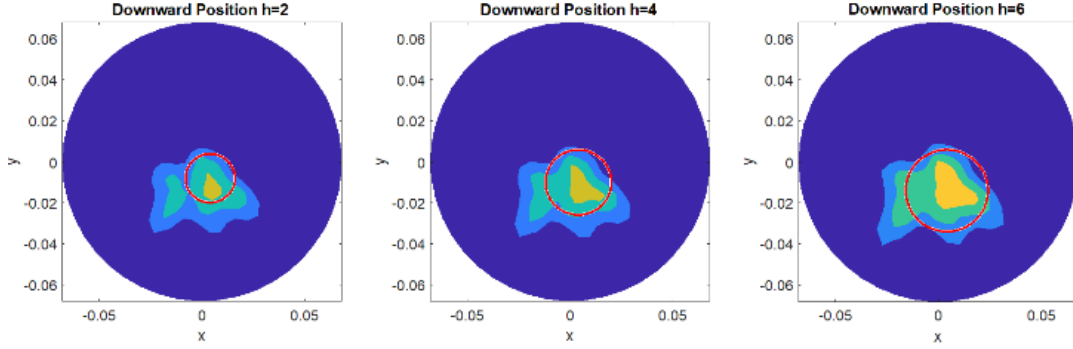


Figure 5.10: Normalized and adjusted Microwave images with detected inclusion (permittivity increased by a factor of 4) at $h=2$, 4 and 6. Axes units are meters.

liability. To thoroughly examine the algorithm's performance, modifications were applied to all six planes along the z -axis. However, for visualization purposes, only planes 2, 4, and 6 along the z -axis have been highlighted in Figures 5.10 and 5.11. In Figure 5.10 and 5.11, the circled parts illustrate that the actual position of the inclusion is slightly displaced compared to the detected position. This slight displacement highlights the impact of altered dielectric properties on the accuracy of the algorithm's localization.

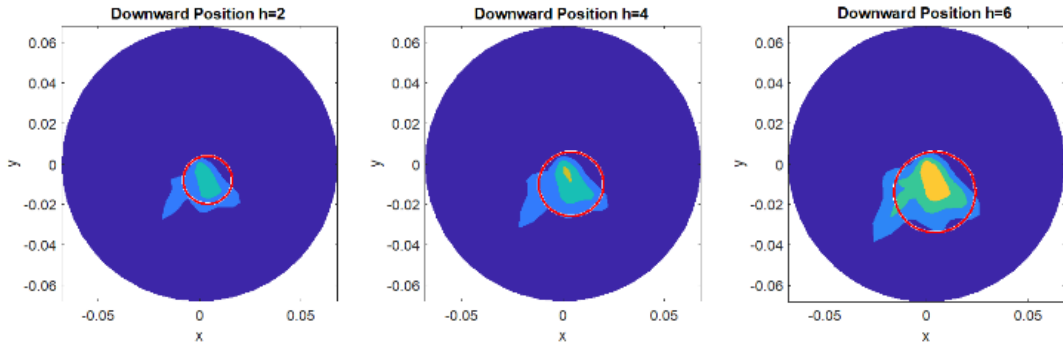


Figure 5.11: Normalized and adjusted Microwave images with detected inclusion (permittivity and conductivity increased by factors of 4 and 2, respectively) at $h=2$, 4 and 6. Axes units are meters.

The quantification of the results obtained in Figures 5.10 and 5.11 were performed to assess the performance of the HP-based imaging algorithm under altered dielectric properties. Calculated SCR at each plane along the z -axis for both scenarios are presented in Table 5.4. In Table 5.2, SCR was calculated for the original scenario with free space dielectric properties, and the high values of SCR indicated successful detection and localization of the inclusion.

In Table 5.4, SCR is shown for the modified scenario with altered permittivity and

conductivity information. Although the localization of the inclusion is still achieved successfully, SCR drops compared to the results in Table 5.2. The decrease in SCR indicates that the altered dielectric properties have introduced some level of noise or uncertainty into the imaging process.

It is essential to consider the trade-off between the accuracy of the detected inclusion and the SCR. In practical scenarios, some level of uncertainty or noise may exist due to various factors, and the algorithm’s ability to maintain localization under such conditions is valuable. Overall, the quantification results in Table 5.4 confirm that the HP-based imaging algorithm remains capable of detecting and localizing the inclusion under altered dielectric property scenarios.

Table 5.4: Signal to clutter comparison with increased values of ε & σ at multiple planes along the z -axis.

Z_h along the z -axis	SCR[dB] $\varepsilon_r = 4$ Reference plane, $h = 1$	SCR[dB] $\varepsilon_r = 4, \sigma = 0.2$ [S/m]
0.5 cm Downward, $h = 2$	1.21	2.99
1 cm Downward, $h = 3$	2.74	2.93
1.5 cm Downward, $h = 4$	2.72	3.50
2 cm Downward, $h = 5$	4.16	3.91
2.5 cm Downward, $h = 6$	5.87	4.19

The dimensional analysis error of the detected inclusion is an important metric that indicates the accuracy of the algorithm’s reconstruction of the inclusion’s size compared to the ground truth. In the original scenario with free space dielectric properties (as shown in Table 5.3), the dimensional analysis error was 7.5%, indicating a relatively accurate reconstruction of the inclusion’s dimensions. However, when the permittivity was increased in the modified scenario, the dimensional analysis error increased to 18%. This indicates that the algorithm’s ability to precisely reconstruct the size of the inclusion is affected by the inaccurate information provided.

Furthermore, when both permittivity and conductivity were increased in the modified scenario, the dimensional analysis error increased to 24%. This shows that the inclusion’s dimensions were even less accurately reconstructed when both dielectric properties were altered.

While the dimensional analysis errors may have increased, the algorithm’s capability to provide a qualitative detection and localization of the inclusion is valuable in real-world scenarios. Medical imaging applications often encounter variations and uncertainties, and

the algorithm's ability to maintain detection and localization under such conditions can be beneficial. In summary, the increase in dimensional analysis error when increasing permittivity or both permittivity and conductivity indicates the impact of inaccurate dielectric properties on the reconstruction accuracy

The localization error, which represents the distance between the actual centre of the inclusion and the centroid of the detected inclusion in the normalized and adjusted image, has been calculated to further validate the effect of dielectric properties on the algorithm's localization accuracy. Table 5.5 presents the results of this analysis. To calculate the centroid, binary version of the adjusted reconstruction image was created through thresholding. Thresholding is a common image processing technique that converts a grayscale image into a binary image by setting a certain threshold value. Pixels with intensity values above the threshold are set to one (representing the inclusion), and pixels below the threshold are set to zero (representing the background).

Using this binary image, the centroid of the detected inclusion was determined, and its distance from the actual centre of the inclusion was measured. The localization error was then computed as the distance between these two points. Table 5.5 shows the localization error before and after changing the dielectric properties. As expected, when the dielectric properties were altered, the localization error increased compared to the original scenario with free space dielectric properties. The increase in localization error indicates that inaccuracies in dielectric properties can affect the algorithm's ability to precisely locate the inclusion's centre. However, despite the increase in localization error, the algorithm was still capable of detecting and approximately localizing the inclusion.

In conclusion, this research have effectively demonstrated the impact of dielectric properties on localization accuracy through the calculation of the localization error. The algorithm's ability to maintain detection and localization, despite the errors introduced by altered dielectric properties, highlights its potential for reliable and robust medical imaging.

From Table 5.5 and the images in Figures 5.9 and 5.10, it is evident that the localization error increases when the dielectric properties are altered. The localization error represents the difference between the actual centre of the inclusion and the centroid of the detected inclusion in the reconstructed image. As the dielectric properties are changed, the algorithm's ability to precisely locate the centre of the inclusion is affected. This

Table 5.5: Localization error comparison between free space parameters and increased values of ε & σ at multiple planes along the z-axis.

Z_h	Localization error (mm) Free space parameters	Localization error (mm)	
		$\varepsilon_r = 4$ $h = 2$	$\varepsilon_r = 4, \sigma = 0.2$ [S/m]
$h = 4$	5.82	7.66	7.78
$h = 6$	7.57	10.57	10.65

results in an increase in the localization error, indicating that the algorithm’s localization accuracy degrades when inaccurate dielectric information is provided. Despite the increase in localization error, the detection results still satisfy the aim of validating the robustness of the imaging algorithm with respect to the knowledge of dielectric properties. The algorithm successfully detects the inclusion’s presence and provides a qualitative localization, even though the accuracy of the localization may be reduced. This finding is important in the context of real-world medical imaging scenarios, where uncertainties and variations in dielectric properties are common. The algorithm’s ability to maintain detection and provide approximate localization under such conditions is valuable in practical applications. Overall, the research demonstrates the trade-off between detection and localization accuracy when dealing with altered dielectric properties. While the localization error may increase, the algorithm’s robustness in detecting the inclusion remains intact, showcasing its potential for reliable imaging even in uncertain environments.

5.4.3 Skull Mimicking Phantom Results

In this part of the research, the same measurement procedure as the previous experiment was applied to the skull-mimicking phantom. Six measurements were taken at multiple planes along the z-axis, starting from the top of the skull phantom and going downwards. To validate the 3D imaging algorithm’s ability to manage varying dielectric properties along the z-axis, a cylindrical inclusion with uniform cross-section was fabricated. The dielectric properties of the inclusion varied along the z-axis, with the bottom 1 cm filled with water and the remaining part filled with the same oil used in the skull. This setup represented a 3D variation in dielectric properties along the z-axis, simulating real-world scenarios where tissues may have different dielectric properties at various depths.

Figures 5.12 and 5.13 show the reconstructed images obtained from the experimental data using the proposed HP-based 3D imaging algorithm. Figure 5.12 depicts the recon-

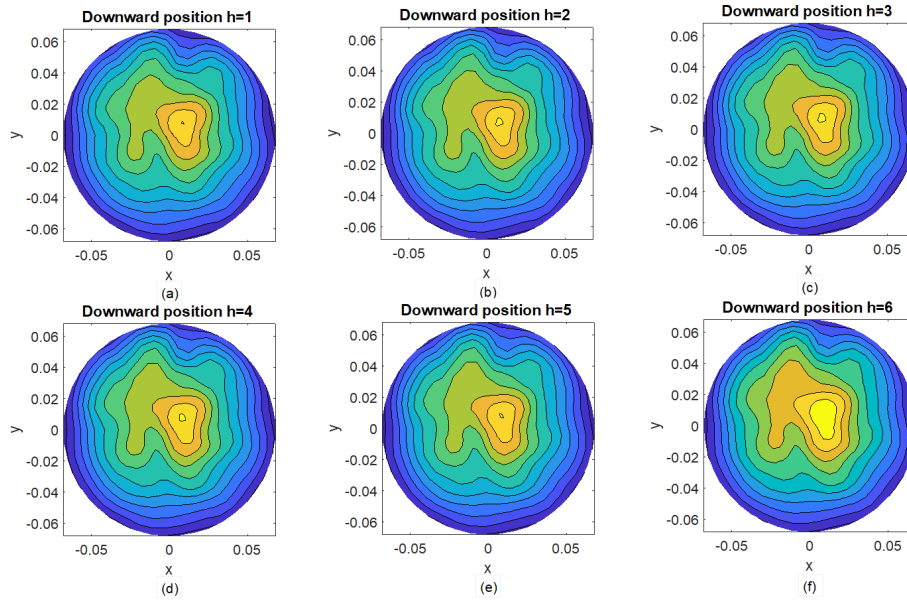


Figure 5.12: Microwave images with detected inclusion at reference planes (head-phantom): (a) $h=1$, (b) $h=2$, (c) $h=3$, (d) $h=4$, (e) $h=5$, (f) $h=6$. Axes units are meters.

structured images before normalization and adjustment, while Figure 5.13 shows the images after normalization and adjustment. The adjustment involves highlighting the detected inclusion to clearly observe its varying dimensions along the z -axis, while the normalization process scales the intensity values to provide a more consistent visualization.

The obtained images from the skull-mimicking phantom experiment reveal the highest SCR of 9 dB at plane 6. This indicates that the algorithm's performance is most pronounced at the cross-sectional analysis of the plane where the portion filled with 1 cm of water (mimicking the inclusion) is present. The high SCR at this specific plane indicates successful detection and localization of the inclusion. Figure 5.14 showcases the successful 3D visualization of the reconstructed images after normalization and image adjusting. The visualization of the detected inclusion has been improved by applying these techniques, providing a clearer representation of its dimensions along the z -axis.

The results in Figures 5.12, 5.13 and 5.14 further validate the capability of the proposed HP-based 3D imaging algorithm to handle variations in dielectric properties along the z -axis. The algorithm successfully identifies and visualizes the inclusion with varying dielectric properties at different cross-sections of the phantom. Overall, the high SCR at plane 6 and the successful 3D visualization in Figure 5.14 indicate that the algorithm performs effectively even in complex scenarios with varying dielectric properties. This demonstrates the algorithm's robustness and potential for accurate imaging in medical

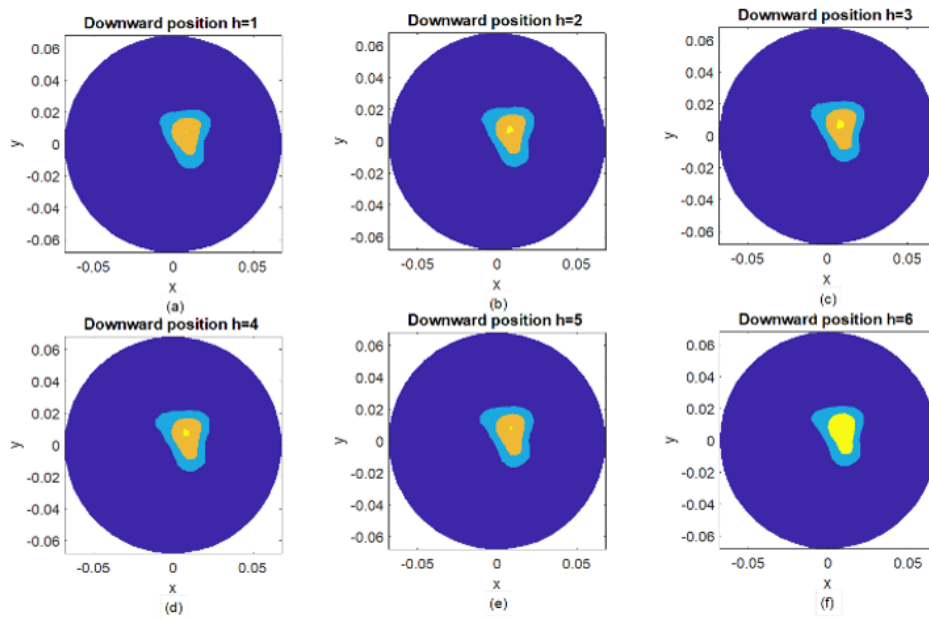


Figure 5.13: Normalized and adjusted microwave images with detected inclusion at reference planes (head-phantom): (a) $h=1$, (b) $h=2$, (c) $h=3$, (d) $h=4$, (e) $h=5$, (f) $h=6$. Axes units are meters.

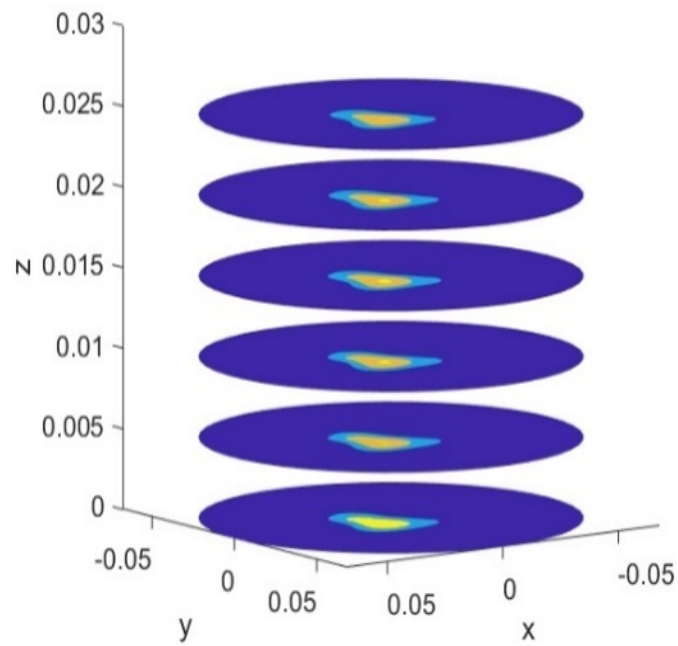


Figure 5.14: 3D Visualization of the detected inclusion in multiple cross-sections along the z-axis (head-phantom) after normalization and image adjusting. Axes units are meters.

applications, especially when dealing with tissues with non-uniform dielectric properties along the imaging depth.

5.4.4 3-layer Phantom Results

In the experiment involving the 3-layer cylindrical phantom, the same experimental methodology was applied as in the previous cases. Measurements were performed at six multiple planes along the z-axis, with the height of the antennas changed simultaneously. Figures 5.15 and 5.16 display the reconstructed images obtained for the six planes along the z-axis before and after image normalization and adjustment, respectively. Figure 5.15 shows the images before normalization and adjustment, while Figure 5.16 presents the same images after applying normalization and adjustment techniques. The algorithm's performance in detecting and localizing the inclusion within the 3-layer cylindrical phantom can be validated by analyzing the images in Figures 5.15 and 5.16. These images demonstrate the algorithm's capability to handle complex scenarios with multiple layers of different dielectric properties, successfully visualizing the detected inclusion at various depths along the z-axis. These results further reinforce the robustness and effectiveness of the proposed HP-based 3D imaging algorithm, confirming its potential as a reliable technique for medical imaging applications. The ability to accurately detect and visualize inclusions within complex phantoms opens up possibilities for its use in real-world medical imaging scenarios, where tissues often have varying dielectric properties across different layers

In this particular experiment with the 3-layer cylindrical phantom, a specific design was employed to fill only the spherical part of the inclusion with the fabrication mixture. The objective was to assess how this variation in the inclusion's dielectric properties would be reflected in the reconstructed images. Figures 5.15 and 5.16 indeed demonstrate the successful detection of the spherical cross-sectional analysis. This detection is most prominently visible at $h=6$ along the z-axis, which corresponds to the height with the largest diameter of the inclusion. At this particular height, the reconstructed images exhibit the highest SCR ratio of 10.48 dB. The ability to successfully detect the spherical part of the inclusion at $h=6$, along with the high SCR, further validates the effectiveness of the HP-based 3D imaging algorithm. It indicates that the algorithm is capable of accurately identifying and visualizing the inclusion's dimensions, even in scenarios where

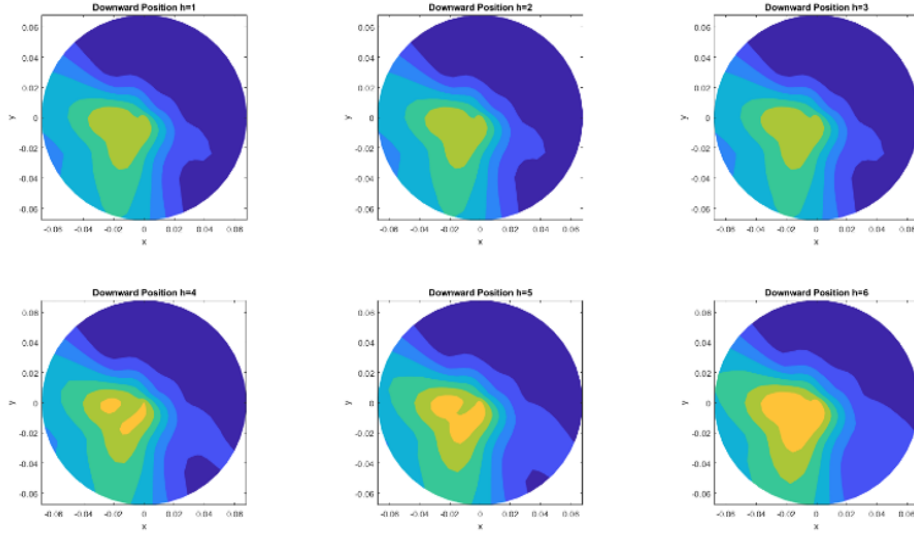


Figure 5.15: Microwave images with detected inclusion at reference planes (3-layer phantom): (a) $h=1$, (b) $h=2$, (c) $h=3$, (d) $h=4$, (e) $h=5$, (f) $h=6$. Axes units are meters.

only specific parts of the inclusion possess altered dielectric properties.

Overall, the results presented in Figures 5.15 and 5.16 demonstrate the algorithm's robustness and its potential to handle complex scenarios with varying dielectric properties. It showcases the algorithm's ability to accurately reconstruct the internal structures of multi-layered phantoms and detect the presence of inclusions at different depths along the z -axis. Regarding the dimensional analysis error, which compares the detected inclusion's dimensions with the realistic setup, the error is found to be less than 6% at $h=6$ in this experiment. Although this error is slightly higher than the corresponding error at the same height in the first experiment (reported in Table 5.3), it is still within an acceptable range. The fact that the algorithm performs well in both experiments, despite the differences in inclusion types and dielectric properties, indicates the robustness and effectiveness of the HP-based imaging algorithm [106]. Subsequently, Figure 5.17 shows the 3D visualization of the reconstructed images after image normalization and adjustment at multiple slices along the z -axis.

5.5 Summary

The proposed 3D imaging algorithm based on the Huygens principle has shown promising results in detecting and visualizing internal structures in medical imaging. In this Chapter, measurements were performed on three fabricated phantoms to validate the

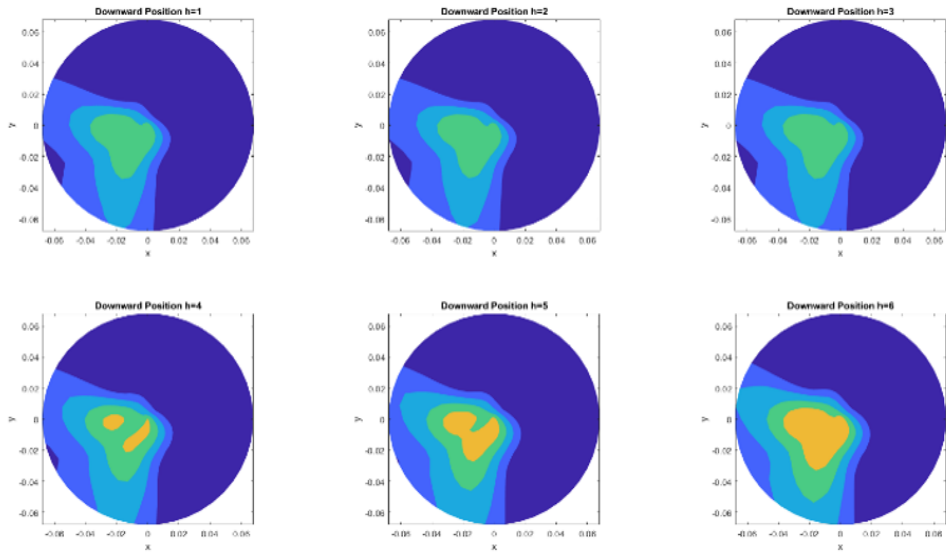


Figure 5.16: Normalized and adjusted microwave images with detected inclusion at reference planes (3-layer phantom): (a) $h=1$, (b) $h=2$, (c) $h=3$, (d) $h=4$, (e) $h=5$, (f) $h=6$. Axes units are meters.

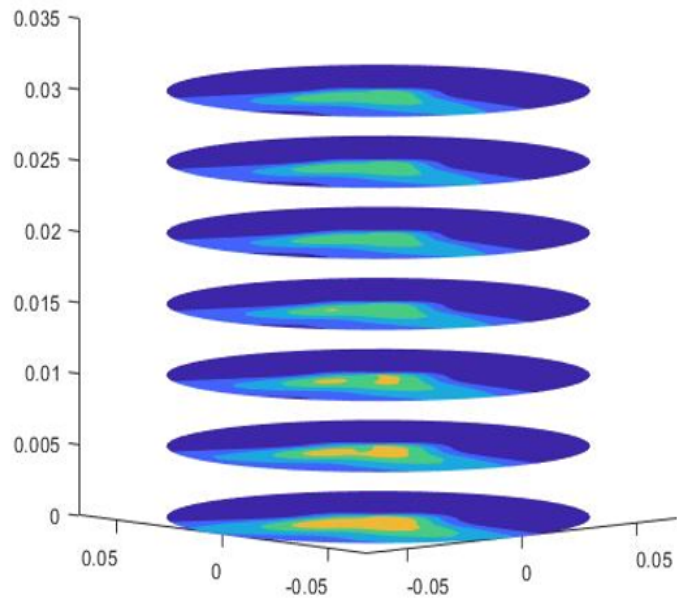


Figure 5.17: 3D Visualization of the detected inclusion in multiple cross-sections along the z-axis (3-layer phantom) after normalization and image adjusting. Axes units are meters.

algorithm's effectiveness. The complex signals S21 were obtained using 5 transmitting positions arranged in triplets and 80 receiving points at different planes along the z-axis Z_h . The first phantom used in the study included a 3D structured inclusion, consisting of a tube with a spherical bottom. Measurements were taken at multiple planes along the z-axis using MammoWave, which is known for its safety as it does not employ ionizing radiation. MammoWave was operated through a user-friendly GUI, allowing for automated antenna positioning and facilitating measurements at different planes. The algorithm successfully processed the received signals and reconstructed the 3D images of the inclusion at various depths along the z-axis. The results were validated through dimensional analysis, which confirmed the accurate detection of the inclusion's dimensions. Additionally, a skull-mimicking phantom and a 3-layer cylindrical phantom were used to test the algorithm's robustness in handling multi-layered complex scenarios. The algorithm demonstrated its ability to handle such scenarios and successfully localized the internal structures, even in cases where dielectric properties varied along the z-axis. Overall, this research presented a novel and efficient 3D imaging algorithm for medical applications, showcasing its potential for non-invasive and safe diagnostic imaging. The ability to visualize internal structures accurately and safely using MammoWave makes this algorithm a valuable tool for medical professionals in the field of imaging and diagnostics.

The investigation successfully achieved the main goal of visualizing the detected inclusion in 3D. The superimposition theorem was employed to combine the results obtained from multiple planes along the z-axis Z_h , allowing for the visualization of the inclusion's 3D structure. The results demonstrated that the size of the detected inclusion varied in accordance with the realistic inclusion, with an error of less than 7.5%. To further validate the proposed 3D imaging algorithm, experiments were conducted on a skull-shaped head phantom containing a cylindrically shaped inclusion. The measurements were repeated at different planes along the z-axis, and the results showed prominent target detection at the last plane, which aligned with the setup and verified the successful implementation of the algorithm. The algorithm's robustness was further tested in a more complex scenario involving a 3-layer phantom with varying dielectric properties and a 3D structured spherical inclusion. Despite the complexity of the setup, the algorithm still successfully detected and localized the inclusion, with the dimensional analysis error remaining below 6% .

Chapter 6

A Spiral-like Acquisition Strategy for 3D Huygens' Principle Based Microwave Imaging

6.1 Introduction

This Chapter focuses on the implementation of a novel methodology to achieve a reduction in imaging time by employing a 3D imaging HP algorithm, integrated with MammoWave. The specific approach involves using a three-layer cylindrical phantom with a 3D structured inclusion, characterized by varying dielectric properties. The primary objective of the study is to investigate the feasibility of reducing measurement time while maintaining acceptable imaging accuracy. To this end, various spiral-like measurement scenarios along the z-axis were explored. In the first scenario, measurements were conducted in a spiral-like configuration (configuration-I) at multiple planes along the z-axis. The second scenario involved an alternate application of spiral configuration (configuration-II) with respect to receiving points.

The findings of the study indicate that the proposed spiral-like measurement scenarios hold promise in achieving a notable 50% reduction in measurement time. However, it is essential to consider the trade-offs associated with this time reduction. Notably, there is a decrease in the SCR, with a maximum reduction of approximately 3.2 dB. Additionally, there is a slight increase in error (around 3.5%) in the dimensional analysis and localization of the 3D structured inclusion. Despite the observed trade-offs, the study

demonstrates the potential advantages of implementing spiral-like measurement configurations for expedited imaging. This Chapter highlights the need for carefully considering the balance between time reduction and imaging accuracy. The results open avenues for further exploration and optimization of the 3D imaging algorithm to achieve enhanced efficiency and precise localization of structures of interest within the phantom.

6.2 Experimental Insights

Over the last two decades, MWI has gained widespread recognition as a novel diagnostic technique, particularly in the realm of breast cancer detection [107]. It has also shown promise in detecting various diseases at early stages, such as brain strokes, bone fractures, and skin cancer, offering a viable alternative to conventional imaging technologies like ultrasounds, X-rays, and MRI [108]. One of the key advantages of MWI lies in its utilization of non-ionizing radiation, ensuring safe and risk-free medical imaging for patients. By exploiting the distinct physical dielectric properties of healthy and diseased tissues, MWI can effectively differentiate between these tissues at the receiver's end [109].

The research community actively explores MWI for diverse applications, particularly 3D medical imaging, holding significant promise for improved diagnostic precision and treatment planning [110]. MWI's non-invasive, high-resolution imaging capabilities position it as a promising avenue for continued research, expected to play a vital role in early disease detection and healthcare advancements. In this research, I had introduced a novel 3D MWI technique based on HP and applied it using the rapid MWI device known as MammoWave [12]. By leveraging the HP-based MWI methodology, the need to solve complex inverse scattering problems and perform matrix inversions has been eliminated. Additionally, this approach enables to capture and combine information from individual frequencies, leading to the reconstruction of a consistent image with highly accurate localization and minimal error [41]. Recent developments have further expanded the capabilities of the 3D imaging technique based on HP, employing the MammoWave system, as presented in [102, 106]. Notably, successful 3D image reconstruction has been achieved, showcasing the potential of this approach. In [106], a comprehensive analysis of the reconstructed images has been conducted, specifically focusing on dimensional analysis error and localization error calculations. The results have demonstrated the technique's

effectiveness in accurately determining the various dimensions of lesions along the z-axis.

However, it is essential to acknowledge that the current methodology in [106] still requires considerable time for data acquisition and processing. Measurements on six different cross-sections along the z-axis were performed for 3D image reconstruction in [106], with each measurement taking approximately 9 minutes. As continuous improvement and optimization are pursued, the goal remains to further reduce the overall imaging time. Advancing the research, the primary objective is to further enhance the time efficiency of the proposed methodology. Currently, the methodology achieves a notable reduction in session time, averaging between 9-10 minutes, which is a considerable improvement compared to the conventional 45-60 minutes required for a full MRI session. This endeavor aligns with the pursuit of streamlined processes, particularly crucial in the context of 3D imaging, where swift acquisition of data is paramount for optimizing diagnostic outcomes. To achieve this, two novel scenarios involving spiral-like acquisitions along the z-axis have been introduced and investigated, each with distinct configurations. These scenarios were meticulously tested on a complex three-layer cylindrical phantom featuring a 3D structured inclusion, which serves as a representative testing case. The core objective of this study is to analyse and quantify the impact of these proposed time-saving approaches in terms of SCR, dimensional error, and localization error. A thorough understanding of the effectiveness and practicality of the two spiral-like acquisition configurations (configuration I and II) in reducing imaging time while preserving diagnostic accuracy is sought by evaluating these key metrics.

Moreover, in addition to the two spiral-like acquisition configurations, an additional configuration is further explored and tested. The purpose of this testing was to assess the potential for achieving significant time reduction while minimizing errors. Through this rigorous analysis, the aim is to identify the most optimal and efficient approach that strikes the ideal balance between time savings and imaging precision. By thoroughly examining the results obtained from these experiments, valuable insights into enhancing the efficiency and effectiveness of the 3D MWI technique are intended to be offered. Ultimately, this research endeavours seek to contribute to the advancement of medical imaging technologies, ensuring faster and more accurate disease detection and diagnostic processes.

6.3 Methodology

In this chapter, the fabrication of a sophisticated phantom featuring three cylindrical layers, along with a 3D structured spherical inclusion possessing varying dielectric properties, is undertaken. For this purpose, specialized liquids from ZMT Zürich MedTech, Switzerland, are procured and employed to create the distinct cylindrical layers, as detailed in Table 6.1.

To fabricate the spherical 3D structured inclusion, a mixture comprising 40% glycerol and 60% water has been utilized, which exhibited the specific dielectric properties outlined in Table 6.1. To introduce a more intricate scenario, a unique approach is employed during the inclusion fabrication process. Specifically, the spherical part of the inclusion is filled with the designated mixture, while the remaining portion of the tube is left empty. By implementing this novel fabrication methodology, the aim is to simulate a complex and realistic environment for microwave imaging experiments. This multi-layered phantom, along with the 3D structured inclusion, allows for the accurate assessment and validation of the performance and capabilities of the proposed imaging techniques. In the fabricated

Table 6.1: Dielectric properties of materials used in phantom fabrication.

Fabrication Materials	Relative Permittivity (ϵ_r)	Conductivity (σ) [S/m]
TLe11.5c.045oil (external layer)	7	0.3
TLe5c24 oil (internal layer)	5	0.2
40% glycerol and 60% water	60	2

phantom, the cylinders representing the external and internal layers possess respective diameters of 11 cm and 7 cm. The 3D structured spherical inclusion has a diameter of 1 cm at its tube-shaped cross-section and expands to 3.5 cm at its spherical cross-section. Figure 6.1 illustrates the positioning of the spherical inclusion inside the internal cylindrical layer. To create a realistic representation of the internal structure, the two cylinders are deliberately placed with a deviation of 3.5 cm between their centres. This positioning allows to simulate a more complex and accurate scenario, closely resembling the spatial arrangement of internal organs or tissues.

By designing the phantom with such intricate geometries and dimensions, the aim is to test and validate the performance of the proposed microwave imaging technique in a controlled yet realistic environment.



Figure 6.1: The multilayered fabricated phantom with 3D structured inclusion.

6.3.1 Device and Imaging Procedure

In this chapter, the measurements were again performed using the previously described MammoWave device. In the proposed 3D HP based imaging algorithm of Chapter 5 [102, 106], the measurements were performed at 6 planes along the z -axis on multiple fabricated phantoms. This was achieved by simultaneously changing the height of the antennas and reconstructing 3D images. Moreover, the received signals S_{21} were measured for each individual plane along the z -axis. The signal was transmitted at five central Tx planes ($0^\circ, 72^\circ, 144^\circ, 216^\circ, 288^\circ$) with an angular shift of 4.5° , and the signals were received at 80 receiving points covering the range from 0° to 360° at intervals of 4.5° .

The main objective of this experiment instead was to reduce the measurement time while ensuring reliable imaging results. To achieve this, a spiral-like acquisition approach was employed in two distinct configurations. These measurements were carried out at six planes along the z -axis, while systematically varying the height of both antennas denoted as h_1, h_2, \dots, h_6 .

In Configuration-I, a novel data acquisition strategy was introduced to optimize the recording process. Instead of capturing signals at 80 receiving points, a segmented approach was adopted. Specifically, for h_1 , the received signal was recorded using the first 40 receiving points. Similarly, for h_2 , the receiving points from 41 to 80 were considered, and this pattern was continued for subsequent heights. Specifically, for h_3 and h_5 , the

first 40 receiving points has been utilized, while for h_4 and h_6 , the second half of the 80 receiving points has been utilized. This segmentation scheme is visually depicted in Figure 6.2(a). By implementing this modified data acquisition methodology, the aim was to reduce the total number of receiving points required for each height, thereby optimizing the measurement time. The impact of this configuration on the imaging process was carefully analyzed to ensure that it delivers meaningful and accurate information for medical diagnosis and treatment planning.

Similarly, Configuration-II involved a different arrangement of receiving points, specifically tailored to enhance time reduction while maintaining imaging accuracy. The combination of these two configurations allowed to comprehensively evaluate the effectiveness of the spiral-like acquisition approach and identify the most efficient setup for achieving substantial time savings. This approach enables to draw meaningful conclusions and insights from these findings, ultimately contributing to the advancement of microwave imaging techniques for medical applications.

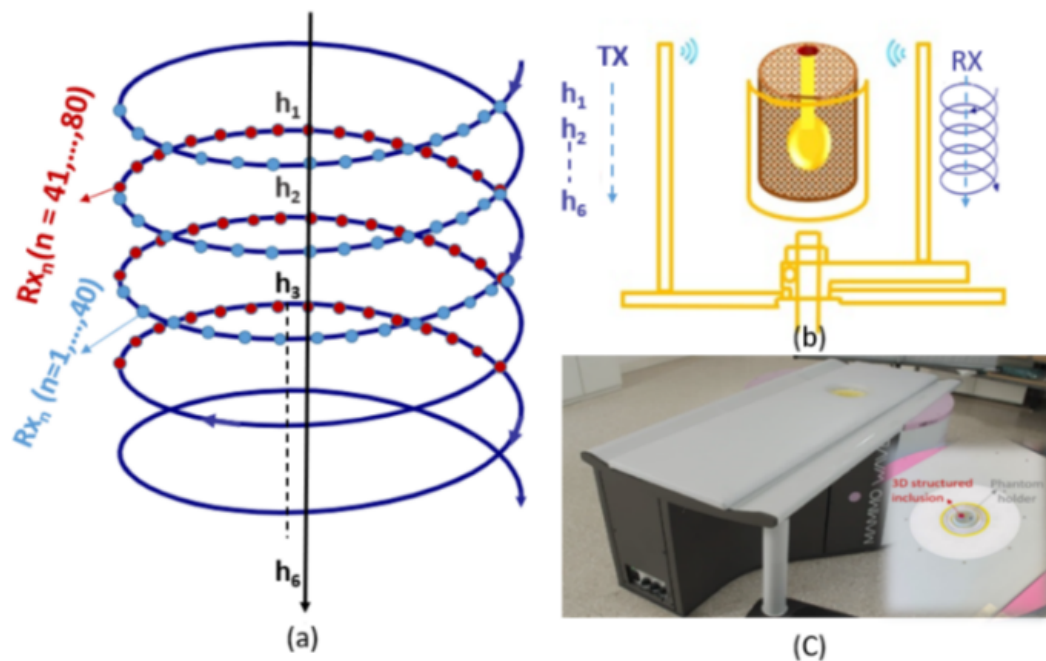


Figure 6.2: (a) Spiral-like acquisition configuration, (b) The experimental schematic, (c) MWI device MammoWave.

In configuration-II, the focus was to record complex S_{21} by evaluating 40 receiving points with alternating 20 receiving points. Specifically, for h_1, h_3 , and h_5 , the data from Rx points 1 to 20 and 40 to 60 was recorded. On the other hand, for h_2, h_4 , and h_6 , Rx points 21 to 40 and 61 to 80 were considered. To conduct the measurements, the fabri-

cated phantom was positioned inside the cylindrical hub of the MammoWave. The data collection process started from the top of the phantom and progressed downwards, capturing measurements at multiple planes along the z-axis. This experimental arrangement allowed to comprehensively assess the effectiveness of the spiral-like acquisition approach in both configurations.

Figure 6.2 provides a visual representation of the experimental setup and the spiral-like configuration used in this research. This pictorial demonstration further enhances the understanding of the procedures and methodologies employed during this microwave imaging experiments. By meticulously documenting this experimental setup and procedures, along with the use of complex $S21$ measurements and the spiral-like configurations, the aim is to present a comprehensive and transparent account of this research. These efforts contribute to the reproducibility of the findings and facilitate comparisons with other studies in the field of medical imaging, particularly in the context of microwave imaging for diagnostic applications.

Indeed, all the measurements conducted in this research were performed in the frequency domain. The choice of operating in the frequency domain offers several advantages, particularly when aiming to reconstruct a consistent and accurate image. Working in the frequency domain allows valuable information to be obtained from all the frequencies used during the measurements. This allows for capturing a view of the electromagnetic properties of the object being imaged. Each frequency provides unique insights into the interaction between the electromagnetic waves and the target, offering a more detailed and complete picture of the internal structures. The ability to combine data from all the frequencies during the reconstruction process is crucial in achieving a consistent image. This approach facilitates the integration of information from different aspects of the object's dielectric properties, resulting in a more robust and reliable representation. The combination of data from multiple frequencies improves the SCR and helps mitigate artefacts and distortions, leading to a higher-quality image. Moreover, working in the frequency domain simplifies the imaging process and reduces computational complexity. It eliminates the need to solve complex inverse scattering problems, as would be required in the time-domain imaging approach.

The received signals at the multiple planes Z_h along the z-axis at different heights h_{n1} and h_{n2} can be represented as $S21_{n1}$ and $S21_{n2}$:

$$S21_{n_1} = S21_{n_1, h_{n_1}}^{m,p}(a_0, \phi_{n_1}, Z_{h_{n_1}}; Tx_{m,p, h_{n_1}}; f)$$

$$S21_{n_2} = S21_{n_2, h_{n_2}}^{m,p}(a_0, \phi_{n_2}, Z_{h_{n_2}}; Tx_{m,p, h_{n_2}}; f)$$

where $n_1 = 1, \dots, 40$ and $n_2 = 41, \dots, 80$ indicate the receiving points representing spiral-like Configuration-I and $n_1 = 1, \dots, 20$ & $40, \dots, 60$ and $n_2 = 21, \dots, 40$ & $61, \dots, 80$ for spiral-like Configuration-II for heights $h_{n_1} = h_1, h_3, h_5$ and $h_{n_2} = h_2, h_4, h_6$ respectively for both configurations along the z-axis; $m = 1, \dots, 5$ stipulates the central Tx points, $p = 1, 2, 3$ shows the positions of the transmitting points with the angular transposition of $\pm 4.5^\circ$ and f signifies the frequency.

These received signals are processed via HP in order to remap the dielectric contrast of the internal field by calculating the external field; according to Huygens' principle, the calculated external field carries the information of the internal field, which can be presented as:

$$E_{(HP,3D)}^{rcstr}(\rho, \phi, Z; Tx_{m,p, h_{n_1}+h_{n_2}}; f) = \sum_{h=1}^{h_{n_1}} \sum_{h=2}^{h_{n_1}} \sum_{n=1}^{n_1} \sum_{n=41}^{n_2} (S21_{n_1} + S21_{n_2}) G(k_1 |(\rho_{n,h})^{\vec{z}} \vec{\rho}|)$$

Hence, the intensity of the consistent 3D image can be obtained by summing all the solutions, i.e., by gathering information from all the receiving points from spiral-like acquisitions along the z-axis for a number of frequencies NF as shown below:

$$I_{3D}(\rho, \phi, Z; Tx_{m,p, h_{n_1}+h_{n_2}}) = \sum_{h=1}^{h_{n_1}+h_{n_2}} \sum_{i=1}^{NF} |E_{(HP,3D)}^{rcstr}(\rho, \phi, Z; Tx_{m,p, h_{n_1}+h_{n_2}}; f_i)|^2$$

Artefact removal has been performed using a rotation-subtraction procedure [106]. Finally, normalization has been applied with respect to the global maximum. The combination of artefact removal through the rotation-subtraction procedure and subsequent normalization helps deliver improved and more accurate microwave images.

6.4 Results and Discussions

In this research, two experiments were conducted involving measurements at six planes along the z-axis. The first experiment utilized a spiral-like configuration (Configuration-I) where the data was recorded from Rx points 1 to 40 for heights h_1 , h_3 , and h_5 , and Rx points 41 to 80 for heights h_2 , h_4 , and h_6 . In the second experiment, a different configuration was used with Rx points 1 to 20 and 40 to 60 for heights h_1 , h_3 , and h_5 , and Rx points 21 to 40 and 61 to 80 for heights h_2 , h_4 , and h_6 . These measurement methodologies led to a significant reduction of 50% in acquisition time compared to the original setup. The results were further quantified using various factors to determine the differences compared to the original configuration.

During the fabrication of the phantom, only the spherical part of the 3D structured inclusion was deliberately filled with the designated mixture. This decision was made to focus on detecting the inclusion specifically at cross-sections 5 and 6, corresponding to heights h_5 and h_6 , as shown in Figure 6.3 [106]. These cross-sections represent crucial areas of interest, and the objective was to accurately identify and analyse the inclusion in these specific regions. By conducting these experiments and analyzing the results, the aim was to validate the effectiveness of the proposed methodologies in reducing acquisition time without compromising the ability to detect and localize the 3D structured inclusion.

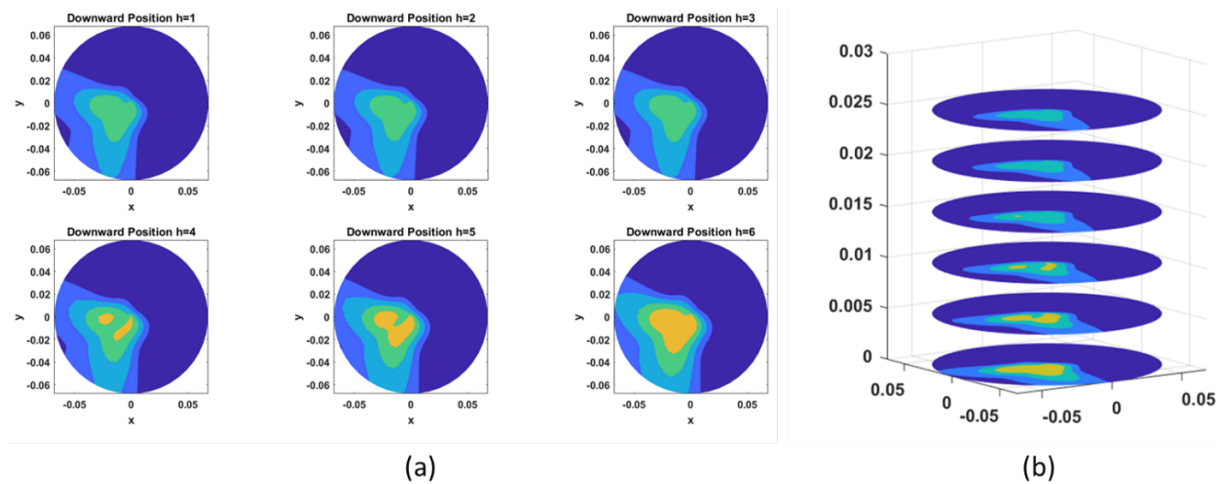


Figure 6.3: (a) Reconstructed microwave images with detected inclusion at reference planes (when employing all receiving points at each height), (b) 3D reconstructed image. Images are produced after normalization and image adjustment. Axes units are meters.

In the first scenario, which involved the spiral-like acquisition configuration-I, the reconstructed images at multiple planes along the z-axis, along with the 3D visualization,

are displayed in Figure 6.4. Notably, Figure 6.4(a) illustrates the images reconstructed at heights h_5 and h_6 . These specific planes exhibit a more prominent depiction of the detected inclusion, with varying dimensions, as compared to the other planes. The results obtained from this scenario clearly indicate the successful implementation of the spiral-like acquisition configuration, yielding promising and noteworthy outcomes.

The visualization of the inclusion at varying heights through the 3D visualization further confirms the efficacy of the spiral-like acquisition configuration-I. This visualization enhances the understanding of the internal structures and dimensions of the 3D inclusion, thereby reinforcing the value of microwave imaging for medical applications. Overall, the outcomes presented in Figure 6.4 affirm the successful implication of the spiral-like acquisition configuration-I in achieving accurate and reliable microwave imaging results, particularly in detecting and localizing the 3D structured inclusion at different heights along the z-axis.

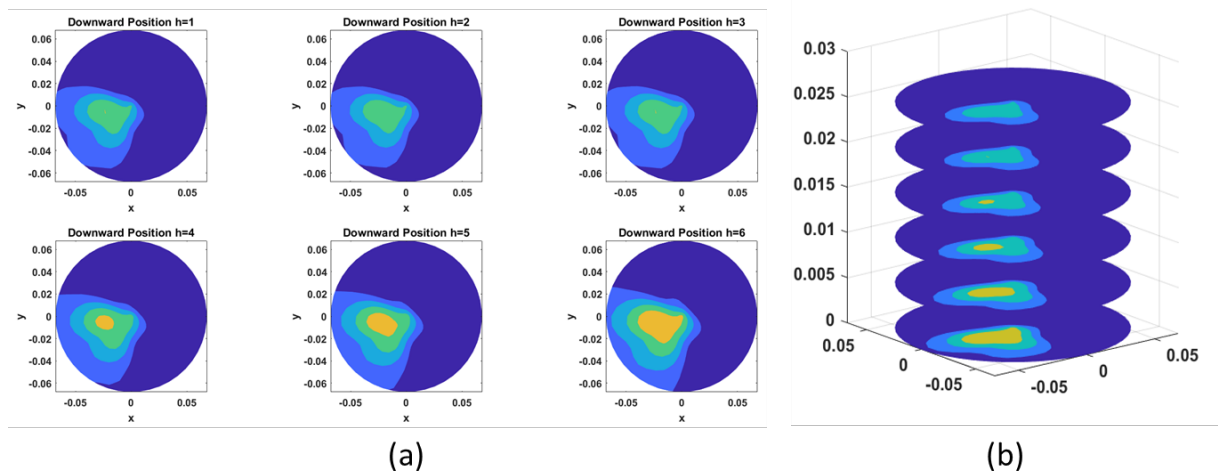


Figure 6.4: (a) Reconstructed microwave images with detected inclusion at reference planes (spiral-like acquisition Configuration-I), (b) 3D reconstructed image, Images are produced after normalization and image adjustment. Axes units are meters.

In the second scenario, which involved spiral-like configuration-II, Figure 6.5(a) shows the images reconstructed at multiple planes along the z-axis. Notably, the images reveal successful detection of the inclusion at the bottom two planes; however, there is a noticeable dimensional error present. This discrepancy in dimensions could potentially impact the accuracy of the imaging results. To gain a better understanding of the detected inclusion and its dimensional variations, Figure 6.5(b) presents the corresponding 3D visualization. This visualization allows to observe the variation in dimensions of the

inclusion, which helps in identifying and analyzing potential errors in the imaging process. The presence of a dimensional error in the detected inclusion indicates that the spiral-like configuration-II may require further refinement or adjustments to achieve more precise and accurate results. While the detection at the bottom planes is successful, addressing the dimensional error is crucial to enhance the reliability and usefulness of the imaging technique.

These findings from Figure 6.5 underscore the importance of rigorous evaluation and fine-tuning of the measurement methodologies in microwave imaging. It highlights the need for continuous research and development to optimize imaging configurations, thereby improving the accuracy and clinical utility of the technology. The results presented in Figure 6.5 provide valuable insights into the strengths and limitations of the spiral-like configuration-II. By identifying the dimensional error and analyzing the variation in inclusion dimensions through 3D visualization, efforts can be directed towards enhancing the imaging techniques for more effective medical applications, particularly in early disease detection and diagnosis.

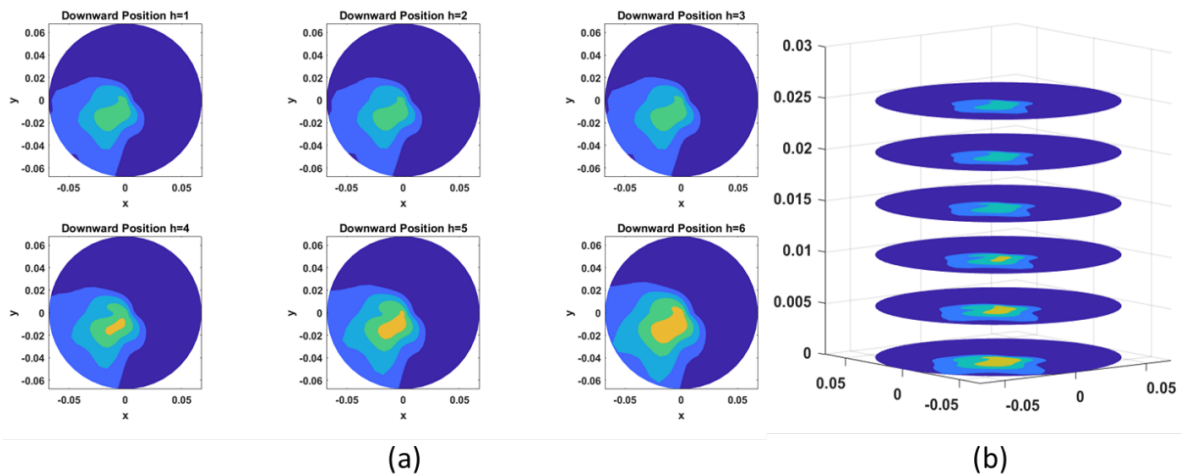


Figure 6.5: (a) Reconstructed microwave images with detected inclusion at reference planes (spiral-like acquisition configuration-II), (b) 3D reconstructed image. Images are produced after normalization and image adjustment. Axes units are meters.

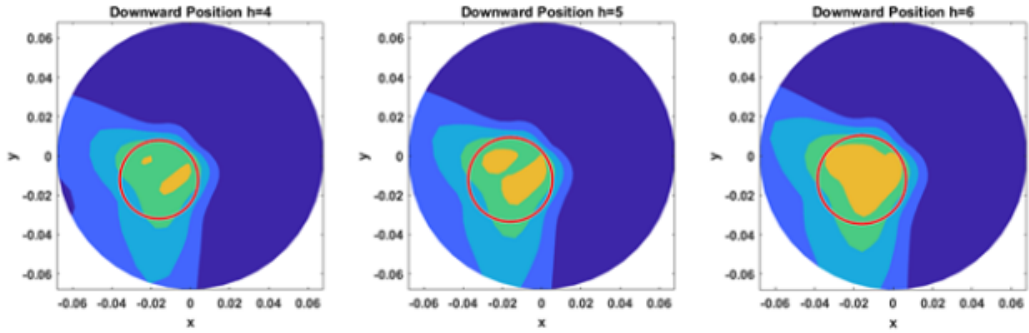
After generating the reconstructed images using the 3D imaging algorithm, a detailed analysis has been conducted for all three scenarios, namely: (i) the original setup as described in [106], (ii) spiral-like acquisition configuration-I, and (iii) spiral-like acquisition configuration-II. As per the experimental arrangement, where only the spherical part of the inclusion was filled with the fabrication mixture, the expectation was to detect the

inclusion at heights h_4 , h_5 , and h_6 . This objective was successfully achieved, as evident from Figures 6.4 and 6.5. To perform the analysis, focus was placed on the reconstructed images at heights h_4 , h_5 , and h_6 along the z -axis. Figure 6.6(a) presents the detected inclusion at these heights for the original experimental setup. The red circles in the figure represent the actual location of the inclusion, aligned with the realistic scenario of this experimental setup. Similarly, Figures 6.6(b) and 6.6(c) illustrate the detected inclusion at heights h_4 , h_5 , and h_6 for spiral-like acquisition configurations I and II, respectively. In all three figures, the diameters of the red circles, representing the actual size and location of the inclusion at multiple planes along the z -axis, remain the same.

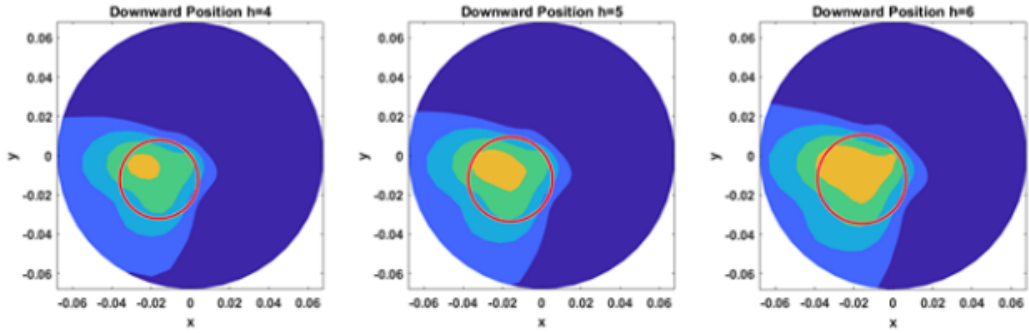
The comparative analysis of the detected inclusions among the three scenarios allows to assess the performance and accuracy of each configuration. By aligning the detected inclusion with the actual location represented by the red circles, insights into the level of precision and reliability achieved by each imaging setup are gained. The results presented in Figure 6.6 demonstrate the successful detection of the inclusion at specific heights along the z -axis for all three scenarios. This analysis provides valuable information on the capabilities and limitations of each configuration, which is essential for further improving and optimizing microwave imaging techniques for medical applications.

The calculations have been performed for the signal to clutter ratio (S/C) for all three scenarios in order to compare the results at heights h_4 , h_5 , and h_6 along the z -axis, as shown in Table 6.2. The SCRratio is determined as the ratio between the maximum intensity evaluated within the region of the inclusion and the maximum intensity outside the region of the inclusion [110]. As observed in the table, for the spiral-like acquisition configuration-I, the SCRratio at h_6 (where the inclusion has its largest diameter) drops from 10.48 dB to 9.28 dB, resulting in a difference of 1.2 dB compared to the original setup. On the other hand, for the spiral-like acquisition configuration-II, this ratio experiences a greater drop of 3.14 dB when compared to the original setup. The comparison of SCRratios provides valuable insights into the performance of each configuration in detecting the inclusion accurately and minimizing clutter or interference from surrounding regions. A higher SCRratio indicates better contrast and clarity of the detected inclusion, which is essential for reliable medical imaging.

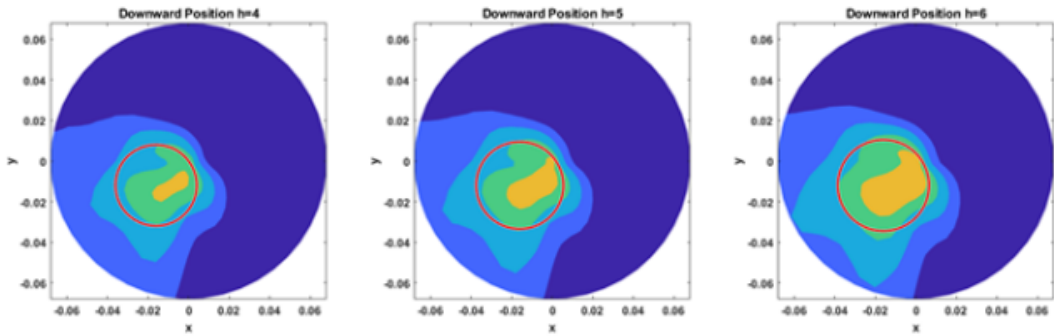
The results from Table 6.2 underscore the trade-offs associated with each acquisition configuration. While spiral-like acquisition configuration-I exhibits a smaller de-



(a)



(b)



(c)

Figure 6.6: Reconstructed microwave images with detected inclusion at h_4 , h_5 , and h_6 using: (a) original setup, (b) spiral-like acquisition configuration-I, (c) spiral-like acquisition configuration-II.

crease in SCRratio, indicating better preservation of signal quality, spiral-like acquisition configuration-II experiences a more significant drop in SCRratio, suggesting a potential decrease in imaging accuracy and clarity. These findings demonstrate the importance of carefully considering and optimizing the acquisition configurations in microwave imaging to achieve the desired balance between acquisition time reduction and imaging quality. The analysis of SCRratios contributes to the ongoing efforts in refining microwave imaging techniques for improved medical applications and disease detection.

Table 6.2: Signal to Clutter Ratio Comparison for all three scenarios.

Z_h along z -axis	Original Setup	Spiral-like Configuration-I	Spiral-like Configuration-II
$h = 4$	4.99	4.59	2.56
$h = 5$	7.48	7.04	5.94
$h = 6$	10.48	9.28	7.34

Additionally, calculations for the dimensional analysis error, as described in the previous chapter, have been performed for all three scenarios. Table 6.3 presents the dimensional error in percentage for each configuration. From the values presented in Table 6.3, it is evident that both proposed methodologies for achieving time reduction result in increased error percentages compared to the original setup. For spiral-like acquisition configuration-I, the increase in error percentage ranges from 1.4% to 3.62%. This indicates a slight to moderate increase in error when compared to the original setup, suggesting that while time reduction is achieved, there is a trade-off in terms of dimensional accuracy.

On the other hand, the spiral-like acquisition configuration-II exhibits a higher increase in error percentage, approximately 6%, compared to the original setup. This indicates a more significant impact on dimensional accuracy with this configuration, highlighting the need for further refinement and optimization to balance time reduction and dimensional precision. The dimensional analysis error is a key parameter in assessing the reliability and accuracy of the imaging results. Higher error percentages can lead to imprecise dimensional measurements, which may limit the effectiveness of microwave imaging for medical applications.

The findings from Table 6.3 emphasize the importance of carefully evaluating the trade-offs between time reduction and dimensional accuracy in microwave imaging techniques. While the proposed methodologies offer notable time savings, the increased dimensional analysis error must be carefully considered and mitigated in the design and imple-

mentation of future microwave imaging configurations. By understanding and quantifying these errors, efforts can be directed towards developing improved imaging algorithms and methodologies that strike a better balance between time efficiency and dimensional accuracy, ultimately enhancing the overall performance and clinical utility of microwave imaging for medical applications.

Table 6.3: Dimensional Analysis Error Comparison for all three scenarios.

Z_h along z -axis	Original Setup	Spiral-like Configuration-I	Spiral-like Configuration-II
$h = 4$	10.69	11.92	14.98
$h = 5$	8.91	10.79	13.06
$h = 6$	6.04	9.66	11.78

Additionally, the localization error was also calculated for all three scenarios. Table 6.4 presents the localization error values for each configuration. From the values presented in Table 6.4, it is evident that the localization error for spiral-like acquisition configuration-I is less than that of spiral-like configuration-II. The localization error is an important parameter in assessing the accuracy of the imaging process in precisely locating the 3D structured inclusion. Lower localization error values indicate a higher level of accuracy in identifying the position and dimensions of the inclusion, which is essential for reliable medical imaging and disease detection.

The results in Table 6.4 indicate that the proposed spiral-like acquisition configuration-I achieves better localization accuracy compared to configuration-II. This suggests that the first configuration is more effective in precisely identifying and localizing the inclusion within the 3D imaging domain.

Table 6.4: Localization Error Comparison for all three scenarios.

Z_h along z -axis	Original Setup	Spiral-like Configuration-I	Spiral-like Configuration-II
$h = 4$	4.81	6.59	7.29
$h = 5$	3.56	5.13	6.07
$h = 6$	2.68	3.92	5.23

In the original setup, the measurement time was 9 minutes per height, which served as the baseline for this comparison. The proposed configurations, as presented above, demonstrated an impressive measurement time reduction of approximately 50%. This significant reduction in acquisition time is a substantial achievement and a critical con-

sideration in optimizing microwave imaging techniques for practical medical applications. Through a detailed analysis encompassing various parameters, including SCR, dimensional analysis error, and localization error, valuable insights into the performance of the two proposed configurations have been gained. Based on the findings, spiral-like acquisition configuration-I emerges as the more suitable and favourable overall configuration among the two. The superiority of spiral-like acquisition configuration-I lies in its ability to achieve a relatively lower decrease in SCR compared to the original setup, indicating better preservation of signal quality. Additionally, the increase in dimensional analysis error with configuration-I is within a moderate range, demonstrating a reasonable trade-off between time reduction and dimensional accuracy.

Moreover, this meticulous evaluation of the localization error reveals that spiral-like acquisition configuration-I outperforms configuration-II in precisely identifying and localizing the 3D structured inclusion. This higher localization accuracy makes configuration-I more adept at pinpointing the exact position and dimensions of the inclusion, a crucial factor in medical imaging for accurate disease detection and diagnosis. Considering all the factors examined, spiral-like acquisition configuration-I stands out as the more favourable choice due to its ability to achieve a considerable reduction in measurement time while still maintaining satisfactory imaging performance in terms of signal quality, dimensional accuracy, and localization precision.

In addition to the two previously discussed configurations, further experimentation was conducted to explore the limits of achieving time reduction while minimizing errors. To achieve this objective, a novel spiral acquisition configuration was implemented by significantly reducing the number of Rx points to one-third of the previous configurations. Specifically, the points that have been considered includes Rx positions 1-27 for heights h_1 and h_4 , Rx positions 28-54 for heights h_2 and h_5 , and Rx positions 55-80 for heights h_3 and h_6 , utilizing only one-third of the receiving points at each plane along the z -axis.

Figure 6.7 showcases the reconstructed images resulting from this spiral acquisition configuration at multiple planes along the z -axis. Through this approach, the aim was to determine the feasibility of achieving further time reduction while maintaining acceptable levels of imaging accuracy. By reducing the number of Rx points, the aim was to strike a balance between time efficiency and imaging performance. This experiment allowed the exploration of the trade-offs between reduced acquisition time and potential increases in

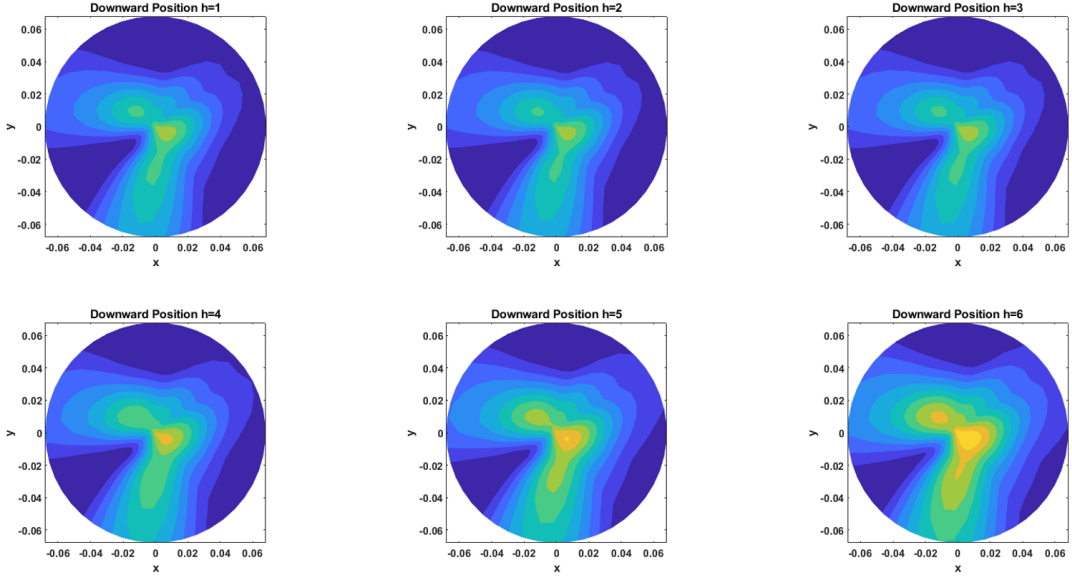


Figure 6.7: Reconstructed images resulting from the novel spiral acquisition configuration at multiple planes along the z -axis.

errors related to dimensional analysis, localization, and SCR.

The findings from this experimentation will further contribute to the optimization of microwave imaging techniques for medical applications, enabling to identify the optimal configuration that achieves the best compromise between time reduction and imaging accuracy. In conclusion, the exploration of the spiral acquisition configuration with reduced Rx points serves as a significant step in refining microwave imaging methodologies.

Upon careful examination of the obtained images and a thorough analysis of the quantification parameters, it is evident that the proposed methodology with reduced Rx points ($1/3$ of the previous configurations) did not yield successful results in this scenario. The experimental findings indicate significant challenges and limitations associated with this specific setup. Particularly noteworthy is the impact on SCR at height $h=6$, where the inclusion is at its largest diameter. The reduction in SCR is notable, dropping by 6.5 dB compared to the original setup and by 4 dB compared to spiral-like acquisition configuration-I. This decrease in SCR reflects a significant degradation in the quality and clarity of the imaging results, affecting the ability to distinguish the inclusion from clutter or noise in the acquired data.

Furthermore, other quantification parameters have also been evaluated, revealing an increase in the dimensional analysis error by 20% and the localization error by 17 mm. Such substantial increases in error percentages underscore the limitations of reducing the

number of Rx points to 1/3. These findings highlight the significant trade-offs between time reduction and imaging accuracy in this particular scenario. The observed challenges and increased error percentages necessitate careful consideration and caution when implementing reduced Rx points as a means of achieving time reduction. While reducing Rx points may lead to faster acquisition times, it comes at the cost of compromised imaging quality and accuracy, as evident from the decreased SCR and higher error percentages.

In conclusion, the experimentation with reduced Rx points in this scenario has brought to light the limitations and practical challenges associated with striking a balance between time reduction and imaging accuracy [111].

6.5 Summary

In this chapter, an investigation was embarked on to explore the feasibility of employing a spiral-like acquisition strategy for 3D microwave imaging based on Huygens' principle. The primary objective was to achieve significant time reduction in the measurement process. To achieve this goal, a three-layer cylindrical phantom with a 3D structured inclusion, exhibiting varying dielectric properties, was fabricated. The implementation of the spiral-like acquisition was performed through two distinct configurations on multiple planes along the z -axis.

In the first scenario (configuration I), the signals were recorded by considering the first 40 Rx points for h_1 and the second set of 40 Rx points (from 41 to 80) for h_2 , and so on. The first 40 points were utilized for h_3 and h_5 , while the second half was used for h_4 and h_6 . For the second scenario (configuration II), the complex S21 measurements were recorded by evaluating 40 Rx points with alternating 20 Rx points. Specifically, Rx points 1 to 20 and 40 to 60 for h_1 , h_3 , and h_5 were considered, while Rx points 21 to 40 and 61 to 80 were used for h_2 , h_4 , and h_6 .

The outcomes of this investigation demonstrated that both scenarios presented promising image reconstructions, accompanied by a remarkable reduction in measurement time of up to 50%. This substantial reduction in acquisition time was achieved without compromising the overall quality of the reconstructed images. However, it is essential to consider the impact of this time reduction on quantification parameters such as the SCR and the dimensional analysis and localization errors. The findings revealed that the 50% mea-

surement time reduction resulted in a maximum 3.2 dB decrease in the SCR and a slight increase of approximately 3.5% in dimensional analysis and localization errors. These deviations signify a reasonable trade-off between time efficiency and imaging accuracy.

In addition, the exploration was extended to include the utilization of only one-third of the receiving points in the spiral-like acquisition. This approach was introduced to test the limits of time reduction. However, the results showed that this configuration led to further increases in error percentages, thereby highlighting the challenges of achieving significant time reduction while preserving imaging accuracy.

In conclusion, this research showcased the potential of spiral-like acquisition strategies for 3D microwave imaging to achieve remarkable time reduction without compromising image quality significantly. While this reduction in measurement time holds great promise for practical medical applications, it is crucial to carefully consider the impact on quantification parameters to strike an optimal balance between time efficiency and imaging accuracy. The insights gained from this study will inform future advancements in microwave imaging methodologies, guiding towards optimizing acquisition configurations to enable precise and efficient medical imaging for disease detection and diagnosis.

Chapter 7

Conclusions and Future Work

7.1 Conclusions

The traditional medical imaging technologies face limitations related to cost, accessibility, and operator expertise, the research highlights the potential of MWI using UWB technology as a safer and cost-effective alternative for early cancer detection. This study emphasizes the importance of advancements in MWI systems for detecting breast, lung, and brain cancers, addressing challenges to promote wider clinical adoption and improve patient outcomes. This research journey has illuminated significant breakthroughs in the domain of MWI, underscoring its pivotal role in critical medical applications. Through methodical exploration and hands-on experimentation, insights of paramount importance have been unraveled that could revolutionize the landscape of medical diagnostics.

In conclusion, this research presented a comprehensive overview of the experimental setup for the proposed MWI technology, detailing crucial hardware and parameters. The hardware, including UWB antennas, VNA, rotating table, and stand, were concisely explained, as was the setup within the anechoic chamber. The MWI experimental setup was arranged inside anechoic chamber and executed using fabricated phantom to emulate lung COVID-19 infections. Both types of phantoms play a crucial role in substantiating the validity and applicability of the research findings. The research delved into the HP-based MWI algorithm utilized to differentiate healthy and malignant tissues based on their dielectric properties. UWB vertically polarized antennas, connected to VNA, recorded complex S21 signals for different transmitting positions, processed through the HP-based imaging algorithm. Images successfully detect the inclusion, validated by a calculated

SCR of 7 dB. This result highlights the potential of MWI in disease detection, with SCR serving as a key performance metric validating the objectives of the proposed research.

Furthermore, the second phantom represents a more realistic model of the lung, aiming to accurately mimic actual lung tissues and tumors, thus posing a challenging context for lesion detection. To achieve this objective, an amplifier was strategically utilized to augment signal power, mitigating the inherent power loss of the antenna caused by the substantial dimensions of the realistic phantom. The size of the mimicked lesion has been intentionally increased, in alignment with the experiment's goal of validating the methodology within a realistic and complex scenario. The processed measurements utilizing the HP-based imaging algorithm successfully identify the inclusion, thereby illustrating a notable advancement in the field and attaining a significant milestone in the research endeavor. Image artefact removal and normalization further enhance results, showcasing a practical approach. Promising results, validated by quantification parameters like SCR and dimensional analysis error, underscore the algorithm's efficacy.

The 3D imaging algorithm, developed on the basis of the Huygens principle, reveals promising outcomes in visualizing internal structures. Its effectiveness in navigating complex scenarios with diverse dielectric properties signifies the successful accomplishment of the research's primary aim. Validated through fabricated phantoms, this algorithm demonstrates its efficacy, particularly in complex scenarios. The algorithm's ability to handle multilayered structures, even with varying dielectric properties, adds to its novelty. This research successfully realizes the main goal of visualizing detected inclusions in 3D, showcasing its potential for accurate diagnostic imaging. Metrics such as dimensional analysis and localization errors contribute to the assessment of its performance.

The investigation extends its scope to spiral-like acquisition strategies for 3D microwave imaging. With a focus on time reduction, a three-layer cylindrical phantom with a structured inclusion was employed. The outcomes highlight significant time reduction of up to 50%, without compromising image quality. This achievement aligns with practical medical applications, offering an efficient approach without sacrificing accuracy. The research underscores the importance of considering quantification parameters and balancing time efficiency with imaging accuracy. This study provides insights guiding future microwave imaging advancements for disease detection and diagnosis, with metrics such as SCR and error percentages serving as benchmarks for success.

In conclusion, this research sets a solid foundation for the evolution of MWI as a transformative medical imaging technology. The journey taken not only exemplifies the novel achievements but also underscores the metrics that will steer the course of future developments, contributing to enhanced disease detection and diagnostics. As venturing forward, the benchmarks established here remain instrumental in guiding the path toward more efficient and accurate medical imaging solutions.

7.2 Recommendations for Future Work

The proposed MWI methodology based on HP has demonstrated promising results in lesion detection, as evidenced by the research showcasing the capability of this methodology through a wide range of experiments utilizing fabricated phantoms. The visualization of detected lesions in 3D, along with insights into their varying dimensions, further supports this methodology's potential. However, there is still room for improvement within this approach.

7.2.1 Enhancement Prospects in Lung Lesion Detection

In the context of the lung lesion detection via realistic multi-layer chest phantom as presented earlier showcase the possibility for enhancement in several ways. One possibility involves the exploration of UWB antennas with robust penetration capabilities and strong signal strength. Another prospect is the automation of measurement recording, aligned with phantom rotation, akin to the principles of MammoWave, to achieve heightened accuracy. Furthermore, with the utilization of advanced UWB antennas, it is conceivable to decrease inclusion size, contributing to a more realistic simulation. Additionally, incorporating the dynamics of lung inflation and deflation into the simulation could replicate dielectric properties and amplify the effectiveness of the imaging algorithm. Furthermore, as a prospect for future research, following the implementation and thorough testing of the previously mentioned methods and the validation of HP-based MWI effectiveness in detecting lung lesions through extensive experiments, the possibility arises to create an innovative, fast, and accurate device like MammoWave. This potential device could include automated experimental setups and improved, validated hardware, representing a significant breakthrough in lung lesion screening, offering safe assessments without any

age restrictions.

7.2.2 Advancements in 3D Visualization

In the realm of 3D visualization, the MWI device MammoWave takes centre stage. Experiments were conducted across multiple planes along the z-axis as explained provides validation for MammoWave's ability to offer dimensional insights into detected lesions, confirmed through SCR ratio, localization error, and image quantification methods. Building upon these achievements, a multitude of opportunities beckon for exploration and implementation to further enhance results. First and foremost, optimizing the proposed 3D MWI algorithm is paramount, aiming to minimize errors while substantiating its performance with quantifiable parameters. Furthermore, there is the potential to elevate the sophistication of the 3D algorithm to calculate inclusion resolution across multiple z-axis planes, which presents a promising avenue for advancement. Moreover, the next phase of development should encompass the visualization of detected inclusions in various dimensions, allowing for a 3D representation of the entire volume. This capability would enable the examination of any cross-section along any plane, thus providing a more detailed view of the data.

7.2.3 Strategies for Improving Time Reduction in Microwave Imaging

Notably, while the outlined time reduction strategy offers efficiency gains, it also introduces some compromise in terms of increased errors. Potential strategies include adapting the measurement schematic and antenna rotation along the z-axis in a spiral-like configuration, aimed at diminishing errors and enhancing overall performance. Meanwhile, in future there is possibility of optimizing the hardware along with the software to enhance the reconstructed images with minimal errors.

References

- [1] J. H. Scatliff and P. J. Morris, “From roentgen to magnetic resonance imaging: The history of medical imaging,” *North Carolina Medical Journal*, vol. 75, no. 2, pp. 123–125, 2014.
- [2] A. Paterson, L. F. Donnelly, and D. P. Frush, “The pros and cons of imaging options,” *Contemporary Pediatrics*, vol. 18, no. 4, pp. 73–94, 2001.
- [3] Z. Zhekova-Maradzhieva, B. Velchovska, A. Uzunov, E. Ivanova, D. Petrova, M. Yordanova, and G. Valchev, “The effect of x-ray radiation on the human body: Pros and cons. radiation protection in medical imaging and radiotherapy,” *Scripta Scientifica Salutis Publicae*, vol. 2, pp. 161–165, 2017.
- [4] M. E. Ladd, P. Bachert, M. Meyerspeer, E. Moser, A. M. Nagel, D. G. Norris, S. Schmitter, O. Speck, S. Straub, and M. Zaiss, “Pros and cons of ultra-high-field mri/mrs for human application,” *Progress in Nuclear Magnetic Resonance Spectroscopy*, vol. 109, pp. 1–50, 2018.
- [5] G. Katti, S. A. Ara, and A. Shireen, “Magnetic resonance imaging (mri)—a review,” *International Journal of Dental Clinics*, vol. 3, no. 1, pp. 65–70, 2011.
- [6] G. Ross, “Transmission and reception system for generating and receiving base-band pulse duration pulse signals without distortion for short base-band communication system.” Google Patents, Apr 17 1973. US Patent 3,728,632.
- [7] I. Oppermann, M. Hämäläinen, and J. Iinatti, *UWB: Theory and Applications*. John Wiley & Sons, 2004.
- [8] R. S. Kshetrimayum, “An introduction to uwb communication systems,” *IEEE Potentials*, vol. 28, no. 2, pp. 9–13, 2009.

- [9] Y. Rahayu, T. A. Rahman, R. Ngah, and P. S. Hall, “Ultra wideband technology and its applications,” in *2008 5th IFIP International Conference on Wireless and Optical Communications Networks (WOCN’08)*, pp. 1–5, 2008.
- [10] K. Siwiak and D. McKeown, *Ultra-Wideband Radio Technology*. John Wiley & Sons, 2004.
- [11] J. Pan, “Medical applications of ultra-wideband (uwb),” *Survey Paper*, 2007.
- [12] A. Vispa, L. Sani, M. Paoli, A. Bigotti, G. Raspa, N. Ghavami, S. Caschera, M. Ghavami, M. Duranti, and G. Tiberi, “Uwb device for breast microwave imaging: Phantom and clinical validations,” *Measurement*, vol. 146, pp. 582–589, 2019.
- [13] S. Semenov, “Microwave tomography: Review of the progress towards clinical applications,” *Philosophical Transactions of the Royal Society A: Mathematical, Physical and Engineering Sciences*, vol. 367, no. 1900, pp. 3021–3042, 2009.
- [14] M. F. Rahiman, T. T. W. Kiat, S. P. Jack, and R. A. Rahim, “Microwave tomography application and approaches—a review,” *J. Teknol*, vol. 73, no. 3, pp. 133–138, 2015.
- [15] M. A. Elahi, B. Lavoie, E. Porter, M. Olavini, E. Jones, E. Fear, and M. O’Halloran, “Comparison of radar-based microwave imaging algorithms applied to experimental breast phantoms,” in *2017 XXXIInd General Assembly and Scientific Symposium of the International Union of Radio Science (URSI GASS)*, pp. 1–4, 2017.
- [16] H. B. Lim, N. T. T. Nhung, E.-P. Li, and N. D. Thang, “Confocal microwave imaging for breast cancer detection: Delay-multiply-and-sum image reconstruction algorithm,” *IEEE Transactions on Biomedical Engineering*, vol. 55, no. 6, pp. 1697–1704, 2008.
- [17] X. Li, E. J. Bond, B. D. Van Veen, and S. C. Hagness, “An overview of ultra-wideband microwave imaging via space-time beamforming for early-stage breast-cancer detection,” *IEEE Antennas and Propagation Magazine*, vol. 47, no. 1, pp. 19–34, 2003.

- [18] M. D. Hossain and A. S. Mohan, “Cancer detection in highly dense breasts using coherently focused time-reversal microwave imaging,” *IEEE Transactions on Computational Imaging*, vol. 3, no. 4, pp. 928–939, 2017.
- [19] M. I. Patel, A. M. Lopez, W. Blackstock, K. Reeder-Hayes, A. Moushey, J. Phillips, and W. Tap, “Cancer disparities and health equity: A policy statement from the american society of clinical oncology,” *Journal of Clinical Oncology*, vol. 38, no. 29, p. 3439, 2020.
- [20] “Cancer research uk.” <https://www.cancerresearchuk.org/>.
- [21] F. Bray, J. Ferlay, I. Soerjomataram, R. L. Siegel, L. A. Torre, and A. Jemal, “Global cancer statistics 2018: Globocan estimates of incidence and mortality worldwide for 36 cancers in 185 countries,” *CA: A Cancer Journal for Clinicians*, vol. 68, no. 6, pp. 394–424, 2018.
- [22] “Breast cancer: Prevention and diagnosis.” <https://www.who.int/cancer/prevention/diagnosis-screening/breast-cancer/en/>.
- [23] M. M. Beg and M. Jain, “An analysis of the methods employed for breast cancer diagnosis,” *arXiv Preprint arXiv:1206.3777*, 2012.
- [24] L. Xing, N. W. Todd, L. Yu, H. Fang, and F. Jiang, “Early detection of squamous cell lung cancer in sputum by a panel of microRNA markers,” *Modern Pathology*, vol. 23, no. 8, pp. 1157–1164, 2010.
- [25] V. Anitha and S. Murugavalli, “Brain tumour classification using two-tier classifier with adaptive segmentation technique,” *IET Computer Vision*, vol. 10, no. 1, pp. 9–17, 2016.
- [26] M. Bialkowski and Y. Wang, “Uwb cylindrical microwave imaging system employing virtual array antenna concept for background effect removal,” *Microwave and Optical Technology Letters*, vol. 53, no. 5, pp. 1100–1104, 2011.
- [27] E. C. Fear, J. Bourqui, C. Curtis, D. Mew, B. Docktor, and C. Romano, “Microwave breast imaging with a monostatic radar-based system: A study of application to patients,” *IEEE Transactions on Microwave Theory and Techniques*, vol. 61, no. 5, pp. 2119–2128, 2013.

- [28] S. Kwon, S. Lee, *et al.*, “Recent advances in microwave imaging for breast cancer detection,” *International Journal of Biomedical Imaging*, vol. 2016, 2016.
- [29] M. Islam, M. Mahmud, M. T. Islam, S. Kibria, and M. Samsuzzaman, “A low-cost and portable microwave imaging system for breast tumor detection using uwb directional antenna array,” *Scientific Reports*, vol. 9, no. 1, p. 15491, 2019.
- [30] L. Sani, N. Ghavami, A. Vispa, M. Paoli, G. Raspa, M. Ghavami, F. Sacchetti, E. Vannini, S. Ercolani, A. Saracini, *et al.*, “Novel microwave apparatus for breast lesions detection: Preliminary clinical results,” *Biomedical Signal Processing and Control*, vol. 52, pp. 257–263, 2019.
- [31] O. J. Babarinde and M. Jamlos, “Uwb microwave imaging for lung tumor detection in a thorax model,” in *2014 IEEE Symposium on Wireless Technology and Applications (ISWTA)*, pp. 130–133, IEEE, 2014.
- [32] A. Zamani and A. Abbosh, “Frequency domain artifact removal technique for multistatic microwave head imaging,” in *2015 International Symposium on Antennas and Propagation (ISAP)*, pp. 1–3, IEEE, 2015.
- [33] A. Alhawari, “Lung tumour detection using ultra-wideband microwave imaging approach,” *Journal of Fundamental and Applied Sciences*, vol. 10, no. 2, 2018.
- [34] B. Khalesi, B. Khalid, N. Ghavami, S. Dudley, M. Ghavami, and G. Tiberi, “Microwave imaging for lung covid-19 infection detection through Huygens principle,” in *2021 Photonics & Electromagnetics Research Symposium (PIERS)*, pp. 2885–2891, IEEE, 2021.
- [35] H. Zhang, B. Flynn, A. T. Erdogan, and T. Arslan, “Microwave imaging for brain tumour detection using an uwb vivaldi antenna array,” in *2012 Loughborough Antennas & Propagation Conference (LAPC)*, pp. 1–4, IEEE, 2012.
- [36] H. Gupta, V. Maheshwari, and V. V. Thakery, “Brain tumor detection by microwave imaging using planar antenna,” *International Journal of Bio-Science and Bio-Technology*, vol. 8, no. 5, pp. 201–210, 2016.
- [37] B. Sohani, B. Khalesi, N. Ghavami, M. Ghavami, S. Dudley, A. Rahmani, and G. Tiberi, “Detection of haemorrhagic stroke in simulation and realistic 3-d human

- head phantom using microwave imaging,” *Biomedical Signal Processing and Control*, vol. 61, p. 102001, 2020.
- [38] H. G. Schantz, “Bottom fed planar elliptical uwb antennas,” in *IEEE Conference on Ultra Wideband Systems and Technologies, 2003*, pp. 219–223, IEEE, 2003.
- [39] H. Schantz, “Radiation efficiency of uwb antennas,” *IEEE Conference on Ultra Wideband Systems and Technologies*, pp. 351–355, 2002.
- [40] H. Schantz, “Standard gain uwb planar horn antennas,” *IEEE Conference on Ultra Wideband Systems and Technologies*, pp. 370–374, 2012.
- [41] N. Ghavami, G. Tiberi, D. Edwards, and A. Monorchio, “Uwb microwave imaging of objects with canonical shape,” *IEEE Transactions on Antennas and Propagation*, vol. 60, no. 1, pp. 231–239, 2009.
- [42] N. Ghavami, G. Edwards, D.J.and Tiberi, and G. Manara, “Huygens principle based technique for microwave imaging of objects with inclusions,” *International Conference on Electromagnetics in Advanced Applications*, pp. 1044–1047, 2011.
- [43] G. Tiberi, N. Ghavami, D. Edwards, and A. Monorchio, “Ultrawideband microwave imaging of cylindrical objects with inclusions,” *IET Microwaves, Antennas & Propagation*, vol. 5, no. 12, pp. 1440–1446, 2011.
- [44] C. Huang, Y. Wang, X. Li, L. Ren, J. Zhao, Y. Hu, L. Zhang, G. Fan, J. Xu, X. Gu, *et al.*, “Clinical features of patients infected with 2019 novel coronavirus in wuhan, china,” *The Lancet*, vol. 395, no. 10223, pp. 497–506, 2020.
- [45] H. Shi, X. Han, N. Jiang, Y. Cao, O. Alwalid, J. Gu, Y. Fan, and C. Zheng, “Radiological findings from 81 patients with covid-19 pneumonia in wuhan, china: A descriptive study,” *The Lancet Infectious Diseases*, vol. 20, no. 4, pp. 425–434, 2020.
- [46] R. C. Conceição, J. J. Mohr, M. O’Halloran, *et al.*, *An Introduction to Microwave Imaging for Breast Cancer Detection*. Springer, 2016.
- [47] S. Ahdi Rezaeieh, A. Zamani, K. Bialkowski, and A. Abbosh, “Novel microwave torso scanner for thoracic fluid accumulation diagnosis and monitoring,” *Scientific Reports*, vol. 7, no. 1, p. 304, 2017.

- [48] S. N. Muhammad, M. M. Isa, and F. Jamlos, “Review article of microwave imaging techniques and dielectric properties for lung tumor detection,” in *AIP Conference Proceedings*, vol. 2203, AIP Publishing, 2020.
- [49] X. Lin, Z. Gong, Y. Ding, Y. Chen, P. A. V. Sosa, and M. J. V. Sosa, “Feasibility study of detection of coronavirus disease 2019 with microwave medical imaging,” in *2021 15th European Conference on Antennas and Propagation (EuCAP)*, pp. 1–4, IEEE, 2021.
- [50] P. A. Hasgall, F. Di Gennaro, C. Baumgartner, E. Neufeld, B. Lloyd, M. Gosselin, D. Payne, A. Klingenböck, and N. Kuster, “It’s database for thermal and electromagnetic parameters of biological tissues,” *Version 4.0*, 2018.
- [51] S. Gabriel, R. Lau, and C. Gabriel, “The dielectric properties of biological tissues: Iii. parametric models for the dielectric spectrum of tissues,” *Physics in Medicine & Biology*, vol. 41, no. 11, p. 2271, 1996.
- [52] P. M. Meaney, C. J. Fox, S. D. Geimer, and K. D. Paulsen, “Electrical characterization of glycerin: Water mixtures: Implications for use as a coupling medium in microwave tomography,” *IEEE Transactions on Microwave Theory and Techniques*, vol. 65, no. 5, pp. 1471–1478, 2017.
- [53] Zurich MedTech AG, “Validation hardware - tle5c-24-2450.”
- [54] E. C. Fear, X. Li, S. C. Hagness, and M. A. Stuchly, “Confocal microwave imaging for breast cancer detection: Localization of tumors in three dimensions,” *IEEE Transactions on Biomedical Engineering*, vol. 49, no. 8, pp. 812–822, 2002.
- [55] F. Bray, J. Ferlay, I. Soerjomataram, R. L. Siegel, L. A. Torre, and A. Jemal, “Global cancer statistics 2018: Globocan estimates of incidence and mortality worldwide for 36 cancers in 185 countries,” *CA: A Cancer Journal for Clinicians*, vol. 68, no. 6, pp. 394–424, 2018.
- [56] S. Blandin Knight, P. Crosbie, H. Balata, J. Chudziak, T. Hussell, and C. Dive, “Progress and prospects of early detection in lung cancer. open biol 7,” 2017.
- [57] J. K. Field, S. W. Duffy, D. R. Baldwin, K. E. Brain, A. Devaraj, T. Eisen, B. A. Green, J. A. Holemans, T. Kavanagh, K. M. Kerr, *et al.*, “The uk lung cancer

- screening trial: A pilot randomised controlled trial of low-dose computed tomography screening for the early detection of lung cancer,” *Health Technology Assessment (Winchester, England)*, vol. 20, no. 40, p. 1, 2016.
- [58] R. C. Conceição, J. J. Mohr, M. O’Halloran, *et al.*, *An Introduction to Microwave Imaging for Breast Cancer Detection*. Springer, 2016.
- [59] S. Ahdi Rezaeieh, A. Darvazehban, A. S. Janani, and A. M. Abbosh, “Electromagnetic torso scanning: A review of devices, algorithms, and systems,” *Biosensors*, vol. 11, no. 5, p. 135, 2021.
- [60] S. N. Muhammad, M. M. Isa, and F. Jamlos, “Review article of microwave imaging techniques and dielectric properties for lung tumor detection,” in *AIP Conference Proceedings*, vol. 2203, AIP Publishing, 2020.
- [61] B. Khalesi, B. Khalid, N. Ghavami, G. Raspa, M. Ghavami, S. Dudley-McEvoy, and G. Tiberi, “A microwave imaging procedure for lung lesion detection: Preliminary results on multilayer phantoms,” *Electronics*, vol. 11, no. 13, p. 2105, 2022.
- [62] SPEAG, “Multilayer chest phantom v1.”
- [63] C. Gabriel, S. Gabriel, and Y. Corthout, “The dielectric properties of biological tissues: I. literature survey,” *Physics in medicine & biology*, vol. 41, no. 11, p. 2231, 1996.
- [64] T. A. Shah and S. S. Guraya, “Breast cancer screening programs: Review of merits, demerits, and recent recommendations practiced across the world,” *Journal of microscopy and ultrastructure*, vol. 5, no. 2, pp. 59–69, 2017.
- [65] T. H.-H. Chen, A. M.-F. Yen, J. C.-Y. Fann, P. Gordon, S. L.-S. Chen, S. Y.-H. Chiu, C.-Y. Hsu, K.-J. Chang, W.-C. Lee, K. G. Yeoh, *et al.*, “Clarifying the debate on population-based screening for breast cancer with mammography: a systematic review of randomized controlled trials on mammography with bayesian meta-analysis and causal model,” *Medicine*, vol. 96, no. 3, 2017.
- [66] J. A. Hanley, A. Hannigan, and K. M. O’Brien, “Mortality reductions due to mammography screening: Contemporary population-based data,” *PloS one*, vol. 12, no. 12, p. e0188947, 2017.

- [67] R. C. RODRIGUES, H. L. DEL PUERTO, FERREIRA, F. ALVES, and A. S. MARTINS, “Breast cancer: Prognostic evaluation perspectives by transcription factors using histochemical immunolocalizers and functional genomics.,” *NBC-Periódico Científico do Núcleo de Biociências*, vol. 10, no. 20, 2020.
- [68] J. Ferlay, M. Ervik, F. Lam, M. Colombet, L. Mery, M. Piñeros, A. Znaor, I. Soerjomataram, and F. Bray, “Global cancer observatory: cancer today. lyon, france: international agency for research on cancer,” 2018.
- [69] B. C. S. Consortium *et al.*, “sensitivity, specificity, and false negative rate for 1,682,504 screening mammography examinations from 2007-2013,” *BCSC, National Cancer Institute*, vol. 31, 2014.
- [70] N. K. Stout, S. J. Lee, C. B. Schechter, K. Kerlikowske, O. Alagoz, D. Berry, D. S. Buist, M. Cevik, G. Chisholm, H. J. De Koning, *et al.*, “Benefits, harms, and costs for breast cancer screening after us implementation of digital mammography,” *Journal of the National Cancer Institute*, vol. 106, no. 6, p. dju092, 2014.
- [71] H. D. Nelson, M. Pappas, A. Cantor, J. Griffin, M. Daeges, and L. Humphrey, “Harms of breast cancer screening: systematic review to update the 2009 us preventive services task force recommendation,” *Annals of internal medicine*, vol. 164, no. 4, pp. 256–267, 2016.
- [72] N. K. Nikolova, “Microwave imaging for breast cancer,” *IEEE microwave magazine*, vol. 12, no. 7, pp. 78–94, 2011.
- [73] M. A. Aldhaeabi, K. Alzoubi, T. S. Almoneef, S. M. Bamatraf, H. Attia, and O. M. Ramahi, “Review of microwaves techniques for breast cancer detection,” *Sensors*, vol. 20, no. 8, p. 2390, 2020.
- [74] P. M. Meaney, M. W. Fanning, T. Raynolds, C. J. Fox, Q. Fang, C. A. Kogel, S. P. Poplack, and K. D. Paulsen, “Initial clinical experience with microwave breast imaging in women with normal mammography,” *Academic radiology*, vol. 14, no. 2, pp. 207–218, 2007.
- [75] N. K. Stout, S. J. Lee, C. B. Schechter, K. Kerlikowske, O. Alagoz, D. Berry, D. S. Buist, M. Cevik, G. Chisholm, H. J. De Koning, *et al.*, “Time-domain wideband

- adaptive beamforming for radar breast imaging,” *IEEE Transactions on Antennas and Propagation*, vol. 63, no. 4, pp. 1725–1735, 2015.
- [76] A. Vispa, L. Sani, M. Paoli, A. Bigotti, G. Raspa, N. Ghavami, M. Ghavami, and G. Tiberi, “Uwb device for microwave imaging: Validation through phantoms,” in *2019 13th European Conference on Antennas and Propagation (EuCAP)*, pp. 1–4, IEEE, 2019.
- [77] L. Sani, A. Vispa, R. Loretoni, M. Duranti, N. Ghavami, D. Alvarez Sánchez-Bayuela, S. Caschera, M. Paoli, A. Bigotti, M. Badia, *et al.*, “Breast lesion detection through mammowave device: Empirical detection capability assessment of microwave images’ parameters,” *Plos one*, vol. 16, no. 4, p. e0250005, 2021.
- [78] Copper Mountain Technologies, “M5065 2-port 6.5 ghz vna analyzer.”
- [79] D. Sánchez-Bayuela, N. Ghavami, G. Tiberi, L. Sani, A. Vispa, A. Bigotti, G. Raspa, M. Badia, L. Papini, M. Ghavami, *et al.*, “A multicentric, single arm, prospective, stratified clinical investigation to evaluate mammowave’s ability in breast lesions detection,” *Plos one*, vol. 18, no. 7, p. e0288312, 2023.
- [80] G. Tiberi, B. Khalesi, B. Sohani, S. Dudley, M. Ghavami, and N. Ghavami, “Phase-weighted uwb imaging through huygens principle,” in *2019 PhotonIcs & Electromagnetics Research Symposium-Spring (PIERS-Spring)*, pp. 949–952, IEEE, 2019.
- [81] N. Ghavami, G. Tiberi, M. Ghavami, S. Dudley, and M. Lane, “Huygens principle based uwb microwave imaging method for skin cancer detection,” in *2016 10th International Symposium on Communication Systems, Networks and Digital Signal Processing (CSNDSP)*, pp. 1–4, IEEE, 2016.
- [82] N. Ghavami, G. Tiberi, M. Ghavami, S. Dudley, and M. Lane, “Huygens principle based uwb microwave imaging method for skin cancer detection,” in *2016 10th International Symposium on Communication Systems, Networks and Digital Signal Processing (CSNDSP)*, pp. 1–4, IEEE, 2016.
- [83] UBTech Medical (Srl) Italy., “Mammowave - breast cancer detection system.”

- [84] G. Tiberi, L. Sani, N. Ghavami, M. Paoli, A. Vispa, G. Raspa, E. Vannini, A. Saracini, M. Duranti, *et al.*, “Sensitivity assessment of a microwave apparatus for breast cancer detection,” European Congress of Radiology-ECR 2018, 2018.
- [85] B. Khalesi, B. Sohani, N. Ghavami, M. Ghavami, S. Dudley, and G. Tiberi, “Free-space operating microwave imaging device for bone lesion detection: A phantom investigation,” *IEEE Antennas and Wireless Propagation Letters*, vol. 19, no. 12, pp. 2393–2397, 2020.
- [86] N. Ghavami, M. Badia, L. Sani, G. Raspa, D. Á. Sánchez-Bayuela, A. Vispa, A. Bigotti, L. Papini, M. Cosottini, M. Ghavami, *et al.*, “Radar-based imaging through strokewave device: Preliminary experimental results,” in *2023 17th European Conference on Antennas and Propagation (EuCAP)*, pp. 1–4, IEEE, 2023.
- [87] W. A. Kalender, *Computed tomography: fundamentals, system technology, image quality, applications*. John Wiley & Sons, 2011.
- [88] K. Kim and H. Choi, “High-efficiency high-voltage class f amplifier for high-frequency wireless ultrasound systems,” *PLoS One*, vol. 16, no. 3, p. e0249034, 2021.
- [89] E. C. Fear, X. Li, S. C. Hagness, and M. A. Stuchly, “Confocal microwave imaging for breast cancer detection: Localization of tumors in three dimensions,” *IEEE Transactions on biomedical engineering*, vol. 49, no. 8, pp. 812–822, 2002.
- [90] R. Chandra, I. Balasingham, H. Zhou, and R. M. Narayanan, “Medical microwave imaging and analysis,” in *Medical Image Analysis and Informatics*, pp. 451–466, CRC Press, 2017.
- [91] S. Semenov, “Microwave tomography: review of the progress towards clinical applications,” *Philosophical Transactions of the Royal Society A: Mathematical, Physical and Engineering Sciences*, vol. 367, no. 1900, pp. 3021–3042, 2009.
- [92] M. S. Goyal and V. S. Kushwah, “Study of uwb wireless communication for recent medical applications,” *For Healthcare Professionals: Scope and Opportunities*, p. 144, 2020.

- [93] B. Allen, A. Brown, K. Schwieger, E. Zimmermann, W. Q. Malik, D. J. Edwards, L. Ouvry, and I. Oppermann, “Ultra wideband: Applications, technology and future perspectives,” international workshop on convergent technologies (IWCT), 2005.
- [94] N. K. Nikolova, “Microwave imaging for breast cancer,” *IEEE microwave magazine*, vol. 12, no. 7, pp. 78–94, 2011.
- [95] A. W. Preece, I. Craddock, M. Shere, L. Jones, and H. L. Winton, “Maria m4: clinical evaluation of a prototype ultrawideband radar scanner for breast cancer detection,” *Journal of Medical Imaging*, vol. 3, no. 3, pp. 033502–033502, 2016.
- [96] M. Guardiola, S. Capdevila, J. Romeu, and L. Jofre, “3-d microwave magnitude combined tomography for breast cancer detection using realistic breast models,” *IEEE antennas and wireless propagation letters*, vol. 11, pp. 1622–1625, 2012.
- [97] T. M. Grzegorzczak, P. M. Meaney, P. A. Kaufman, K. D. Paulsen, *et al.*, “Fast 3-d tomographic microwave imaging for breast cancer detection,” *IEEE transactions on medical imaging*, vol. 31, no. 8, pp. 1584–1592, 2012.
- [98] M. T. Bevacqua and R. Scapatucci, “A compressive sensing approach for 3d breast cancer microwave imaging with magnetic nanoparticles as contrast agent,” *IEEE transactions on medical imaging*, vol. 35, no. 2, pp. 665–673, 2015.
- [99] J. A. Tobon Vasquez, R. Scapatucci, G. Turvani, G. Bellizzi, D. O. Rodriguez-Duarte, N. Joachimowicz, B. Duchêne, E. Tedeschi, M. R. Casu, L. Crocco, *et al.*, “A prototype microwave system for 3d brain stroke imaging,” *Sensors*, vol. 20, no. 9, p. 2607, 2020.
- [100] B. Sohani, J. Puttock, B. Khalesi, N. Ghavami, M. Ghavami, S. Dudley, and G. Tiberi, “Developing artefact removal algorithms to process data from a microwave imaging device for haemorrhagic stroke detection,” *Sensors*, vol. 20, no. 19, p. 5545, 2020.
- [101] J. Puttock, B. Sohani, B. Khalesi, G. Tiberi, S. Dudley-McEvoy, and M. Ghavami, “Uwb microwave imaging for inclusions detection: Methodology for comparing artefact removal algorithms,” in *Body Area Networks. Smart IoT and Big Data for In-*

- telligent Health: 15th EAI International Conference, BODYNETS 2020, Tallinn, Estonia, October 21, 2020, Proceedings 15*, pp. 46–58, Springer, 2020.
- [102] B. Khalid, B. Khalesi, N. Ghavami, S. Dudley, M. Ghavami, and G. Tiberi, “3d microwave imaging using Huygens principle: A phantom-based validation,” in *2021 Photonics & Electromagnetics Research Symposium (PIERS)*, pp. 2892–2896, IEEE, 2021.
- [103] R. P. Porter and A. J. Devaney, “Holography and the inverse source problem,” *JOSA*, vol. 72, no. 3, pp. 327–330, 1982.
- [104] A. Devaney and R. Porter, “Holography and the inverse source problem. part ii: Inhomogeneous media,” *JOSA A*, vol. 2, no. 11, pp. 2006–2012, 1985.
- [105] N. Ghavami, P. Probert Smith, G. Tiberi, D. Edwards, and I. Craddock, “Non-iterative beamforming based on Huygens principle for multistatic ultrawide band radar: application to breast imaging,” *IET Microwaves, Antennas & Propagation*, vol. 9, no. 12, pp. 1233–1240, 2015.
- [106] B. Khalid, B. Khalesi, N. Ghavami, L. Sani, A. Vispa, M. Badia, S. Dudley, M. Ghavami, and G. Tiberi, “3d Huygens principle based microwave imaging through mammowave device: Validation through phantoms,” *IEEE Access*, vol. 10, pp. 106770–106780, 2022.
- [107] R. Conceição, “Mohr, and m. o’halloran,” *An Introduction to Microwave Imaging for Breast Cancer Detection*, 2016.
- [108] X. Lin, Y. Chen, Z. Gong, B.-C. Seet, L. Huang, and Y. Lu, “Ultrawideband textile antenna for wearable microwave medical imaging applications,” *IEEE Transactions on Antennas and Propagation*, vol. 68, no. 6, pp. 4238–4249, 2020.
- [109] M. Pastorino and A. Randazzo, *Microwave imaging methods and applications*. Artech House, 2018.
- [110] B. Khalesi, B. Sohani, N. Ghavami, M. Ghavami, S. Dudley, and G. Tiberi, “A phantom investigation to quantify Huygens principle based microwave imaging for bone lesion detection,” *Electronics*, vol. 8, no. 12, p. 1505, 2019.

- [111] B. Khalid, B. Khalesi, N. Ghavami, G. Raspa, M. Badia, S. Dudley-Mcevoy, M. Ghavami, and G. Tiberi, “A spiral-like acquisition strategy for 3d Huygens’ principle based microwave imaging,” in *Photonics & Electromagnetics Research Symposium (Piers) 2023*, 2023.

Appendix

Appendix I: Required Software for MWI Algorithm

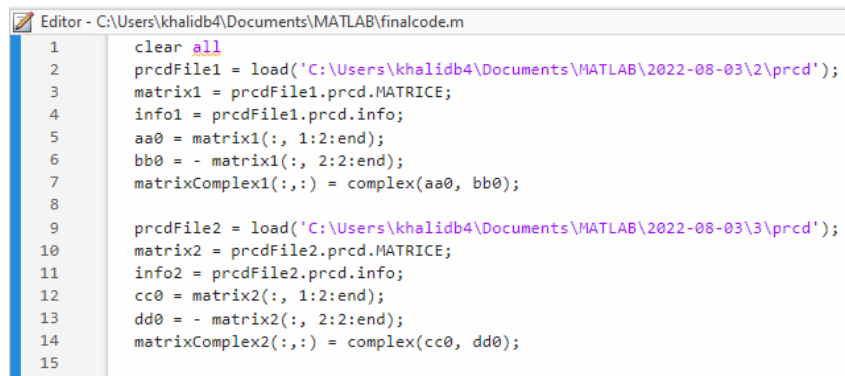
Frequency-domain measurements have been performed using a single transmitting antenna and one receiving antenna, both connected to the VNA. This arrangement facilitated the recording of the S21 parameter, which represents the complex transfer function from the transmitting to the receiving antenna. The capabilities of MATLAB, a versatile mathematical programming language known for its matrix manipulation, function plotting, and algorithm implementation capabilities, were leveraged for the image reconstruction process as outlined below:

For the measurements performed in the anechoic chamber, the results of these measurements were stored as s2p files via the VNA. Subsequently, these files were imported into MATLAB and parsed into matrices that included both the real and imaginary components of the S21 parameter. After this matrix was constructed, initial parameters were defined. This encompassed setting up the free-space parameters, establishing the axis for internal field plotting, and configuring the grid that would underpin the reconstruction of the internal field. In the domain of MammoWave, the data acquired from each measurement has been meticulously archived in the format of 'prcd' files, meticulously encapsulating the intricate complexities of the S21 parameter. Remarkably, within the realm of MATLAB's expansive toolkit, a powerful feature manifests: the ability to seamlessly load these 'prcd' files. This inherent capability not only streamlines the process but also empowers the arrangement of the extracted data into multifaceted forms, be it intricate complex matrices or a multitude of files. This attribute proves particularly invaluable when addressing the nuances associated with three-dimensional imaging endeavors.

In the subsequent steps, the software orchestrated two distinct loops. The first loop was responsible for varying the transmitting positions, while the second loop cycled through different frequencies as per the experimental procedure and frequency range used. Within this framework, an HP reconstruction process was executed, the specific details of which are safeguarded and cannot be disclosed here. Nevertheless, it's important to underscore that this step culminated in the generation of the images themselves.

Appendix II: Code Samples

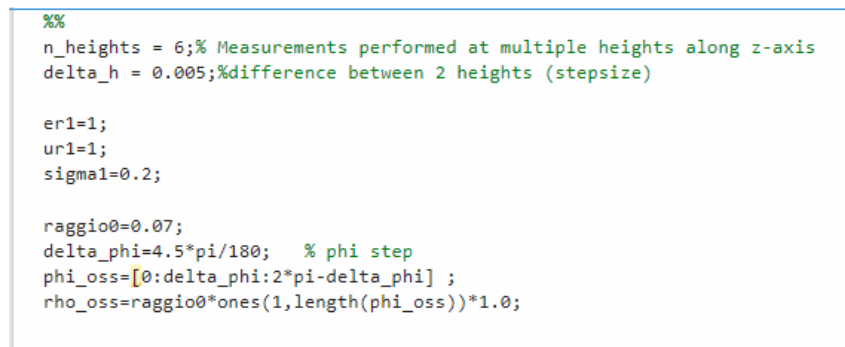
Concerning MammoWave, the data gathered from measurements has been carefully preserved within 'prcd' files. The process is visually elucidated in Figure 8.2, depicting the extraction of these files and their subsequent transformation into complex matrices. This pivotal transformation not only prepares the data for further analysis but also lays the foundation for the application of the HP-based imaging algorithm. This algorithm holds a central role in this methodology, enabling to extract meaningful insights from the collected data.



```
Editor - C:\Users\khalidb4\Documents\MATLAB\finalcode.m
1 clear all
2 prcdFile1 = load('C:\Users\khalidb4\Documents\MATLAB\2022-08-03\2\prcd');
3 matrix1 = prcdFile1.prcd.MATRICE;
4 info1 = prcdFile1.prcd.info;
5 aa0 = matrix1(:, 1:2:end);
6 bb0 = - matrix1(:, 2:2:end);
7 matrixComplex1(:, :) = complex(aa0, bb0);
8
9 prcdFile2 = load('C:\Users\khalidb4\Documents\MATLAB\2022-08-03\3\prcd');
10 matrix2 = prcdFile2.prcd.MATRICE;
11 info2 = prcdFile2.prcd.info;
12 cc0 = matrix2(:, 1:2:end);
13 dd0 = - matrix2(:, 2:2:end);
14 matrixComplex2(:, :) = complex(cc0, dd0);
15
```

Figure 1: Extraction of 'prcd' files via MATLAB.

The subsequent stage involves the establishment of preliminary essential parameters. This encompasses variables such as permittivity, conductivity, and the count of height levels—serving as the various cross-sectional planes traversing the z-axis. These parameters are pivotal in facilitating the 3D visualization process as in Figure. 8.3.



```
%%
n_heights = 6;% Measurements performed at multiple heights along z-axis
delta_h = 0.005;%difference between 2 heights (stepsize)

er1=1;
ur1=1;
sigma1=0.2;

raggio0=0.07;
delta_phi=4.5*pi/180; % phi step
phi_oss=[0:delta_phi:2*pi-delta_phi] ;
rho_oss=raggio0*ones(1,length(phi_oss))*1.0;
```

Figure 2: Defining Parameters.

Moving forward, the subsequent phase encompasses a critical task: the delineation of grid parameters. These parameters hold pivotal significance as they lay the foundation for the meticulous reconstruction of images that distinctly illustrate variations in dielectric

properties. This stage forms a cornerstone in this methodology, underscoring its relevance in achieving precise and informative visual representations (see Figure. 8.4).

```

% grid Parameters |where we want to reconstruct the internal field
delta_phi_reconstr=pi/90*4;
delta_rho_reconstr=0.0005*8;    % delta_rho_reconstr=0.0005;
h_max= delta_h*(n_heights -1)+delta_h;
h_min = 0;
delta_z_reconstr = 0.005;
%introducing z co-ordinate as heights

```

Figure 3: Defining Parameters (Grid for Reconstruction).

A distinctive attribute of MammoWave lies in its self-contained anechoic chamber, equipped with microwave absorbers. This specialized setup enables the execution of measurements in a free-space environment. Operating within the frequency domain, these measurements adhere to a predefined frequency range, as exemplified in Figure 8.5. This unique configuration affords MammoWave the capacity to conduct investigations with notable precision and reliability.

```

% free-space
u0=4*pi*10^(-7);
e0=1/(36*pi)*10^-9;
Z0=120*pi;
c0=300000000;

% frequency
f_min=1.0*10^9
f_max=6.5*10^9
df_new=5*10^6; % frequency step
new_ff=[f_min:df_new:f_max];
NF=length(new_ff);
BB=df_new*NF;

```

Figure 4: Defining Parameters (Freespace and Frequency).

Subsequent to this, the data is processed utilizing an HP-based imaging algorithm, the details of which are confidential. This process culminates in the generation of data that holds the key to reconstructing images. This data is structured within multidimensional matrices, encapsulating a comprehensive array of information pertaining to numerous cross-sectional planes across the z-axis.

The visualization aspect is brought to fruition through a well-defined plotting technique, exemplified in Figure 8.6. This technique leverages the 'contourf' plotting command, adeptly superimposing multiple cross-sectional planes along the z-axis. This visual representation underscores the efficacy of this approach, allowing for a detailed and insightful exploration of the reconstructed images.

```

fig = figure(1);
ax = gca(fig);
z_per_slice = 7;
z_base = 1;
limit=[0.6 1];
for i=0:1:6
    slice= MAG_uwb_scatt_incoh_reconstr_diff_OLD_normalised(:,:,i);
    x=X_reconstr(:,:,i);
    y=Y_reconstr(:,:,i);
    tform = hgtransform(ax);
    hold(ax, 'on')
    contourf(x,y,slice,'LineStyle','none','parent', tform, 'displayname', string(i));
    tform.Matrix = makehgtform('translate', [0, 0, 0.00]);
end
hold(ax, 'off')
view(3)
xlim(ax, 'auto')
ylim(ax, 'auto')
caxis(limit)
colorbar(ax)
grid(ax, 'on')
axis(ax, 'normal')
zlim(ax, [0 0.035])

```

Figure 5: 3D Visualisation Code sample.